Università degli Studi di Napoli
Federico II

Scuola Politecnica e Delle Scienze Di Base

Department of Industrial Engineering

Master Degree Thesis in
Aerospace and Astronautic Engineering

SETUP OF A NEW DATA ACQUISITION SYSTEM AND WIND TUNNEL TESTS OF A COMMUTER AIRCRAFT

Supervisors:
Ch.mo. Prof. Fabrizio Nicolosi
Dr. Danilo Ciliberti

Candidate:
Giuseppe Buonagura
M53001017

Academic Year 2021/2022

"When everything seems to be going against you,
remember that the airplane takes off against the wind, not with it."
— Henry Ford

Abstract

This work focuses on the experimental assessment of the aerodynamic characteristics of a commuter aircraft model, specifically investigating its longitudinal stability and control characteristics. The aircraft model was designed to be tested in various configurations: wing-body, complete aircraft, including flap and elevator deflections. Two data acquisition software were developed for the testing phase: `taraPesi` generates a matrix of weight coefficients to define the net forces/moment on the model; `DAQ_Long` acquires voltage signals and derives aerodynamic coefficients. Preliminary wind tunnel tests on the wing-body configuration, highlighted the effects of Reynolds number and flow transition. The deflection of fowler flaps at various angles showed an increase in lift, drag, and pitching moment coefficients, as well as lift curve slope. Similar effects were observed on the complete configuration. The installation of the empennage introduced the longitudinal stability, as expected. The neutral point was evaluated at different flap deflections. The elevator control power and its efficiency were also evaluated. These tests have shown that the preliminary aircraft model has good stability and control characteristics. However, these results serve as a foundation for further analysis to continue characterizing the aerodynamic behavior of this configuration.

Sommario

Questo lavoro si concentra sulla valutazione sperimentale delle caratteristiche aerodinamiche di un modello di aeromobile commuter, indagando in particolare la stabilità longitudinale e sulle caratteristiche di controllo. Il modello è stato progettato per essere testato in varie configurarioni: ala-fusoliera, velivolo completo, includendo deflessione di flap ed elevatore. Due programmi di acquisizione dei dati sono stati sviluppati per la fase di test: `taraPesi` genera una matrice di coefficienti di peso per definire forze/momenti netti sul modello; `DAQ_Long` acquisisce segnali di tensione e determina i coefficienti aerodinamici. I test preliminari in galleria, sulla configurazione ala-fusoliera, hanno evidenziatio gli effetti del numero di Reynolds e della transizione del flusso. La deflessione dei fowler flap a vari angoli, ha mostrato un aumento dei coefficienti di portanza, resistenza e momento di beccheggio, nonché della pendenza della curva di portanza. Effetti simili sono stati osservati sulla configurazione completa. L'installazione dell'impennaggio ha introdotto la stabilità longitudinale, come previsto. Il punto neutro è stato valutato con diverse deflessioni dei flap. E' stata valutata la potenza di controllo e l'efficienza dell'elevatore. Questi test hanno dimostrato che il modello di aeromobile preliminare ha buone caratteristiche di stabilità e controllo. Tuttavia, questi risultati costituiscono il punto di partenza per successive analisi, così da continuare a caratterizzare il comportamento aerodinamico di questa configurazione.

Contents

List of Figures

List of Tables

List of Abbreviations

A/D Analog to Digital. 49

AC Alternating Current. 7

ASK Available Seat Kilometers. 3

AWT Atmospheric Wind Tunnel. 28

BMS Battery Management System. 7

CAD Computer Aided Design. 55

CNC Computer Numerical Control. 66

COVID-19 Corona Virus Disease 2019. 3

CS Certification Specification. 4

DC Direct Current. 7

DEP Distributed Electric Propulsion. 3

DII Department of Industrial Engineering. 43

EASA European Aviation Safety Agency. 5

FAR Federal Aviation Regulations. 4

FST Full-Scale Wind Tunnel. 29

GDP Gross Domestic Product. 2

GEN Electricity Generator. 8

HST High Speed Tunnel. 31

IATA International Air Transport Association. 3

ICE Internal Combustion Engine. 6

LabVIEW aboratory Virtual Instrumentation Engineering Workbench. 49

LTPT Low Turbulance Pressure Tunnel. 36

MOT Motor transforms the electric power back to mechanical power. 6

NACA National Advisory Committee for Aeronautics. 27

NASA National Aeronautics and Space Administration. 28

NI National Instruments. 49

NPL National Physical Laboratory. 21

NTF National Transonic Facility. 28

OEI One Engine Inoperative. 5

ONERA National Office for Aerospace Studies and Research. 25

PC Personal Computer. 49

PON National Operational Program. 4

PROSIB Propulsion and Hybrid System for fixed and rotary wing aircraft. 4

PRT Propeller Research Tunnel. 28

RPK Revenue Passenger Kilometers. 3

SAFs Sustainable Aviation Fuels. 3

SARS Severe Acute Respiratory Syndrome. 2

SAT Small Air Transport. 5

USB Universal Serial Bus. 49

V/STOL Vertical and/or Short Take-off and Landing. 40

VDT Variable Density Tunnel. 27

VTOL Vertical Take-off & Landing. 4

WB Wing-Body configuration. 71

WBHV complete aircraft configuration configuration. 90

List of Symbols

$Æ$	wing aspect ratio
$\overline{V}_t$	tail volumetric coefficient
C	tunnel test section area
C_D	3-D drag coefficient
C_M	3-D pitching moment coefficient
C_{D_0}	3-D drag coefficient at zero lift
C_{DB}	buoyancy effect
C_{Di}	induced drag coefficient
$C_{L_{\alpha,w}}$	3-D wing lift curve slope
C_{l_α}	2-D wing lift curve slope
$C_{L_{\delta_e}}$	lift coefficient derivative with respect to the elevator deflection angle
C_{L_c}	corrected 3-D lift coefficient
C_L	3-D lift coefficient
$C_{M_{\alpha,t}}$	pitching moment curve slope of the horizontal tailplane
$C_{M_{\delta_e}}$	control power of the elevator
$C_{M_{cb}}$	3-D pitching moment coefficient referred to the balance center
C_{M_c}	corrected 3-D pitching moment coefficient
$C_{M_{polo}}$	3-D pitching moment coefficient, used in the LabVIEW program and referred to the pole of the moments

CO_2 carbon dioxide

D_p propeller diameter

$F_{x_{tar}}$ unweighted force or net force along the x axis

F_x total force along x axis containing the effects of the weight

$F_{z_{tar}}$ unweighted force or net force along the z axis

F_z total force along z axis containing the effects of the weight

M_y total moment around y axis containing the effects of the weight

NO_X nitrogen oxides

Re Reynolds number

S wing plantform area

S_t horizontal tailplane planform area

S_w wing planform area

T_p/W thrust to weight ratio

V_∞ asymptotic wind speed

V_c corrected speed considering solid and wake blockages

V_p flow speed at the propeller

a_p axial induction factor at propeller disk

a_{p_t} tangential induction factor at propeller disk

b_h horizontal tail span

b_v vertical tail span

b_w wing span

c_{kink} kink chord of the wing

c_{mac} mean aerodynamic chord of the wing, horizontal and vertical tailplane

c_{root} root chord of the wing, horizontal and vertical tailplane

c_{tip} tip chord of the wing, horizontal and vertical tailplane

d_f fuselage diameter

e Oswald's factor

l_f fuselage length

l_h distance between the aircraft center of gravity and the aerodynamic center of the horizontal tailplane

l_v distance between the aircraft center of gravity and the aerodynamic center of the vertical tailplane

$m_{y_{tar}}$ unweighted moment or net moment around the y axis

q_c/q corrected dynamic pressure to dynamic pressure ratio

w wing-induced downwash

w_p propeller-induced downwash without swirl

w_{swirl} tangential speed in the propeller slipstream

x_{ac} wing aerodynamic center longitudinal position relative to the aircraft nose

y_{ac} wing aerodynamic center lateral position relative to the aircraft nose

z_{ac} wing aerodynamic center vertical position relative to the aircraft nose

$\Delta\alpha$ variation of the angle of attack

ΔC_D variation of the 3-D drag coefficient

ΔC_L variation of the 3-D lift coefficient

ΔC_M variation of the 3-D pitching moment coefficient

$\Delta C_{D_{wb}}$ variation of the 3-D drag coefficient due to the wake blockage effect

$\Lambda_{c/2}$ sweep angle at half chord

ΩR tangential speed of the propeller tip

Ω propeller angular speed

α angle of attack

α_c corrected angle of attack

α_{iw} induced angle of attack due to the finite wing

δ boundary correction factor

δ_e elevator deflection angle

ϵ sum of solid and blockage

ϵ_{sb} solid blockage

ϵ_{wb} wake blockage

η_t horizontal tail dynamic pressure ratio

ω flow angular speed

ρ_∞ asymptotic air density

τ_e elevator efficiency

$\tau_{2,t}$ streamline curvature effect on the incidence angle, this is an amount of correction referred to the tailplane

$\tau_{2,w}$ streamline curvature effect on the incidence angle, this is an amount of correction referred to the wing

1

Introduction

Contents

1.1 World population and air transport

Understanding population trends and anticipating demographic change are crucial for national development planning. The forecast is that the world's population will continue to grow in the coming years and is projected to reach 8.5 billion in 2030, 9.7 billion in 2050 and 10.4 billion in 2100. Population growth is caused in part by declining levels of mortality, as reflected in increased levels of life expectancy at birth. Globally, life expectancy reached 72.8 years in 2019, an increase of almost 9 years since 1990. Further reductions in mortality are projected to result in an average longevity of around 77.2 years globally in 2050 [1].

Over the one hundred years from 1950 to 2050, the world population was growing

the fastest in the '60s, when it was increasing on average by 2.1 per cent per year, as shown in Figure 1.1. Since then, the pace of population growth has slowed by more than half owing to reduced levels of fertility. In 2020, and for the first time since 1950, the rate of population growth fell below 1 per cent per year and it is projected to continue to slow in the next few decades and through the end of this century. Conversely the number of people it is always increasing and it could grow to reach a value of 9.7 billion in 2050 [1].

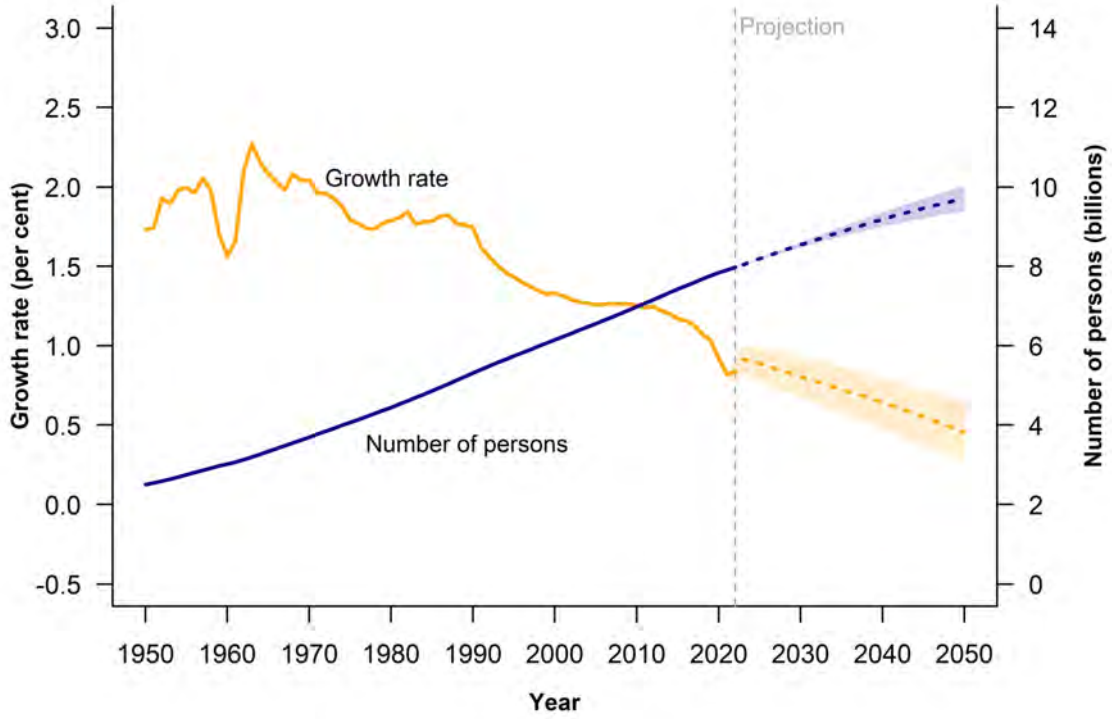

Figure 1.1 Global population size and annual growth rate: estimates, 1950-2022, and medium scenario with 95 per cent prediction intervals, 2022-2050 [1].

Moreover, although more than 8% of the world population still lives in conditions of extreme poverty in 2022 [2], the average gross domestic product (GDP) per capita has increased exponentially over the past century [3]. This growth can justify the continuous increment in the amount of kilometers that the average world citizen will travel by 2050. At beginning of century world citizens moved 23 billion of kilometers in total; by 2050 that figure will grow to 105 billion [4]. In particular, if we focus only on the volume of the air traffic, over the years it has doubled every 15 years. Therefore, not only the total amount of kilometers traveled is increasing, but also the fraction covered using air transport is on the rise. However, over the last 20 years, the aviation industry has been involved in several crisis, e.g., the terror attacks in 2011, the SARS pandemic in 2003 and the financial crisis in 2008. These crises had a different global spread, speed, impact on economies and aviation markets and have

assumed different shapes of recovery. Focusing now on the COVID-19 crisis, however, looks like a severe combination of past crises applied at a global level. The 2020 International Air Transport Association (IATA) traffic statistics showed a decrease of 56.7% in worldwide passenger capacity (Available Seat Kilometers—ASK) and a passenger traffic (Revenue Passenger Kilometers—RPK) was lower at −65.9%. The drop in RPKs has seriously affected revenues: IATA estimated a net industry loss of $126.4 billion in 2020. This crisis cut deeper into the airline industry than any crisis before and it will take years for a full recovery. Although the COVID-19 pandemic, the aviation industry is expected to keep on expanding in the long term. In the most optimistic scenario, the aviation stakeholders expect a return to 2019 traffic level within a few years [5].

While the growth in the air travel is both a driver and a consequence of globalization, it is accompanied by increasing concerns regarding the associated environmental implications. Aviation emissions contribute to global warming through the emission of carbon dioxide (CO_2), nitrogen oxides (NO_X), and increased cloudiness due to contrails and cirrus formation [6, 7]. Even though the aviation is currently responsible only of a small amount of total carbon emissions, from 2.0% to 2.5%; of this small contribution, more than 90% of the carbon emissions come from the commercial operations of large passenger aircraft, which carry more than 100 passengers per trip [8]. Thus, the international challenge of reducing aviation emissions and their impact on climate is receiving increasingly attention.

Analyzing the COVID-19 pandemic period in 2020, due to forced confinements and therefore to the temporary reduction in flights, this appeared to be a positive aspect of a catastrophic event, thanks to non-negligible reduced (CO_2) emissions [9]. However, also looking at the benefits of global temperature due to the short-term dynamics of the pandemic, these are likely to be small. Thus, without underlying long-term decarbonisation at the system level of economies, even massive changes in behavior only lead to modest reductions in the rate of warming [10]. Already in 2012, the European Commission defined sustainable goals in the "Flight-path 2050" to reduce the climate impact of aviation. The targets were to achieve a 75% reduction in (CO_2) and 90% reduction in nitrogen oxide (NO_X) emissions by 2050 [11]. The way to meet these targets is to consolidate a new technologies in aviation. The key solutions identified are: *propulsion and energy storage*, *aerodynamic* and *airframe* technologies.

In the propulsion and energy storage technologies, the main solutions concern the usage of different energy sources: sustainable aviation fuels (SAFs), electric propulsion architectures, batteries for Hybrid-electric propulsion, fuel cells and hydrogen.

In the aerodynamic technologies are included: distributed electric propulsion (DEP), tip propeller, high-lift propeller, boundary layer ingestion, noise mitigation for DEP systems, laminar flow, riblets, ultra-high aspect ratio wings and high-lift devices [8].

This chapter mainly focuses on the working concept of hybrid-electric or full

electric propulsion and on the distributed electric propulsion technology.

1.2 The PROSIB Project

The development of hybrid-electric propulsion aircraft is progressing in parallel with the evolution of enabling technologies in the field of electrical systems. The goal is the reduction, starting from 2035, of the energy required for air transport by about 20% compared to "not electric propulsio" solutions available at that time, contributing to the reduction of the environmental impact.

The PROSIB (Propulsion and Hybrid System for fixed and rotary wing aircraft) project was a PON initiative funded by the Italian Ministry of University and Research. It involved industry, university and research centers. Configurations for regional aircraft and rotary wing platform (VTOL - Vertical Take-off & Landing) as well as architectures for the propulsion systems, including distributed hybrid-electric technologies, were investigated to identify the best strategy in using the different onboard energy sources. Part of this project dealt with the possible propulsive and electric storage sizing, as well as wind tunnel tests for a 19-pax innovative airplane configuration. This is the main focus of this thesis.

1.2.1 Innovative commuter aircraft: certification problem

A 19-seater airplane is considered a commuter aircraft, which has a limited maximum take-off weight of 19000 lbs (8618 kg) to be certified with FAR/CS 23. Any kg more and the airplane is considered a commercial transport aircraft, where FAR/CS-25 apply, with different airworthiness and operations rules.

The advanced commuter aircraft should be a revolutionary design, where disruptive technologies are applied to significantly reduce atmospheric pollution caused by aircraft operations [12]. Of course, aerodynamic, propulsive, and structural technology levels are the key factors to design such an advanced airplane.

Transport aircraft are mainly regulated by Part 23 [13], *Certification Specifications for Normal, Utility, Aerobatic, and Commuter Category Aeroplanes*, and Part 25 [14], *Certification Specifications for Large Aeroplanes*. In compliance with sub-part A of CS-23.1, "Applicability", CS-23 airworthiness code is applicable to:

- Airplanes in the normal, utility and aerobatic categories that have a seating configuration, excluding the pilot seat(s), of nine or fewer and a maximum certificated take-off weight of 5670 kg (12500 lb) or less; and
- Propeller-driven twin-engine aeroplanes in the commuter category that have a seating configuration, excluding the pilot seat(s), of nineteen or fewer and a maximum certificated takeoff weight of 8618 kg (19000 lb) or less.

On the other hand, CS-25.1 declares that this airworthiness code is applicable to turbine-powered large airplanes, without indicating weight or size limit of the aircraft.

The regulations in force do not account for the future electric aircraft. In most cases, the innovative configurations with hybrid-electric technologies proposed are introducing new risks that are not explored in current certification process. Without having explained these technologies in detail yet, for instance, in case of distributed electric propulsion (DEP), the use of the aero-propulsive interactions to increase the maximum lift coefficient during take-off and landing phases is still something that should be regulated, since the reliability of powered high-lift devices is still considered unsatisfactory by current regulation. In the same way, the One Engine Inoperative (OEI) condition requirements could be redefined in the case of distributed electric propellers, depending on how these are powered. In this case, a driving factor could be the thrust provided by each propeller or the power management architecture making some propellers more reliable than others or the distance of the propellers with respect the centre of gravity, which is crucial when sizing the vertical tailplane. For these cases where regulation does not provide specific guidelines, dedicated solutions should be proposed.

The absence of a specific certification code for hybrid-electric and full-electric aircraft makes necessary the introduction of Special Conditions by the European Aviation Safety Agency (EASA). These give designers a framework in which aircraft can be certified in Europe in the future, because at time of writing there are no certified electric aircraft for passengers' transport.

1.2.2 Why interest in a commuter aircraft?

The need for significant emission reduction in aviation pushes research into developing outstanding technologies as well as manufacturing and operational strategies. These technologies, already mentioned at the end of Sec. 1.1, can be easily integrated into a commuter aircraft. In fact, it is opinion of the European Community that advances on the Small Air Transport (SAT) will be a fundamental step to assess the feasibility of new technologies, results in terms of CO_2, NO_X, noise emissions, and will pave the way for the development of large greener airplanes.

Nowadays, commuter aircraft have performance that make them capable to take-off and land in tiny regional or remote utility airports, provide a reduced fuel consumption compared to bigger aircraft, have a fast turnaround time, and can be deployed on routes that would not be geographically or economically viable by rail or road, nor by larger aircraft such as regional turboprops or jets. In this perspective, SATs have a deserving role in a societal functions, helping connections between locations and serve local communities that would otherwise be isolated or confined to much slower road or rail transport. Additionally, SAT aircraft could be employed as a low-cost/short-range cargo for standard pallets delivery in area of the world

where rail is not an option [8].

1.3 Electric propulsion system

Electric propulsion systems convert electric energy into mechanical energy, which is then converted into thrust by a propeller or fan. These systems are an effective way to reduce pollutant emissions as long as the energy sources are renewable. Electric propulsion systems can be classified into: all-electric, hybrid-electric or turbo-electric [8].

1.3.1 Hybrid-electric propulsion

Hybrid-electric propulsion system integrates an electric powertrain with a conventional propulsion system, to provide propulsion. It can combine the clean power of an electric propulsion system with a conventional engine, reducing the fuel burned and therefore emissions [15].

Starting with conventional propulsion system, by considering functional aspect only, it is possible to evolve multiple hybrid propulsion systems. More specifically, a conventional propulsion system is extended step by step with electric components until the most complex hybrid system is achieved.

Figure 1.2 shows a simplified setup of conventional propulsion system, without involving gears and multiple shafts. This system is composed of an internal combustion engine (ICE) and a propulsor. The ICE transforms fuel into mechanical power and can be either a piston or a gas turbine engine. The propulsor on the right side, converts mechanical power to propel the vehicle.

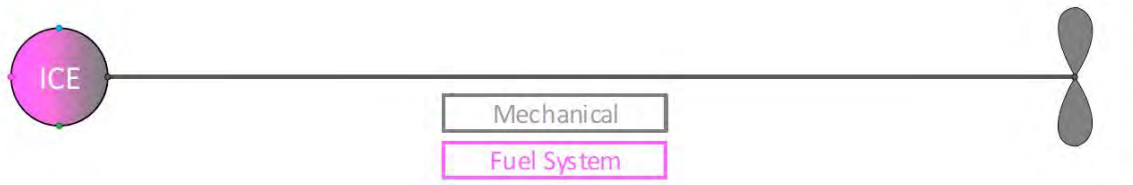

Figure 1.2 Conventional propulsion system.

Hybrid-electric propulsion systems are divided into two categories: parallel hybrid and serial hybrid systems [8].

1.3.2 Parallel hybrid systems

In parallel hybrid systems, the ICE and the MOT are both mechanically connected to the propulsor, so they can contribute to the propulsion energy either simultaneously

or individually [15].

The conventional propulsion system in Figure 1.2 can be extended to a parallel hybrid system, as shown in Figure 1.3, by adding an electric energy storage system which can supply power to the propulsor shaft.

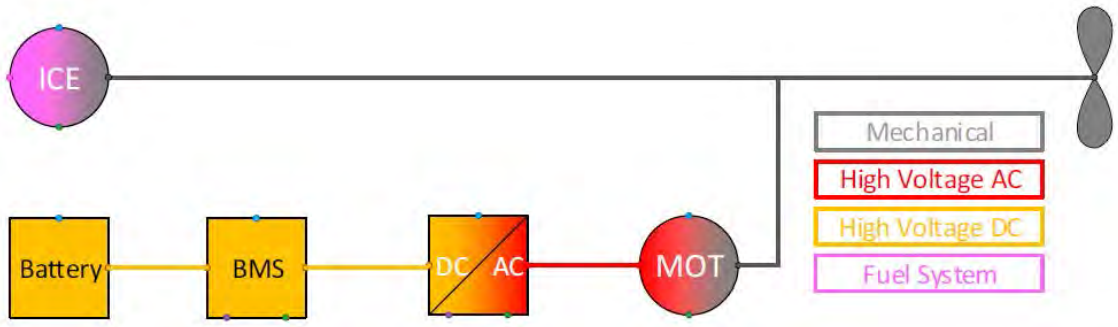

Figure 1.3 Parallel hybrid propulsion system.

The electric energy storage system, here battery but it could be any electric energy storage or fuel cell, can supply additional power during short time mission segments. Hence, the ICE can be downscaled to an average continuous load and the peak load are covered by the additional power from the electric energy storage. The higher load of a downscaled ICE is a beneficial for efficiency but disadvantageous for the lifetime of the engine that operates at higher temperatures and pressure.

In Figure 1.3, the battery energy flows through a battery management system (BMS) — an electronic device that ensures the health of battery cells — then it is supplied to an inverter — DC to AC conversion — which drives an electric motor. The mechanical power of the motor is supplied to the propulsor shaft. Depending on the power electronic design, the energy flow can be bidirectional: the battery can be charged by absorbing mechanical power from the ICE during operative phases in which the propulsor does not require much power [8].

1.3.3 Serial hybrid system

In serial hybrid system, the propulsor is driven exclusively by the electric motor. The conventional propulsion system in Figure 1.2 can be extended to a serial hybrid system, as shown in Figure 1.4.

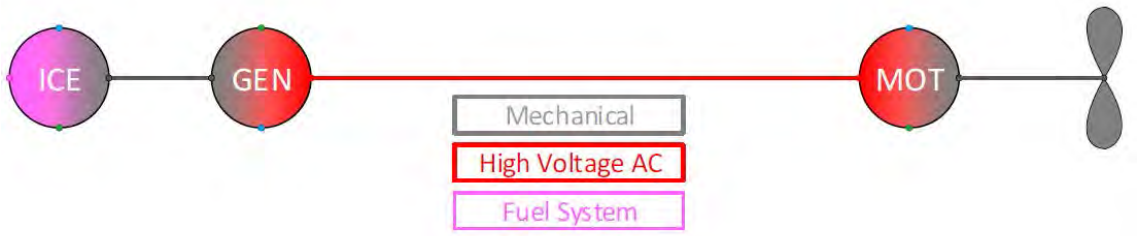

Figure 1.4 Serial hybrid propulsion system, "electric shaft system".

The mechanical power derived from the ICE is converted into electric power through a generator (GEN). The motor (MOT) transforms the electric power back into mechanical power which is supplied to the propulsor. This system is called "electric shaft", as there is no control input to manipulate the power transmission along the line. The generator design, the rotational speed, and the power of the ICE determine the voltage, the current, and the frequency in the AC transmission system. The motor configuration determines the rotational speed and the mechanical power of the propulsor [8]. In this system, there is no mechanical shaft between GEN and MOT, but the non-adjustable voltage between the two electric machine makes it impossible to set the rotational speed of the MOT regardless of the rotational speed of the ICE and GEN. This reduces the degree of freedom of the system. Therefore, if one needs to connect multiple propulsors to one engine, a good solution to adjust the torque and power demand of each propulsor can be a variable pitch mechanism.

Moreover, this system requires a particular star-up sequence with a very low load to enable the spool-up of the propulsors together with the engines and the generators. This requirement reduces the application only to hybrid-electric aircraft with variable pitch propulsors as they can feather the propulsor and spool-up with a low torque load [8]. The advantages of using two electric machines, MOT & GEN, are the simplicity of connecting multiple propulsors and generators to the AC transmission system, as well as the simplicity of routing cables through the vehicle instead of rigid shafts.

While the drawback of this system is the cogging torque[1] limit of the electric machines in such a setup. When the transmitted torque exceeds the cogging torque of synchronous machines, the machines gets desynchronised, which leads to the loss of power transmission and the excessive mechanical forces [8].

Electric shaft with electric energy storage The electric shaft system can also be extended with an electric energy storage to provide additional power during short mission segments, as shown in Figure 1.5.

[1] Torque created by the magnetic attraction between magnets on the rotor and the iron teeth of the stator. It can be physically felt as an intermittent "jerking" motion by rotating the shaft of a conventional brushless motor when it is not under voltage. The cogging torque adds an oscillating component to the constant torque desired by the machine, which can produce vibration and noise, especially at low speed.

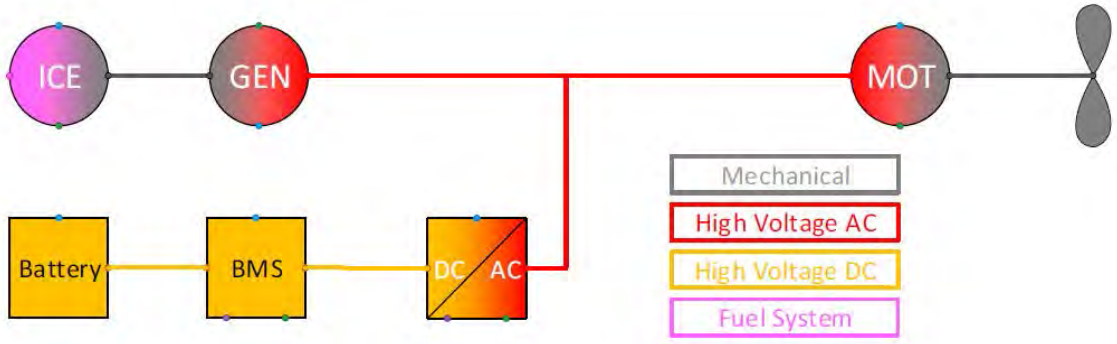

Figure 1.5 Electric shaft with electric energy storage.

The advantages are related to the ICE that can be downscaled to increase its efficiency and reduce its weight, but also to the power electronics of the energy storage would allow to remove the cogging torque limitation of the electric machines. This allows to reduce the size of both electric machines and cables to be used [8].

Turbo-electric propulsion system Adding power electronics devices to the AC transmission, it is possible to extend the electric shaft system. The rectifier device — AC/DC — transforms the AC power from the generator into DC power. The inverter — DC/AC — transforms the DC power into AC power and then transmits it to the propulsor. In the aerospace industry, this system, without an energy storage, is called the turbo-electric propulsion system [8], as shown in Figure 1.6.

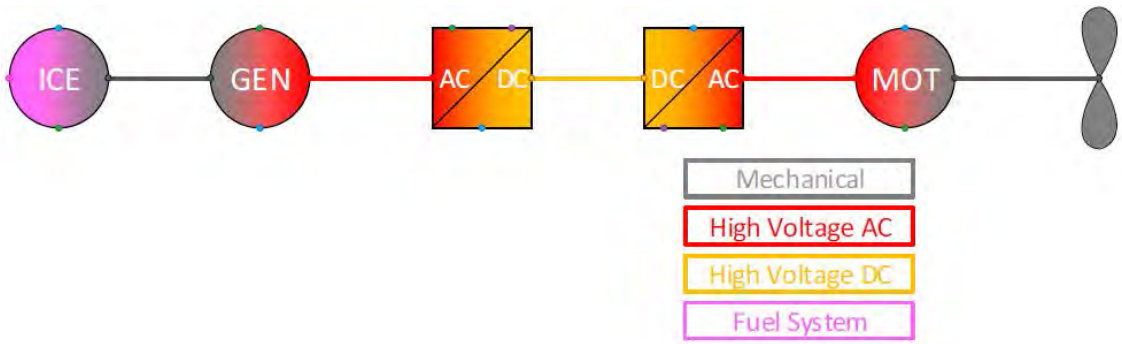

Figure 1.6 Turbo-electric propulsion system.

In this configuration, the introduction of power electronic devices — AC/DC and DC/AC — completely decouples the rotational speeds of the ICE and propulsor. In other words, there is no mechanical shaft between ICE and MOT, but there is the possibility to manage the voltage between the two electric machines through a rectifier and an inverter, allowing the rotational speed of the motor to be set independently of the rotational speeds of the ICE and GEN. This allows to control multiple propulsors independently of each other, without the need for variable pitch mechanics at the propulsors.

DC link - Turbo-electric propulsion system with energy storage An extension of this system with an all electric energy storage which supplies the DC link [8], is shown in Figure 1.7.

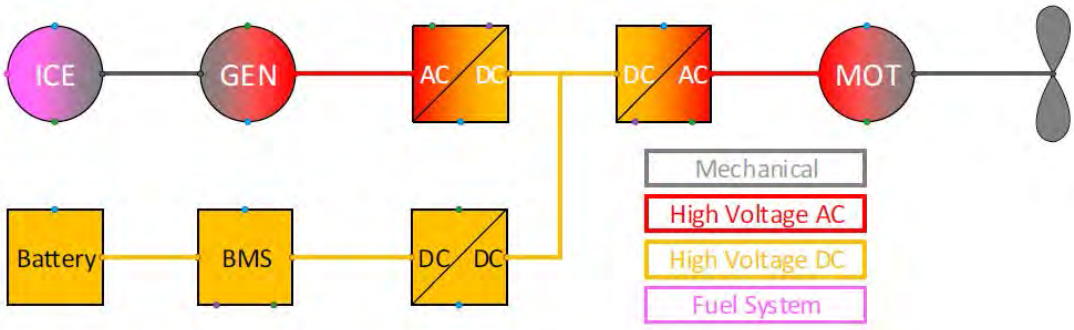

Figure 1.7 Turbo-electric propulsion system with energy storage.

Comparison of the electric shaft and the DC link topology

- DC link topology allows the rotational speeds of the electric machines to be decoupled, while the electric shaft does not.
- Fixed pitch rotors can be used each one independently in a DC link topology, while the electric shaft requires the pitch mechanism to split power between multiple rotors.
- DC link has no torque limitation, while the electric shaft has a torque limit that must not be exceeded during operation to ensure synchronization of all electric machines.
- Both topologies can be extended with electric energy storage subsystems.
- Non-propulsive power offtake is feasible in both topologies.
- DC link topology is more complex than the electric shaft topology, which has a lower number of components and only passive components.
- DC link topology has higher losses in electric machines than the electric shaft.
- DC link topology has higher losses in power electronics devices than the electric shaft topology, as the latter has no power electronic devices.
- Mass of the electric machines will be higher as the machines must be designed for the maximum peak torque to avoid desynchronization. These will be higher in the electric shaft than the DC link topology.
- Mass of power electronic is absent in the electric shaft and it is high in the DC link topology.

- Mass of cables will be larger in the electric shaft than the DC link topology, as the cables must be sized for reactive power in the system [8].

1.4 Distributed electric propulsion

The development of distributed electric propulsion (DEP) for aircraft systems has opened up new possibilities for the the overall efficiency, capabilities, and robustness of future air vehicles. This propulsive concept is based on the novel approach of utilizing electrically driven propulsors that are only electrically connected to the energy sources or power-generating devices. In particular, the increased design freedom in terms of number, size and location of the propulsors results in advantages of aero-propulsive coupling and provide improved performance than the traditional designs [16].

Multiple conventional aircraft, as well as various short and vertical takeoff and landing (VTOL) platforms have been developed with distributed electric propulsion. The placement and configuration of electrically driven propulsor can be beneficial for boundary layer ingestion and thus increase propulsive efficiency and wake-filling benefits. Furthermore, the placement and configuration can also be used to mitigate the trailing vortex system of a lifting surface, by using a "tip-propeller", or leverage increases in dynamic pressure across the blown surface for increased lift performance, with the so-called "high-lift propeller" or blowing. Additionally, the thrust stream of distributed electric propulsors can be utilized to support the vehicle control, thus being able to mitigate requirements for traditional control surfaces and to increase tolerance of the vehicle control system to engine-out or propulsor-out scenarios. It is also possible that aircraft with distributed propulsion may employ differential thrust as a mean to reduce or eliminate the vertical tail and remain still compliant with regulations. One more advantage can be represented by the development of new low-noise configurations, through the installation of small propulsors of a DEP system to leverage an acoustic shielding effect by the airframe [8, 16].

DEP is a disruptive concept that can lead to unprecedented improvements in the future aircraft designs. Several example of disruptive configurations using DEP technologies can be seen in Figure 1.8.

The DEP aircraft concepts generally involve the use of multiple electric propulsors around an airframe with one or more electric generators or energy storage devices. Several electric aircraft concepts have been configured and even manufactured at various organization throughout the world. However, due to the limited specific power or specific energy density of available hardware, this technology has been initially used on many small aircraft. Then, the interest of increasing efficiency, decreasing operating costs, and reducing environmental emissions of larger commercial aircraft applications, has allowed the organisations to research DEP aircraft system for larger passenger and cargo-carrying capabilities [16]. A certain

(a) *NASA X-57 Maxwell: tip-mounted and leading-edge distributed propulsion.*

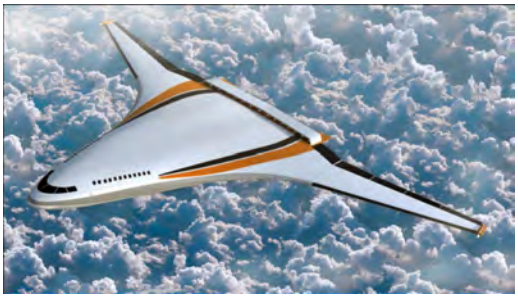

(b) *NASA N-X3: tip-mounted and distributed turbo electri propulsion concept.*

(c) *NASA STARC-ABL: centerline propulsive-fuselage concept with boundary-layer ingestion.*

(d) *ESAero ECO-150: concept with two turbo-electric generator and sixteen electric ducted fans.*

(e) *Airbus Vahana VTOL aircraft.*

Figure 1.8 Disruptive configurations using DEP technologies.

level of aero-propulsive coupling is reached depending on the type of propulsion unit in use — for instance, propeller versus ducted fan — and the proximity of those propulsion units to the wing, tail surface, or fuselage. By adopting a careful design, the propulsion-airframe integration can be advantageously used and can be broken down into several categories:

- improvements in propulsive efficiency due to boundary-layer ingestion,
- strategic placement of propulsor result in a reduced drag through wake filling and vortex suppression “wing-tip propeller”,
- propeller or fan slipstream interacting with an aerodynamic surface to produce some form of enhanced lift or control authority [16].

Moreover, effects on aircraft stability and control due to distributed propulsion

technologies must be carefully evaluated during preliminary design stage to avoid potential disadvantages of such integration [8].

1.4.1 Wing-tip propeller effects

It has been previously discussed that the use of distributed electric propulsion has several advantages in aircraft design. One such advantage is the ability to install propellers at the wing-tips, which can be used to mitigate wing-tip vortices and reduce induced drag.

In detail, by placing the propellers in front of the wing-tips and using their rotation to counteract the effects of the wing-tip vortices, it is possible to reduce the induced drag. The slipstream of a propeller can affect the performance of the wing in various ways. One main impacts is an increase in speed downstream of the propeller. In the following discussion, in the first place it is also assumed that only the speed component normal to the propeller plane is increased. However, this assumption neglects the swirl in the propeller slipstream, whose interaction with the tip vortex of the wing causes a variation of induced drag, even more than the increase in the axial speed [8].

The induced drag can be approximated accordingly to Equation (1.1), because of the wing finiteness. The variation of induced drag C_{Di} is linked to the variation of induce angle α_{iw}; by decreasing α_{iw}, C_{Di} is reduced. The presence of wing finiteness causes a decrease in the angle of attack due to the downwash effect, as shown in Figure 1.9, and the result is an induced angle of attack due to the wing, that can be α_{iw} approximated using Equation (1.2).

$$C_{Di} = C_L \alpha_{iw} \tag{1.1}$$

$$\alpha_{iw} \approx \frac{w}{V_\infty} = \frac{C_L}{\pi \mathcal{A} e} \tag{1.2}$$

What happens by changing the axial speed? The rotating propeller increases the flow axial speed, as shown by the red arrow in Figure 1.9. The variation of axial speed causes an upwash effect counteracting the downwash due to the wing, in other words, the induced angle α_{iw} due to the finiteness wing is reduced by the induced angle α_{ip} due to the increase in axial speed produced by the propeller. The actuator disk theory provides an estimation of the axial induction factor a_p at propeller disk as a function of thrust to weight ratio T_p/W and the propeller diameter D_p, using Equation (1.3). Finally, the flow speed at the propeller V_p is given by Equation (1.4):

$$a_p = \frac{1}{2}\sqrt{1 + \frac{8}{\rho_\infty \pi V_\infty^2} \frac{T_p/W}{D_p^2/W}} - 1 \tag{1.3}$$

$$V_p = a_p V_\infty \tag{1.4}$$

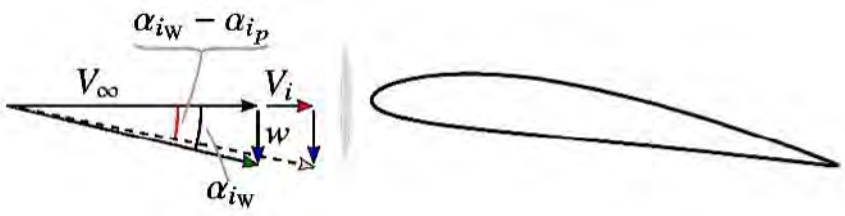

Figure 1.9 Induced angles due to wing and actuator disk.

What happens by considering the flow rotation? Beyond the axial induction, the propeller slipstream induces a rotational motion in the downstream flow. Assuming a certain rotation direction of the propeller, the tangential induction factor a_{p_t} can be defined as the ratio between the flow angular speed ω induced by the propeller rotation and the propeller angular speed Ω, using Equation (1.5). The tangential speed w_{swirl} perceived in the propeller slipstream is the product of the tangential induction factor a_{pt} and the tangential speed of the propeller tip ΩR, according to Equation (1.6). Finally, the induced angle can be computed using Equation (1.7), which takes into account the following contributions:

- w: wing-induced downwash,
- w_p: propeller-induced downwash without swirl,
- w_{swirl}: tangential speed in the propeller slipstream.

$$a_{p_t} = \frac{\omega}{2\Omega} = \frac{1}{2} - \sqrt{\frac{1}{4} - \frac{V^2}{\Omega^2 R^2}(1 + a_p)a_p} \tag{1.5}$$

$$w_{\text{swirl}} = a_{p_t}\Omega R \tag{1.6}$$

$$\alpha_i = \tan^{-1}\left(\frac{w + w_p + w_{\text{swirl}}}{V_\infty + V_P}\right) \tag{1.7}$$

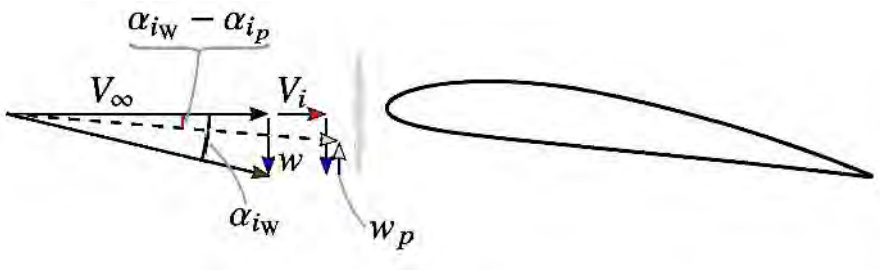

Figure 1.10 Induced angles due to wing and rotating disk.

Therefore, it is also advantageous to take into account the rotation of the flow produced by the propeller, because by properly rotating the tip propeller in the opposite direction relative to the tip-vortex (inner-up direction), it is possible to reduce the induced angle of attack and hence the induced drag [8].

Several investigations supporting this phenomenon have been conducted over the years. In particular as early as 1969, Synder and Zumvalt [17] proposed that aircraft can be designed using propellers at the wingtips in such a way that the lift-to-drag ratio (L/D) can be varied by changing the effective aspect ratio in flight. An experimental program testing a wing with propellers mounted at the wingtips showed that the use of a propeller at the wingtip, turning in the direction opposite to that of the wing vortex, shifts the trailing vortex core outboard, decreases the wing drag coefficient, increases the maximum lift coefficient and increases the effective aspect ratio. These effects at different propeller position along the wing span are shown in Figure 1.11. Conversely, rotating the propeller in the opposite direction has the reverse effect.

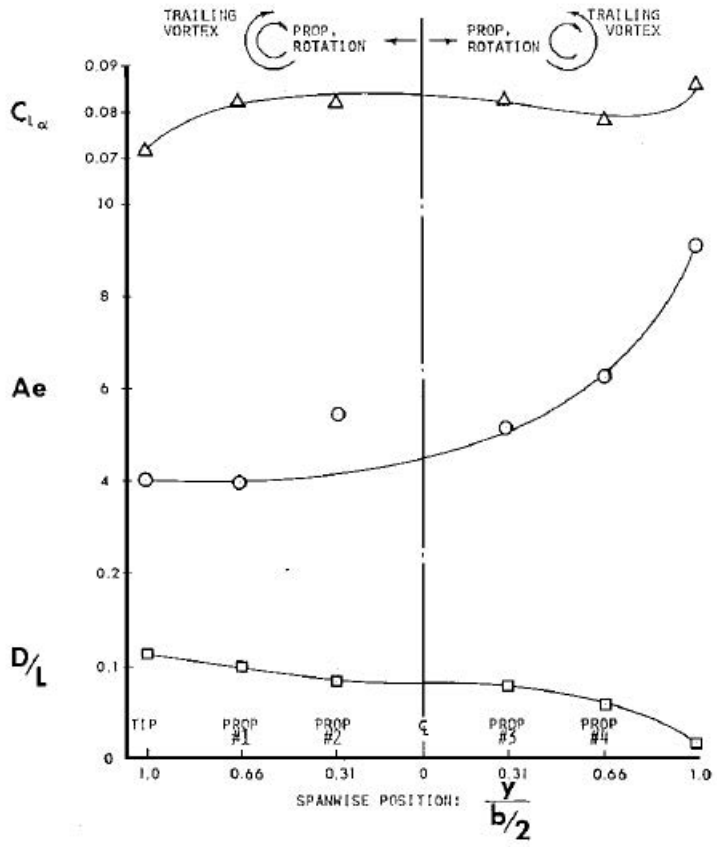

Figure 1.11 Effect of propeller position and rotation direction on wing characteristics [17].

In Figure 1.11, the results are shown considering both the trailing vortex rotating in the same direction as the propeller (left side of the charts) or considering them

counter-rotating (right side of the charts). The effective aspect ratio attaining the maximum value at wing tip, lift curve slope remains constant until 70% span then increasing by about 10% at wing tip, and drag-to-lift ratio decreasing at 0.02 at wing-tip. Other results similar to this one, have been obtained by several other authors, as highlighted in [8]. The common thread between all these investigations is again the reduction of induced drag through the use of a wing-tip mounted propeller.

2

Low-Speed Wind Tunnels

Contents

2.1 History pills

Over the years, low-speed experimental aerodynamics has continued to be important in the development of vehicles and devices that are subject to air or water flow forces. In the 1970s and continuing into the early 1980s some experts predicted that the need for aerodynamic experiments, particularly in the subsonic regime, would would decline as computational fluid dynamics improved. It is true that computational capability has continued to improve at a substantial pace, but it has not advanced enough to reaching a level sufficient to replace the need for experimental data in development projects.

The increased capability of computing equipment has greatly impacted the field of experimental aerodynamics by allowing for faster data collection and real-time sharing of results with people at widely separated geographic locations [18].

2.1.1 Wind tunnel origins

The earliest wind tunnels were invented towards the end of the 19th century. Early experimenters realized that they had two options for testing models: moving the model through the air at a specific velocity or blowing air past a stationary model. The wind tunnel was envisioned as a means of reversing the usual paradigm: instead of the air standing still and an object moving at speed through it, the same effect would be obtained if the object stood still and the air moved at speed past it. Benjamin Robins (1707–1751), a brilliant English mathematician, invented a whirling arm for moving models at high speeds — Figure 2.1 — to determine drag and did some of the first experiments in aviation theory [19].

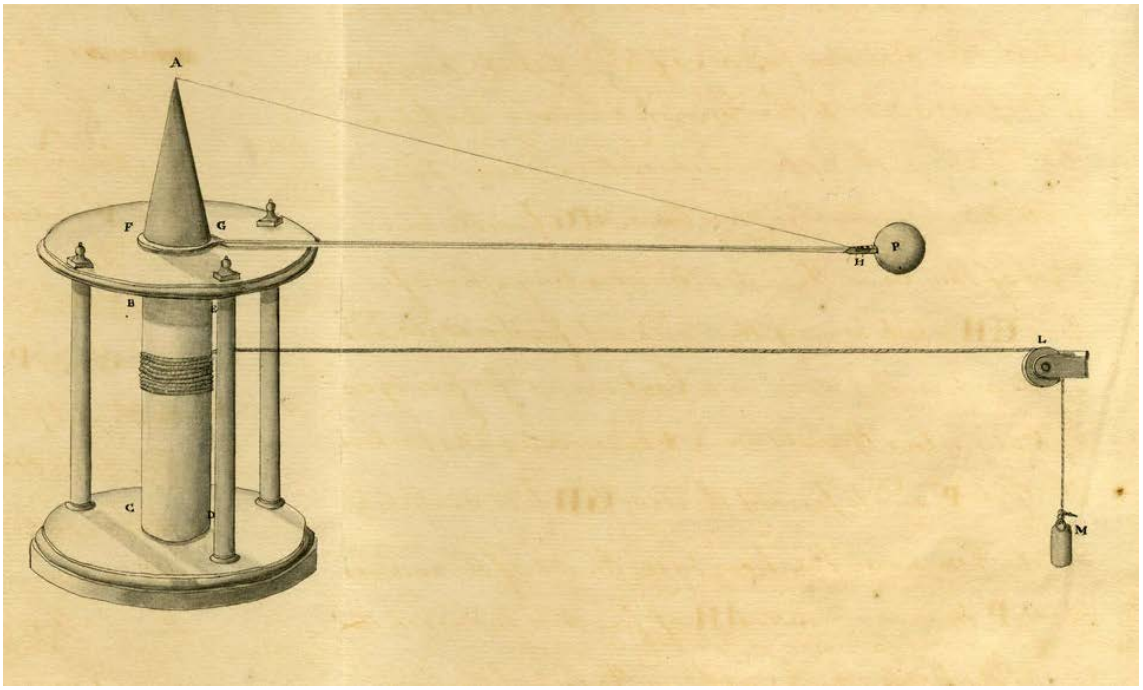

Figure 2.1 Whirling arm device in which weight (M) turned a drum and rotated the test object (P), https://prints.royalsociety.org/products/whirling-arm-rs-11565, credits: Benjamin Robins.

Sir George Cayley (1773–1857) also used a whirling arm to measure the drag and lift of various airfoils. However, at the end of the 19th century, the disadvantages related to the whirling arm began to be understood. In particular, the wing on the end of an arm was forced to fly in its own wake, which meant that with so much turbulence, it was difficult determine the true relative velocity between the model and air, but also to mount instruments and measure forces exerted on the model when it was spinning at high speeds [19].

Otto Lilienthal's (1848-1896) hang glider experiments were preceded by his testing of various lifting surfaces using a whirling arm device, he obtained discouraging results from tests on flat airfoils and cambered surfaces [19].

Francis Herbert Wenham (1824–1908), a member of the Aeronautical Society of Great Britain, solved these issues by creating the first enclosed wind tunnel in 1871 [19].

In a series of notable experiments, the Englishman Osborne Reynolds (1842–1912) of the University of Manchester showed that the airflow pattern over a scale model would be identical to that of a full-size vehicle if a certain flow parameter, now known as the Reynolds number, were the same in both cases. This established a scientific basis for using models in wind tunnels to replicate real-life phenomena. The Reynolds number is a fundamental parameter in the description of all fluid-flow situations. [19].

Sir Hiram Maxim (1840-1916), also used a huge whirling arm to test airfoils. However, when he realized that his whirling arm had limitations, a wind tunnel became the main focus of his experimental work [19].

In America, Samuel Langley (1834-1906) was an early figure in the field of aeronautics. He was a mathematician, astronomer, and secretary of the Smithsonian Institution. He conducted experiments using a whirling arm apparatus, which was located outdoors and was often disturbed by wind and the self-created mass of air swirling around the arm [19].

So annoying were Langley's problems that, in 1901 the Wright brothers used a wind tunnel as test facility to study the effects of airflow over various shapes while developing their Wright Flyer — Figure 2.2 — [19].

(a) *Wright brothers 1901 replica of wind tunnel. National Museum of the United States Air Force.* https://tinyurl.com/mr287fwz

(b) *The rebuilt Wright Flyer in the National Air and Space Museum* [19].

Figure 2.2 Wright brothers wind tunnel and Wright Flyer.

The first post-Wright wind tunnel laboratory for aeronautical research was built in America by Albert Zahm, a professor at Catholic University in Washington D.C. He operated a wind tunnel with a wide test section dimensions. This facility, shown in Figure 2.3, was notable for its unique methods of instrumentation, calibration, and application to aeronautical research [19].

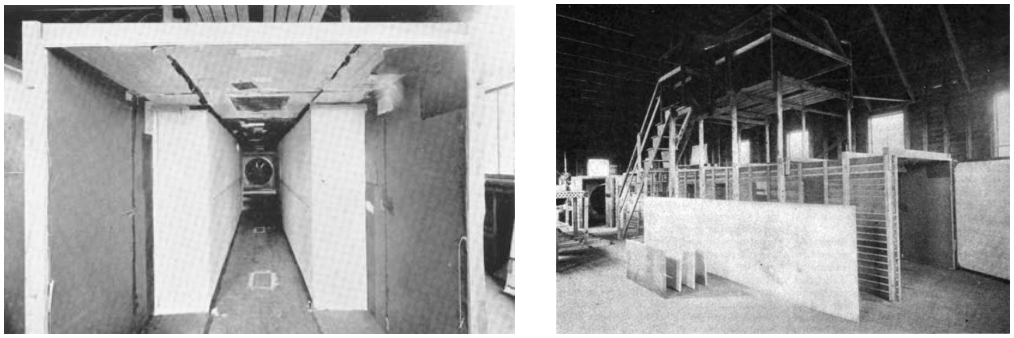

Figure 2.3 Albert Zahm's "air tunnel" built at Catholic University Washington, DC, in 1901. [19], https://www.wright-brothers.org/History_Wing/History_of_the_Airplane/Doers_and_Dreamers/Doers_and_Dreamers_XYZ.htm

The first wind tunnels built, such as the one built by Wright Brothers, used the air moved by a fan disposed upstream of the wind tunnel's test section, as shown in Figure 2.4. The convergent section, which is located upstream of the test section, increases the velocity in the test section due to the mass conservation law for the flow, which is expressed for an incompressible flows, by:

$$V \cdot A = \text{constant} \tag{2.1}$$

where V represents the velocity of the flow and A the surface in the considered section.
Conversely, disposed upstream of the test section, the fan blades cause swirling flow oscillations which are pushed through the tunnel making it difficult to obtain a uniform flow [20].

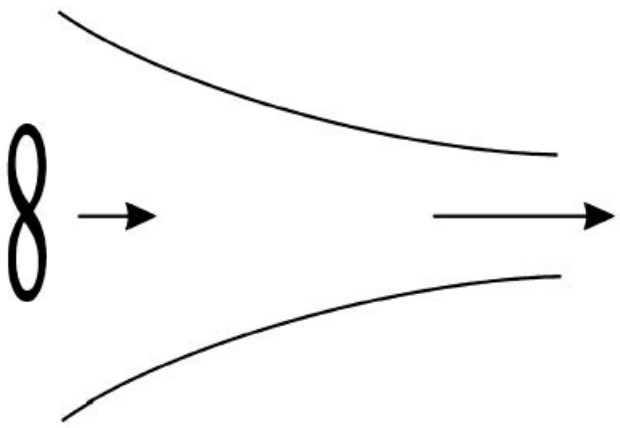

Figure 2.4 Fan upstream of the test section.

The passage to suction is also a significant advancement in the field of wind

tunnel design. With the fan positioned downstream of the test section, as shown in Figure 2.5, it no longer interferes with the model, resulting in a significant improvement in the quality of flow. [20].

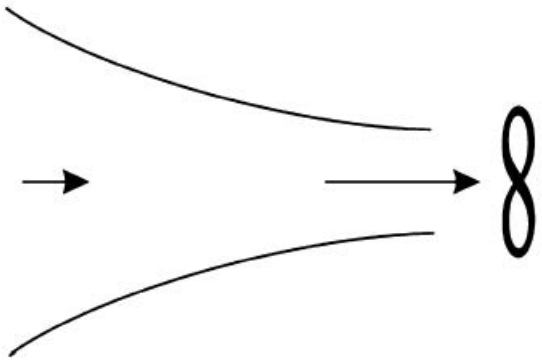

Figure 2.5 Fan downstream of the test section.

2.2 Types of wind tunnels

Wind tunnels are facilities that use fans or compressed air to simulate wind and study the action of the airflow around an object. The test section is the part of the circuit where the solid is studied and the forces exerted on the solid immersed in a fluid can be measured [20]. There are two different types of wind tunnels and two basic test-section configurations can be adopted. However, there are numerous variations and specific features of different wind tunnels, making each one unique in its design and capabilities. The two basic types are open circuit and closed circuit. The two basic test section configurations are open test section and closed test section [18].

In open circuit wind tunnel, the air flows through an essentially straight path from the entrance through a contraction to the test section, then through a diffuser, fan section, and exhaust. The tunnel may have a test section with no solid boundaries (open jet or Eiffel type) or solid boundaries (closed jet or National Physical Laboratory — NPL — type) [18]. This facility is shown in Figure 2.6.

In closed-return wind tunnels, also known as Prandtl or Göttingen type, the air flows in a continuous loop with little or no exchange with the exterior. This facility is shown in Figure 2.7. Generally, these tunnels have a single return, although some have been built with double or annular returns. These tunnels may have either a closed or open test section, and some tunnels have been built that can be operated

with either an open or closed test section, as needed for a particular experimental program [18].

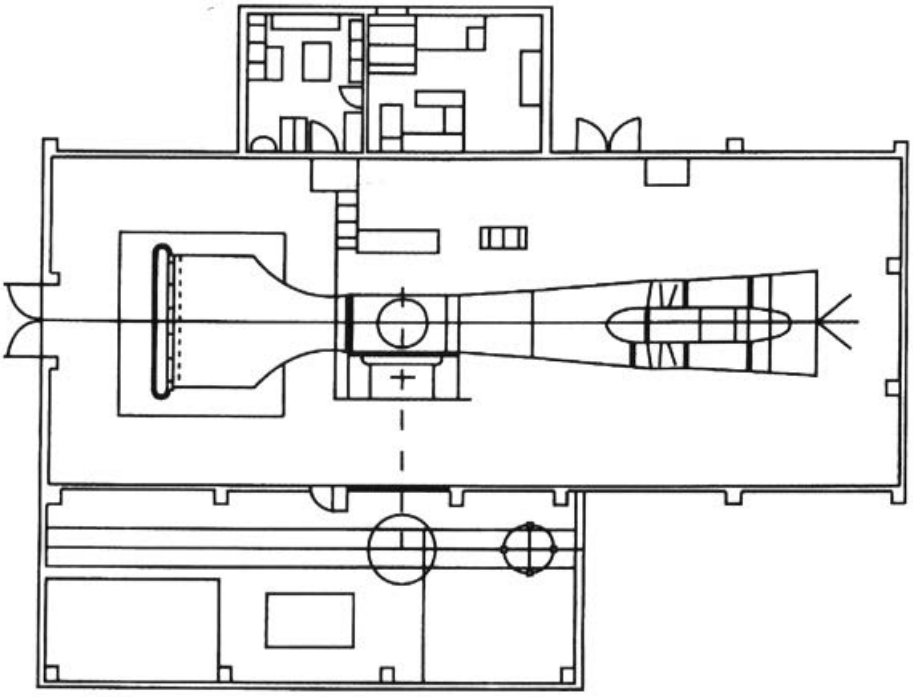

Figure 2.6 Plan view of an open circuit wind tunnel.

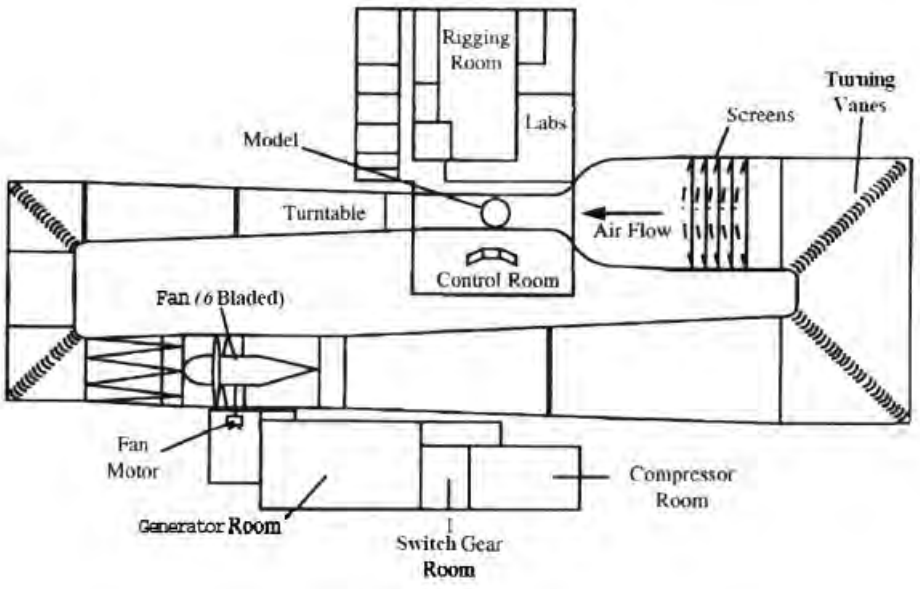

Figure 2.7 Plan view of a closed circuit wind tunnel.

There are advantages and disadvantages with both the open- and closed-circuit-type tunnels and with both open and closed jets [18].

Open return wind tunnels

Advantages

- Low construction costs.
- Internal combustion engines can be run and extensive flow visualization through smoke can be performed without any purging issue, as long as both the inlet and exhaust are open to the atmosphere.

Disadvantages

- If located in a room, the size of the tunnel in relation to the room size may require extensive screening at the inlet for optimal flow. Similarly, if the inlet and/or exhaust is open to the atmosphere, operation may be affected by wind and cold weather conditions.
- For a given size and speed the tunnel will consume more energy to run. This is typically only a concern for developmental experiments where the tunnel has a high utilization rate.
- Open circuit tunnels tend to produce high levels of noise, which can create environmental issues, restrict hours of operation, and necessitate extensive noise treatment of the tunnel and surrounding room.

Closed return wind tunnels

Advantages

- The use of turning vanes and screens allows for precise control of flow quality and makes it independent of external factors such as other activities within the building and weather conditions.
- Less energy is required for a given test-section size and velocity, which can be important for high utilization developmental experiments (two or three shifts, five to six days a week).
- Less noise during operation, minimize environmental impact.

Disadvantages

- The initial cost is higher due to inclusion of return ducts and turning vanes.
- If used for smoke flow visualization experiments or running of internal combustion engines, a method for purging the tunnel must be implemented.
- If tunnel has high utilization, it may require an air exchanger or other cooling system to prevent overheating.

Depending on the purposes, an open or closed test section can be chosen.

An open test section in an open circuit tunnel will require an enclosure around the test section to prevent air being drawn into the tunnel from the test section instead of the inlet.

For closed return tunnels of large size with an external balance, the open test section has one solid boundary to protect the balance from wind.

Many open test-section, closed circuit tunnels have encountered significant flow fluctuation issues that necessitate extensive post construction evaluations and corrective measures. The most common solution is to adopt a closed test section. Furthermore, to accommodate a full scale vehicle, the test section should have as large a cross-sectional area as possible. However, due to the increase in size of aircrafts since World War II, building wind tunnels to accommodate full-size aircraft is cost prohibitive. It is more important to aim for Reynolds numbers that are as close as possible to full-scale values rather than focus solely on size [18].

2.3 Aeronautical wind tunnels

Throughout history a wide variety of wind tunnels have been built and used for aeronautical purposes. The facilities that have helped the aviation world in the study and development of aircraft with ever increasing performance are discussed below.

2.3.1 The European tunnels

Eiffel Tunnel In France, Gustave Eiffel (1832 – 1923) built his first open-return wind tunnel in 1909. It was 1.5 meters in diameter and of the open-jet type. He ran over 4000 tests in this wind tunnel between 1909 and 1912 using air jetting from a special nozzle directed into the test section at speeds up to 20 meters per second, and routed back to the nozzle by the walls of the building rather than a separate return passage. [19]. In 1912 Eiffel significantly improved the efficiency of the open-return wind tunnel, building the second generation of tunnels. He enclosed the test section in a chamber, designed a convergent at entrance section with a honeycomb flow straightener and added a diffuser between the test section and the fan located at the downstream end of the diffuser, Figure 2.8. These were arrangements followed by a number of wind tunnels later built; in fact the open-return low-speed wind tunnel is often called the Eiffel-type wind tunnel [20].

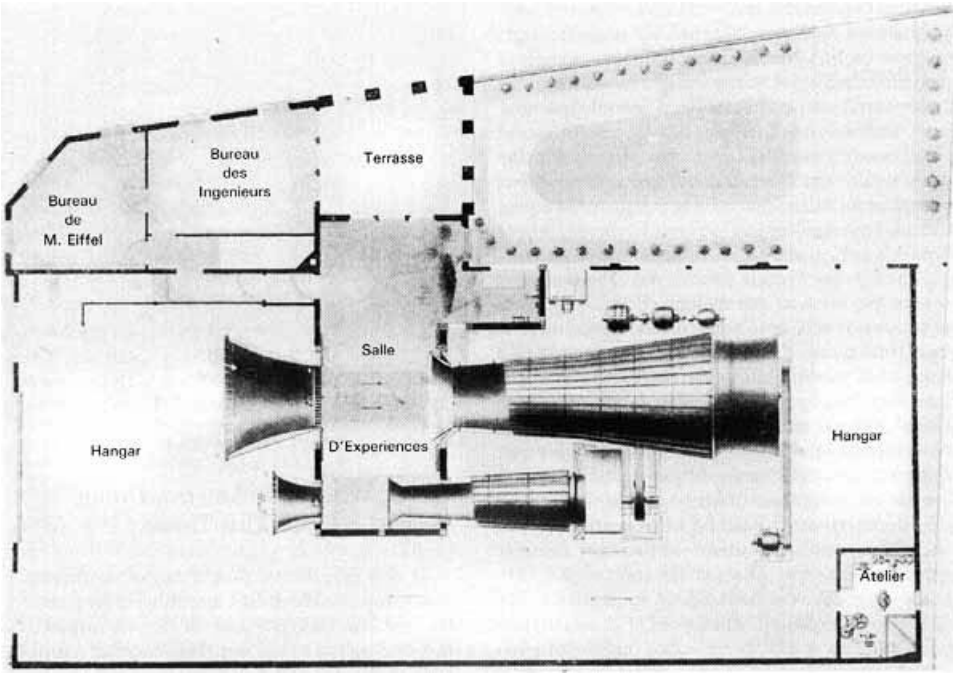

Figure 2.8 Eiffel's second-generation wind tunnel at Auteuil in 1912 [19].

Prandtl or Göttingen Tunnel In 1908, at the University of Göttingen in Germany, the world's first continuous-circuit, return-flow wind tunnel was put into operation under the direction of the renowned aerodynamicist Ludwing Prandtl. It was equipped with vanes at the corners to turn the flow, screens, and honeycomb strategically positioned to homogenize and quite the airflow. Prandtl's second generation tunnel, built at Göttingen in 1916, greatly influenced basic wind tunnel design. Most of the world's large wind tunnels built in the last century have been based on this second generation model. Prandtl added two features in this second generation: a stilling chamber upstream of the test section to reduce flow disturbances, and a contraction cone at the entrance of the test section to create a uniform air velocity across test section and to reduce turbulence, it is shown in Figure 2.9.

England had also constructed wind tunnels at the government-supported National Physical Laboratory — NPL — in London. The first of several large tunnel made its debut in 1912. In 1918, Great Britain's second-generation wind tunnel went into operation at the NPL. The most notable feature of the design was the large size of the test section, which measured 7 $\times$ 14 foot, and was well suited for tests of complete aircraft configuration [19].

Antonin Lapresle, collaborator and successor of Eiffel at the Auteuil wind tunnel, designed a large wind tunnel — Figure 2.10 — at the request of the Air Ministry. It had been built between 1932-1934 in a suburb of Paris, Chalais-Meudon. The wind tunnel was used to test full size aircraft and was equipped with six large fans driven by high powered electric motors. The Chalais Meudon wind tunnel was used by ONERA under the name S1Ch until 1976. The installation, which had

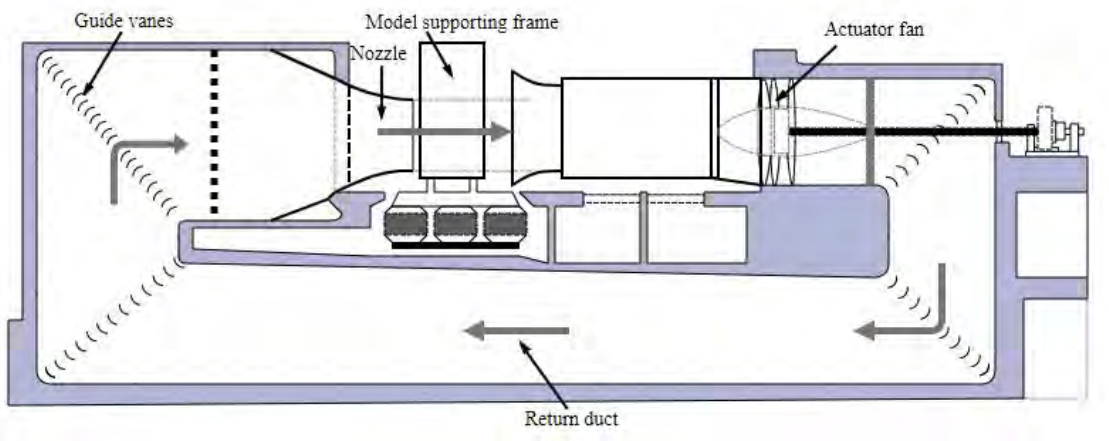

Figure 2.9 Prandtl's second-generation wind tunnel at Göttingen in 1916. https://fr.m.wikipedia.org/wiki/Fichier:Windtunnel3-en.svg.

become obsolete, has been disused in 1977. The building was classified as a historical monument in 2000. It was used to test the aerodynamics of aircraft, automobiles and buildings in many national programs. [20].

Figure 2.10 View of the large S1Ch wind tunnel in Meudon [20].

2.3.2 The American tunnels

By the time of World War I began, Europe had taken the lead in aerodynamic research and this continued throughout the war. Just before hostilities began, Albert Zahm once again applied his talents to wind tunnel design, this time building a wide tunnel in 1913 at the Washington Navy Yard, to generate aerodynamic data for future naval aircraft. The National Advisory Committee for Aeronautics —NACA — engineers didn't have a broad background of wind tunnel experience. They built NACA Wind Tunnel No. 1 — a low speed tunnel with no return circuit for the air passing through the test section. Operation began on June, 1920. This wind tunnel served as a learning tool for the United States to re-enter aeronautical research.

High-Reynolds-Number Tunnel Until 1921 all the wind tunnels that had been constructed around world, were operating at normal atmospheric pressures. As a result, the experimental results obtained using scale models in the tunnels were open to question due to a mismatch of Reynolds number with those encountered in the actual flights of full-scale aircraft. The Reynolds number of 1/20-scale models being tested at operational flight velocities would be too low by a factor of 20. Reynolds' classic experiments had shown that airflow conditions could be vastly different for model and full-scale aircraft. Since the Reynolds number is also proportional to air density, a solution to the problem of scale effects would be to test 1/20-scale models at a pressure of 20 atmospheres, which would match the Reynolds number in wind tunnel tests and actual full-scale flights.

In order to solve the problem of scale effects, NACA's Executive Committee decided to build a Variable Density Tunnel —VDT — in which air pressure could be varied. Max Munk, formerly in Göttingen and now a NACA Technical Assistant, proposed building a wind tunnel inside a large tank that could be pressurized to 20 atmospheres, as shown in Figure 2.11.

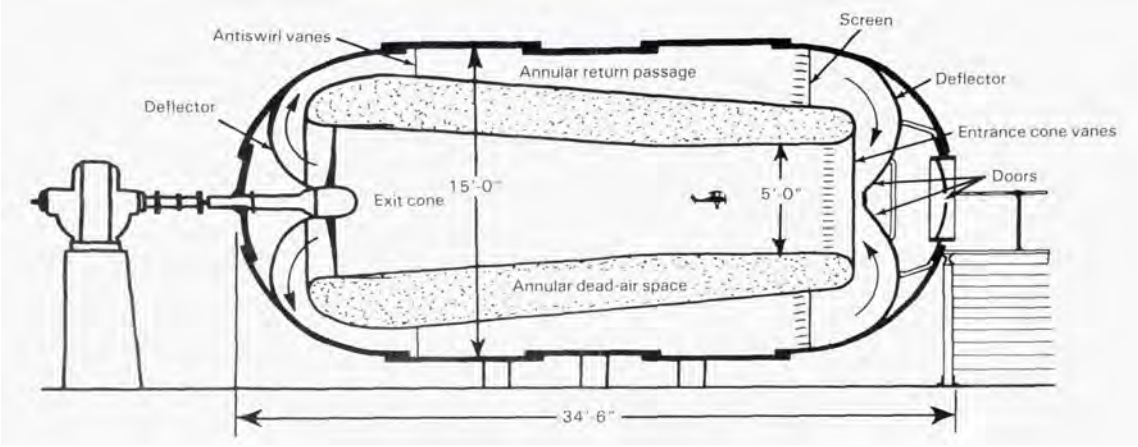

Figure 2.11 Cross section of the variable density tunnel showing the annular flow of the returning air [19].

By March 1923 the VDT was operational. It quickly became the primary source for aerodynamic data at high Reynolds numbers [19]. However, some basic issues such as the cost of construction and operation of pressurized tunnels had to be considered. The cost of the compressor equipment had to be accounted for, and also the provision of access to the model test area without decompressing the entire tunnel added to construction complexity and cost. Furthermore, the operation of pressurized facilities took more to change the pressure condition and to access the model, reducing the productivity of the facility and increasing the cost for users [18].

Another possible approach to increase the Reynolds number was to change the working fluid, using Freon 12. Again, there were many problems of a pressure tunnel, such as initial cost, cost of pumps, cost of the gas, and finding a way to make the test section habitable for model changes. An example of a tunnel that used Freon 12 as the working fluid, beginning 1960, was the Transonic Dynamics Tunnel at the National Aeronautics and Space Administration (NASA) Langley. However, due to the detrimental effect of Freon on the environment, plans were made to use a different heavy gas, referred to as R-134a [18].

A cryogenic tunnel was another approach to increase the Reynolds number. This tunnel reached high Reynolds number by virtue of both increased pressure and decreased temperature. The working fluid was nitrogen, and by injecting liquid nitrogen upstream of the fan, the gas was cooled. The National Transonic Facility (NTF) was built at Langley Research Center. Its operation was based on this approach [18].

Vertical and AWT Tunnels The National Advisory Committee for Aeronautics, decided to replace their Wind Tunnel No. 1 at Langley Field with two new tunnels due to the increasing demand for their research facility in the late 1920s, as aviation grew both commercially and militarily. The first tunnel to be constructed had the test section tilted of 90 degrees and was built vertically, as shown in Figure 2.12a, for detailed studies of aircraft spinning. This phenomenon occurred when an aircraft lost speed and rolled off on one wing, it developed a spinning motion about a vertical axis from which recovery was difficult and sometimes impossible. The second tunnel was the Atmospheric Wind Tunnel — AWT — operational in 1930, shown in Figure 2.12b. The AWT was designed as an aerodynamic research tool to study high-lift wings and general problems of stability and control [19].

Propeller Tunnel One of the earliest propeller tunnels was built at Stanford University in 1917 with a 5.5-foot diameter test section. Then, George Lewis, NACA Director of Research proposed the construction of a new special wind tunnel for propeller research that would be large enough to test the entire fuselage with operating engine and propeller, shown in Figure 2.13. The Propeller Research Tunnel — PRT — went into operation in July 1927. The test section air velocity was only 110 mph, while test section was 20 feet in diameter.

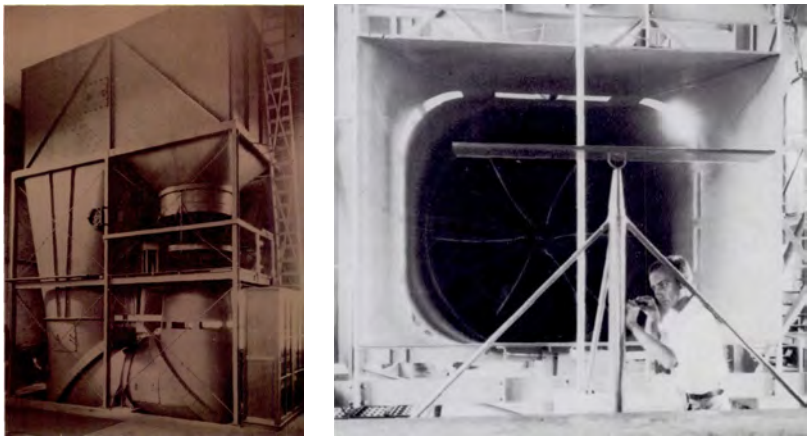

(a) *NACA's vertical wind tunnel at Langley.*

(b) *Atmospheric Wind Tunnel of 1930.*

Figure 2.12 Vertical and Atmospheric Wind tunnel [19].

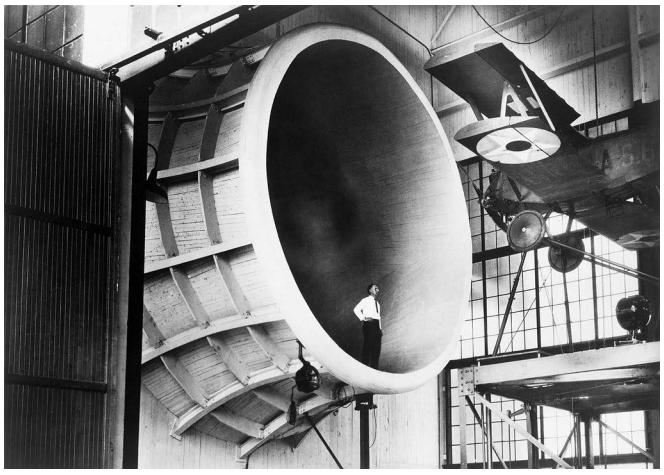

Figure 2.13 Propeller Research Tunnel with Sperry M-1 Messinger full-scale airplane [19].

Besides propeller experiments, this tunnel also demonstrated that exposed landing gears contributed to increased fuselage drag, that there was an advantageous location of engine nacelle relative to the wing for aircraft to perform at best, and that the design of cowls (NACA cowl) for radial engines reduced drag and improved cooling [19].

Full Scale Tunnel The possibility to explore several research areas, in particular, how rotating propeller affect aircraft controllability or what interference effects are created by aircraft component, led the idea to test only full scale models or the actual aircraft. The National Advisory Committee for Aeronautics (NACA) — NASA's predecessor — with Smith J. De France began the design of the Full-Scale Wind Tunnel — FST — at Langley in 1929. The cavernous test section of the FST, shown in Figure 2.14, could accommodate a modest two-story house. It was 30×60-feet, with an open throat that facilitated the installation of full-size aircraft. Downstream, two propellers, each driven by a separate electric motor, circulated air

through the test section. The air circuit was of the double-return type; that is , the airflow from the dual propellers was spilt into two streams, one going right and the other going left. The two streams then double back between the test section and the building's wall, and then reunited prior to the throat of the section, shown in Figure 2.15. The tunnel was completed in the spring of 1931 [19].

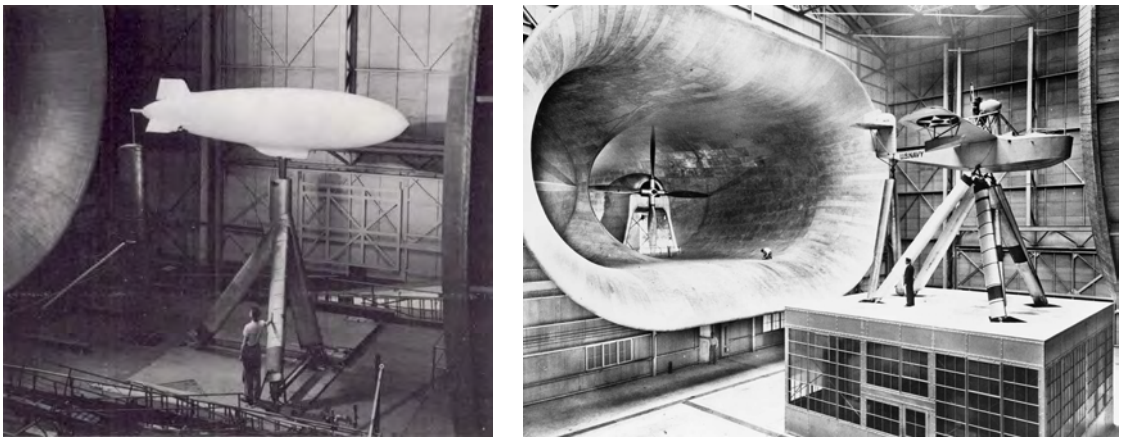

(a) *A scale model of an airship is set up for testing in the full-scale wind tunnel* [19].

(b) *A full-size Loening XSL-1 reconnaissance flying boat is set up for testing in the full-scale wind tunnel, 1932.* https://tinyurl.com/ms8ksrw6

Figure 2.14 Open test section of Full-Scale wind tunnel.

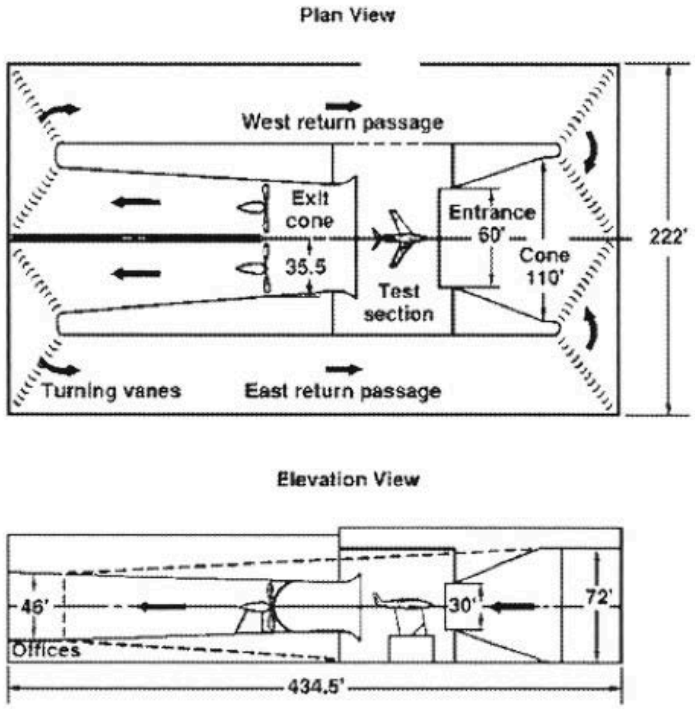

Figure 2.15 Cross-section of the Langley Full-Scale Tunnel showing the general layout and dimensions of the facility, https://www.nasa.gov/centers/langley/news/factsheets/30X60.html

Wind tunnels accelerate to Mach 1 Through 1932 NACA's wind tunnel were all subsonic. When Joseph S. Ames became Chairman of NACA in 1927, he prioritized the development of high-speed wind tunnels and research capabilities for transonic and supersonic speeds. One of the first obstacles was the lack of electric power needed to run such tunnel, as the power required to operate a wind tunnel increases as the third power of the wind velocity. The solution was found by Langley engineers. They realized that a large reservoir of energy was stored in the 5200 cubic feet of air compressed to 20 atmospheres in the variable density tunnel (VDT). This energy was thrown away every time the tank was blown down to change models. They proposed to redirect the VDT exhaust through a smaller tunnel and use the jet as a high-speed windstream.
The Langley 11-inch High Speed Tunnel — 11" HST — was born. In October 1934 tunnel with a 24-inch test section was put into operation and also used the exhaust air from the VDT. Whit this tunnel NACA in 1939 was able to develop and provide aerodynamic data on a family of new high-speed airfoils, using model of only a few inches [19].

The first big high-speed tunnel The necessity to increase the dimensions of tunnel to test sizeable models of a complete aircraft, ended in 1936 with construction of tunnel with 8 feet in diameter able to reach Mach 0.75. In 1945 this airspeed was increased to Mach 1 [19].

Free-Flight Tunnels In the conventional tunnel, the idea to simulate flight was impossible. The model, in this tunnel was attached to supports so that aerodynamic forces could be measured. Langley engineers decided to build a free-flight wind tunnel so that dimensionally and dynamically scaled models could be flown under the influence of gravity. The tunnels could be tilted to set the angle of the air stream to match the glide path of the model. This would allow the study of maneuverability and flight performance of the models, and often control surfaces could be deflected by command through a trailing wire. Two of these tiltable free-flight wind tunnels were constructed at Langley. The first one, which was 5 feet in diameter, was built in 1937. The second one, which was 12 feet across, was built in 1939. The 12-foot free-flight tunnel was used until the early 1950s. Later on, it was replaced by powered models flown in the Langley full-scale tunnel, discussed previously and shown in Figure 2.14, which had a large test section of 30 × 60-foot.

A Nineteen-Foot Pressure Tunnel In 1939 the 19-foot pressure tunnel, shown in Figure 2.16, was a response to reach a full-scale Reynolds numbers and applying the result of model to the full-scale aircraft. Consequently, the aerodynamicists needed a bigger tunnel operating at high pressures, due to the fact that Reynolds number is proportional to both size and air density. This tunnel helped develop several World War II military aircraft and in 1959 it became the Transonic Dynamics Tunnel [19].

(a) *The 19-foot pressure tunnel at Langley Field,* https://www.flickr.com/photos/nasacommons/9421769755.

(b) *The 23 vanes in the 19 foot pressure wind tunnel force the air to turn corners smoothly,* https://tinyurl.com/ycxp4bny

Figure 2.16 The 19-foot pressure wind tunnel.

The War-Time Tunnels at Ames In 1940, NACA began construction on a new laboratory at Moffett Field, California, which is now known as the Ames Research Center of NASA. At the time, the military needed to test new aircraft with moderate speeds — about 250 mph. In May 1940 construction began on two 7 × 10-foot wind tunnels, showed in Figure 2.17, with a closed-throat, single return circuit operating at atmospheric pressure [19].

Figure 2.17 The two wartime 7 × 10 foot wind tunnels built at Ames [19].

The third wind tunnel, showed in Figure 2.18, built early December 1941 at Ames was a giant — 16 feet in diameter at the test section. The tunnel configuration was fairly conventional, with a closed-throat, single return circuit [19].

Figure 2.18 The Ames 16-foot wind tunnel [19].

The fourth war-time wind tunnel, built at the Ames department, went into operation in June 1944. It had a test section of 40 × 80 feet, as shown in Figure 2.19. The low speed below 230 mph was not a problem because the purpose of the tunnel was to examine the take-off and landing characteristics of aircraft. Six 40-foot-diameter fans, Figure 2.20, each powered by a 6000- horsepower electric motor maintained airflow at a defined velocity. In June 1944 this tunnel went into operation [19].

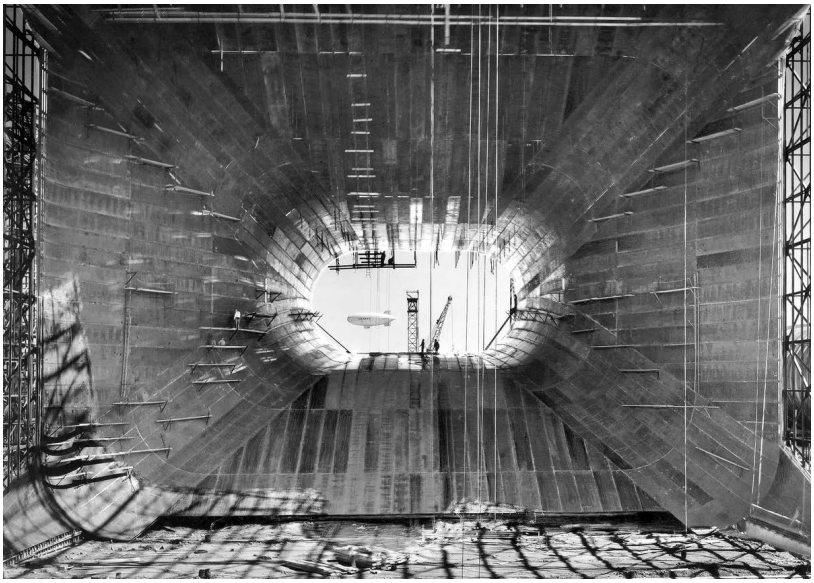

Figure 2.19 The cavernous entrance cone and test section of the Ames 40 × 80 feet full-scale wind tunnel, https://tinyurl.com/ms8ksrw6.

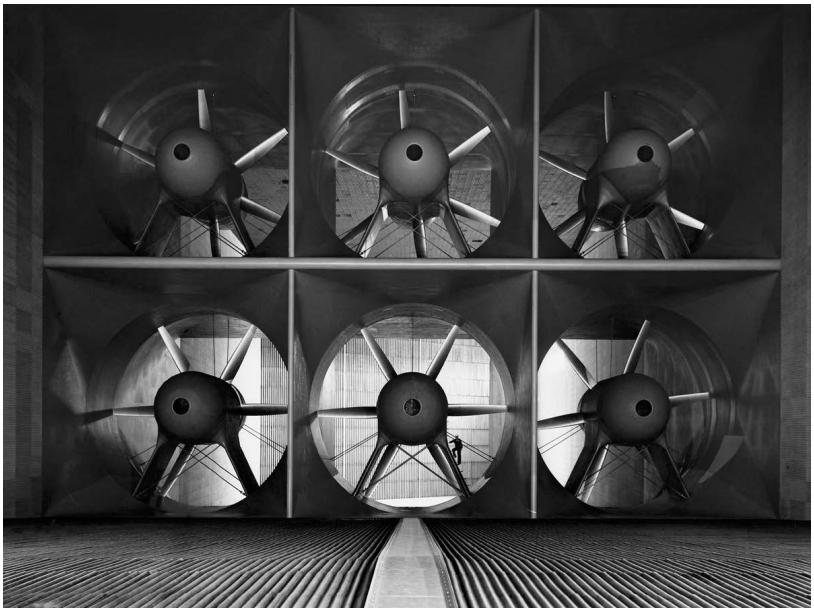

Figure 2.20 Six 40-foot diameter fans stand in the Ames 40 × 80 feet wind tunnel, https://tinyurl.com/ms8ksrw6.

A Twelve-Foot Pressure Tunnel During World War II NACA engineers at Ames decided to try combining three desirable wind tunnel characteristics in a single tunnel. These qualities were and still are:

- High Reynolds numbers
- High subsonic speeds
- Very low airstream turbulence.

The tunnel had a test section of 12-foot, but just before the test section was a large bulge, measuring 43 feet in diameter. The bulge was equipped with low-turbulence screens that smoothed out the airflow, achieving one of the goals. High-speed flow was obtained by using a 12000 horsepower electric drive system. High Reynolds numbers were reached by pressurizing the tunnel. To withstand high pressures, NACA engineers at Ame decided to use small angular steps to turn the high-speed airstream, instead of the usual sharp, mitered 90-degree corners. This stepwise construction was more durable and effective than sharp-angled turns.
Six atmospheres pressure was the goal, although this specification was later reduced to five, but to prove safety it was required to reach 9 atmospheres. For safety reason, the high-pressure integrity of this massive shell was tested by filling it with water, as while an air-filled tunnel was considered a bomb, a water-filled tunnel was safe because water is essentially incompressible. The tunnel passed the hydrostatic test successfully. Finally, the 12-foot pressure tunnel went into operation in July 1946. All the attention was focused on tunnel calibration, air velocity, air turbulence, and flow uniformity, but all performance requirements were met [19].

Figure 2.21 The 12-foot pressure tunnel with several angular stages. The spherical bulge houses the antiturbulence screens [19].

A Sixteen-Foot Twin on the East Coast In November 1940, Langley started expanding its facilities by building new West Area. It already had a 8-foot high-speed wind tunnel in operation but it was inadequate to solve many engineering problems. Consequently, plans for the construction of a twin of the Ames 16-foot high-speed tunnel — shown in Figure 2.18 — were approved. The new tunnel at Langley had to be a lower-speed version of the Ames facility because Langley did not have sufficient electrical power to run it at higher than Mach 0.7. The 16-foot tunnel, was ideal for replicating subsonic high-speed flight conditions quickly and inexpensively compared to ground testing or also actual flight. This made it perfect for solving the cooling problems encountered with aircooled aircraft engines. [19].

Low Turbulence Pressure Tunnel One more important aspect that required the attention of engineers was the level of turbulence in the wind tunnel. Particularly, analyzing wing performance, there was a gap between actual flight and wind tunnel tests. The reason for this was attributed to turbulence in Langley's wind tunnels. The wind tunnel's fans and air-guiding structures induced fine-scale random fluctuations — in contrast with gust or large scale turbulence in the atmosphere — in local air velocity and flow angle. This microscopic "weather" disturbed the thin boundary layer of air next to the surface of the wind tunnel models. Wind tunnel designers used two techniques to tranquilize microscopic air turbulence.

- The first method involved squeezing the airflow into a duct with a smaller cross-sectional area, which ironed out some of the disorderly airflow.

- The second method utilized a settling or stilling chamber upstream of the contraction section. This chamber contained honeycombs and screens to damp out turbulence.

The successor to a first test tunnel built in October 1940, was the Low Turbulance Pressure Tunnel — LTPT, shown in Figure 2.22. It was pressurized to 10 atmospheres. The test section was 7.5 × 3 feet. The contraction ratio was 17.6 to 1, and 11 screening elements were installed to reduce turbulence levels to approach those found in the natural atmosphere. In the spring of 1941 the LTPT commenced operation. Its unique low-turbulence-flow characteristics made it useful for exploring the capabilities of a revolutionary type of wing — laminar-flow airfoil [19].

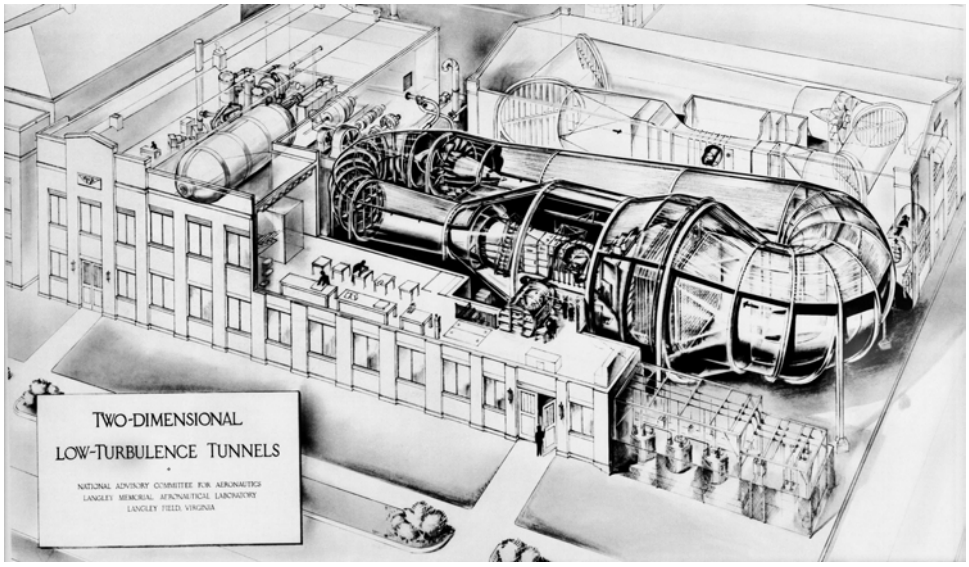

Figure 2.22 Phantom drawing of two-dimensional, low turbulence pressure tunnel, https://www.nasa.gov/feature/low-turbulence-pressure-tunnel-building-582a/, credits: NASA Langley.

Vertical Spin Tunnels The most dangerous type of tailspin is the "flat spin" in which the aircraft spins out of control towards the ground, shown in Figure 2.23. Many pilots died fighting their all but useless controls in a vain effort to recover. NACA began its spin research in the 1920s, employing three techniques:

- Drop tests of aircraft models from high buildings.
- A 5-foot vertical wind tunnel in which typical models were subjected to rotation tests.
- Flight tests of various full-scale aircraft.

The objective was to define criteria for determining whether an aircraft under design had acceptable spin-recovery characteristics. NACA built a series of two free-spinning vertical tunnels at Langley. A 15-foot diameter spin tunnel was put into

operation in 1935 and 20-foot Free Spinning Tunnel began operation in 1941. In all these tunnels, air is drawn upward through the test section by a fan at the top; after passing through the fan, the air circulates back through the test section again by turning vanes which redirect the air into an annular return passage, Figure 2.24. The 20-foot free-spinning tunnel was powered by a 1300-horsepower motor, capable of providing 100 foot per second air in the test section. The operator launched the aircraft model into the rising air by hand from a platform, imparted a spin to the model with a flick of the hand, and then adjusted the wind speed of the tunnel as the model was spinning downward. The operator continued to increase the tunnel wind speed until the model's fall was just balanced by the uprushing air. Then the control surfaces of the model, which were driven by tiny electric servo-actuators, were activated electromagnetically to initiate recovery from the spin. The images of the stabilized spinning motions and the number of turns required for recovery were documented on high-resolution video for later analysis [19].

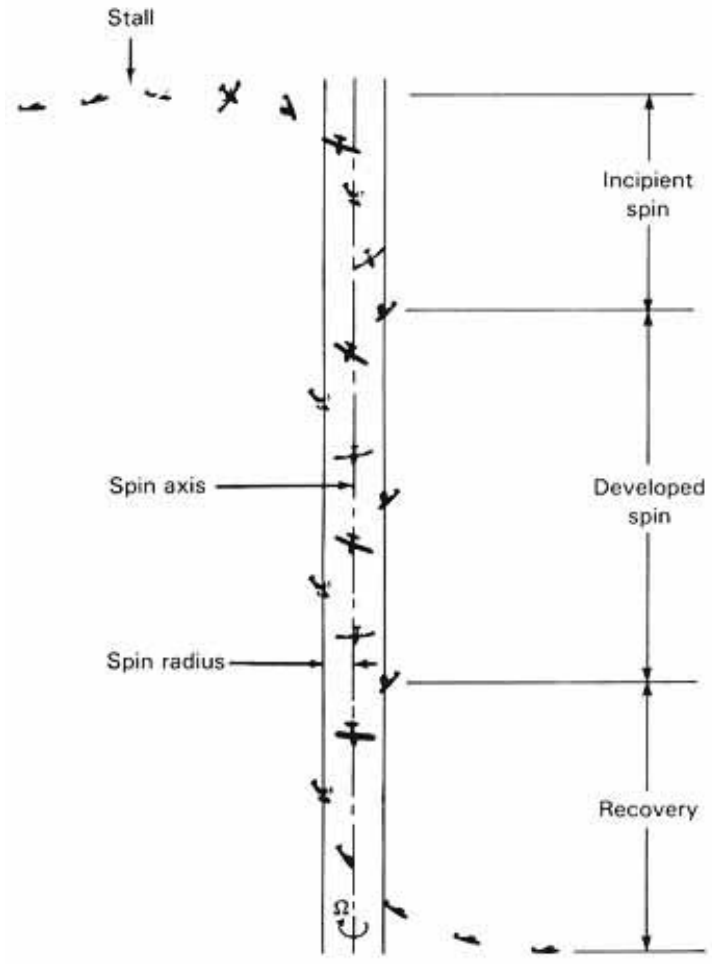

Figure 2.23 Time sequence of an aircraft in a spin [19].

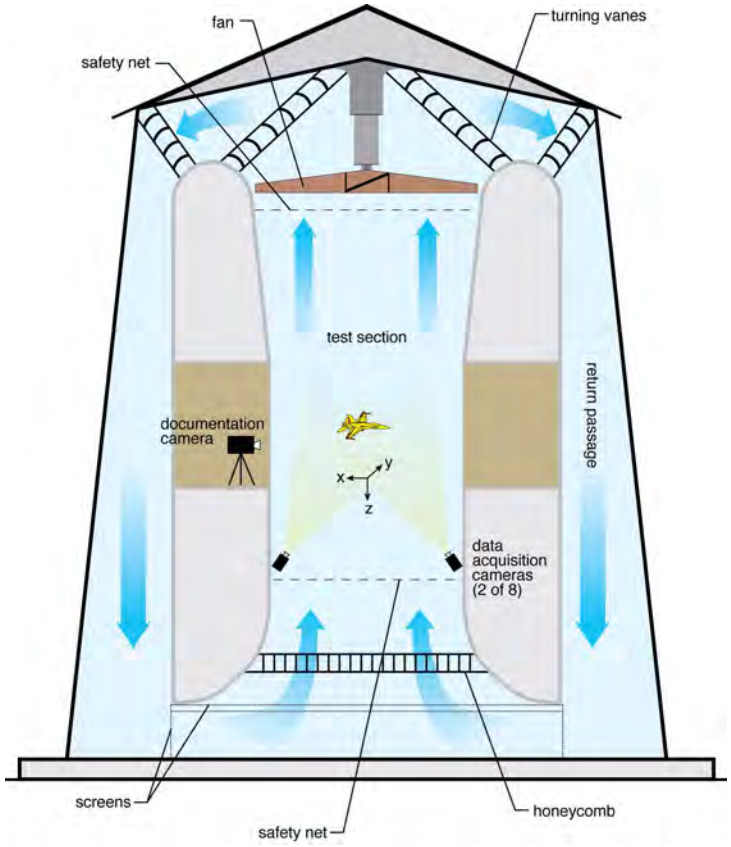

Figure 2.24 Cross section of the Langley 20-foot spin tunnel, https://www.nasa.gov/feature/20-foot-spin-tunnel-building-645/, credits: NASA Langley.

Stability Tunnel In the 1941, NACA built the Stability tunnel at Langley. It was used to study the forces encountered by an airplane during a curved flight path. The tunnel was a continuous-flow wind tunnel that featured two interchangeable test sections, each measuring about 6 feet in size. One test section had a set of rotating vanes that created a swirl in the airstream simulating the aircraft motion in rolling flight. The second test section was curved allowing for simulations of aircraft motion in curved flight. In 1958, this tunnel was moved from Langley to the campus of Virginia Polytechnic Institute and State University at Blacksburg, Virginia. Here was used as an educational and research and development tool [19].

Propulsion Tunnels Testing aircraft engines, whether reciprocating or jet, requires simulating the same conditions of the actual flight in order to accurately measure the performance of the engine. This includes simulating flight velocity, variations in atmospheric pressure and temperature. To simulate high altitude conditions, large air-exhauster pumps must be added to the conventional wind tunnel. High altitudes also mean very low temperatures — −50°F and lower — which requires a large refrigeration system to be installed. Additionally, since the engine must be operated in the tunnel, a system must also be in place to remove the hot exhaust gases from the circuit in order to maintain safe testing conditions.

During World War II, the Lewis Flight Propulsion Laboratory, near Cleveland, Ohio, tackled the task of designing an engine wind tunnel. The Altitude Wind Tunnel — Figure 2.25 — went into operation in 1944 and was used to test a turbojet engine soon after. To meet high-altitude requirements, the tunnel was equipped with four reciprocating-type exhauster units with a total of 7000 horsepower. To achieve low temperature requirements, a large 21000-ton refrigeration unit was installed, which cooled the tunnel air passing through its coils down to −50° F. The Altitude Wind Tunnel had a system in place to remove the hot exhaust gases produced by the engine under test. The exhaust air scoop downstream of the engine collected the hot combustion products and removed them from the tunnel. The lost air was replaced by injecting clean air just ahead of the engine being tested. [19].

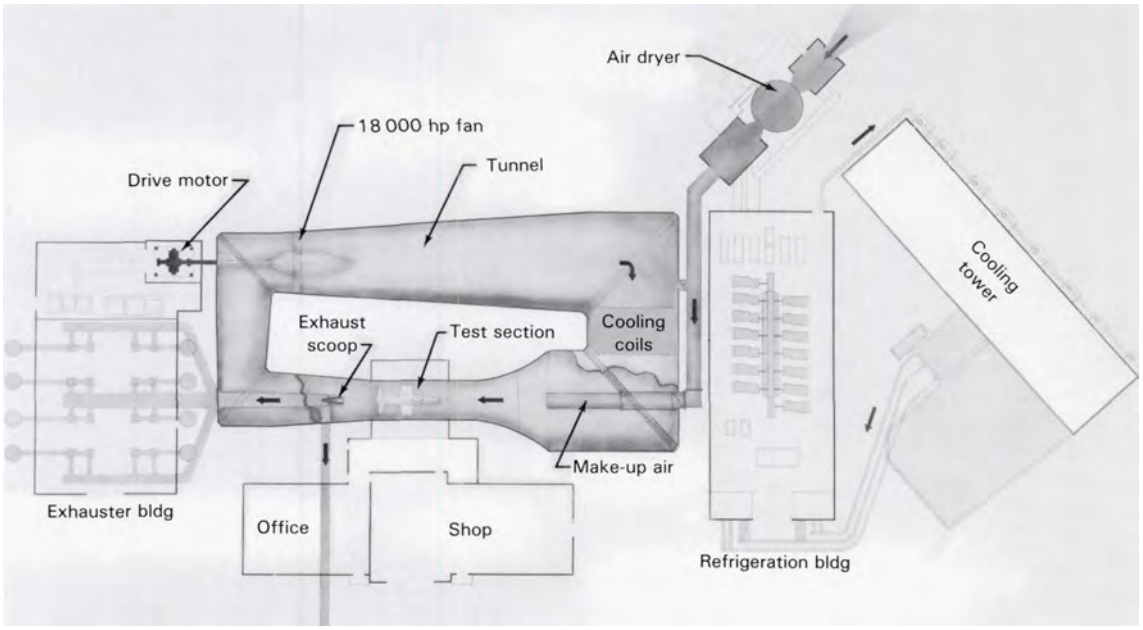

Figure 2.25 Lewis altitude wind tunnel with equipment to purge combustion products, control air pressure and reduce air temperature [19].

Icing Research Tunnel Lewis Icing Tunnel, the world's largest ice tunnel, went into operation in 1944. The increasing interest in studying ice formation on aircraft was due to the fact that ice could quickly render a plane uncontrollable, as heavy layers of ice collected on wings and control surfaces. The Lewis icing research tunnel was specifically designed to study the formation of ice on aircraft. The tunnel appeared similar to a conventional subsonic wind tunnel from the outside. It had a 4160-horsepower electric motor to generate 300 mph air in a 6 × 9 foot test section. The first departure from conventionality was the 2100-ton refrigeration system that cooled the air down to −40° F. To produce ice in the icing tunnel, it was necessary to have water vapor and droplets in the air that could condense and freeze on the aircraft surface. To create these conditions, a battery of atomizers was mounted upstream of the test section. The aircraft in the test section was thus forced to fly

through a cold, supersaturated cloud of air created by the atomizers, resulting in rapid ice buildup on the craft. As the ice layers grew, heating elements in the crucial aircraft components were activated and the detached ice shards were carried away downstream by the airflow. The whole sequence was recorded by cameras, allowing engineers to observe where the ice formed and where improvements could be made in the de-icing system.

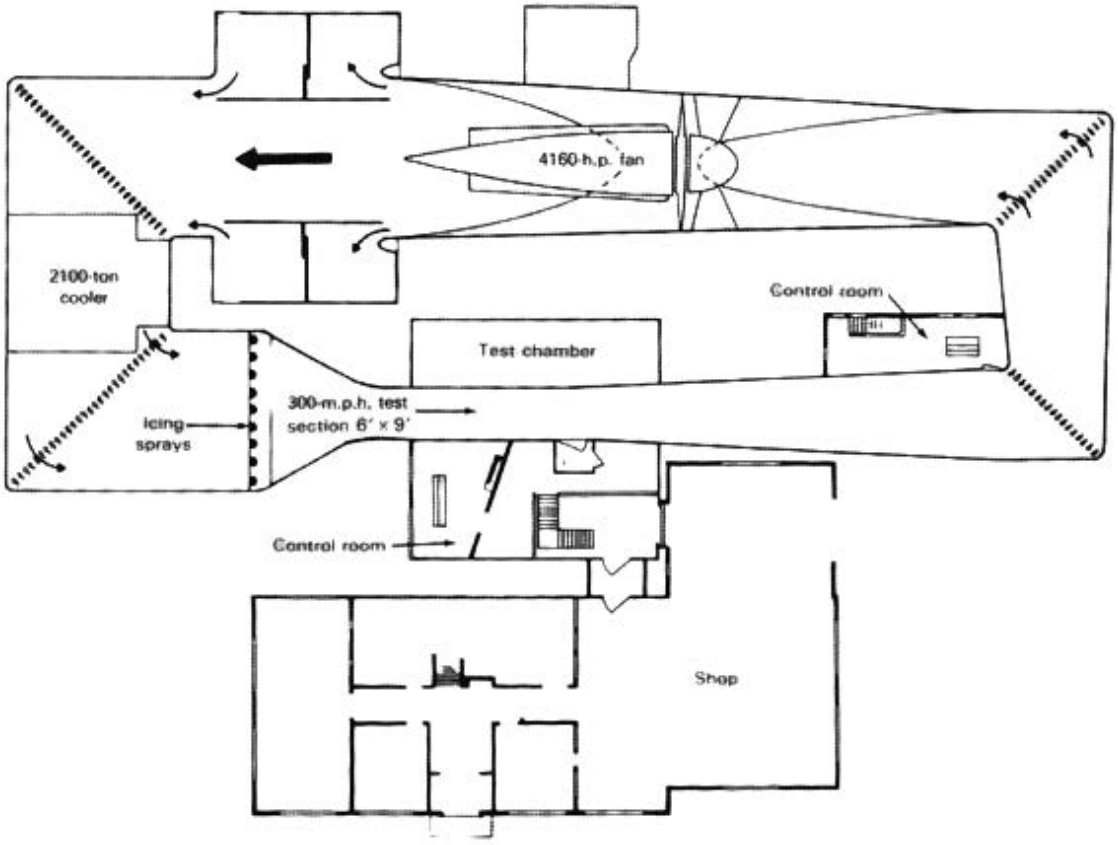

Figure 2.26 Plan of the Lewis icing research tunnel [19].

V/STOL Wind Tunnel The development of V/STOL craft for which the required test speeds must be low, has introduced new challenges for wind tunnel designers. The main problem was to prevent the strong downwash generated by powered lift systems from disturbing the flow in the test section. To overcome this problem, two solutions were adopted. One solution was to make the test section so large that the wall effects were negligible. Another solution was to use a test section with variable aperture walls that could dampen the effects of downwash. The advantages of large tunnel size were effectively exploited in the Ames 40 × 80 foot tunnel, shown in Figure 2.19 and 2.20, where full scale powered V/STOL aircraft were successfully tested.

After the modifications of some existing wind tunnels to carry out investigations on V/STOL aircraft, a new wind tunnel was built specifically for V/STOL testing

at Langley. This facility was brought on line in December 1970. The tunnel was powered with 8000-horsepower electric drive system and was able to achieve a speed of 230 mph. The test section was 14.5 feet high by 21.75 feet wide. The innovative feature was its test section walls. The walls were built on the Tinkertoy principle, which meant that they could be changed from solid to slotted to semi open simply by interchanging wall sections. This allowed the engineers to select the proper wall configuration to reduce the flow disturbances caused by the aircraft's downwash [19].

Another solution to the problem of building V/STOL tunnels was that taken for the Lockheed Martin Aeronautical Systems Co. tunnel. The Lockheed low-speed wind tunnel had a unique design that featured tandem test sections with two contractions. The first, and larger, test section dedicated to V/STOL or powered lift models and had a cross sectional area of 780 square feet with speeds from 23 to 115 mph. The second test section had a cross-sectional area of 378 square feet and speeds from 58 to 253 mph. This design avoided the need for high installed power required to drive the larger test section at high speeds. This design also resulted in an increase in the length of the tunnel, which increased the cost of the shell. [18].

Another approach to solve the problem of building wind tunnels for V/STOL testing is to use multiple interchangeable test sections, one larger test section for low-speed testing of V/STOL, and a smaller test section for high-speed testing. This approach allowed for simulating a variety of conditions. However, it had operational drawbacks, as the time required to install and remove the large inserts must be taken into account in the availability of the tunnel facility [18].

One of the least expensive methods of obtaining V/STOL capability was to use an existing tunnel return circuit for a V/STOL test section. This approach involved repurposing a section of the existing tunnel, such as the settling area ahead of the contraction cone or the end of the diffuser, to test V/STOL aircrafts. However, the flow quality in these test sections could not be as good as in a tunnel built specifically for V/STOL testing. This could be addressed by using screens and honeycombs to improve the flow quality [18].

Another approach to modifying an existing tunnel for V/STOL experiments was to add another leg or legs to the tunnel. The McDonnell-Douglas low-speed tunnel actually had three legs that allowed for changes in configuration of tunnel, creating closed or open return tunnel and open throat or closed test section. The NASA Ames 40 $\times$ 80 feet closed throat tunnel was modified by adding a new leg, creating an open circuit tunnel with a closed throat test section of 80 $\times$ 120 feet, shown in Figure 2.27. The tunnel was also repowered and new fans were built to increase the speed in both test sections [18].

2.3.3 Other wind tunnels

After the wartime, the race for speed in aircraft development led to the creation of more advanced wind tunnel technology. In the 50s, new transonic wind tunnels

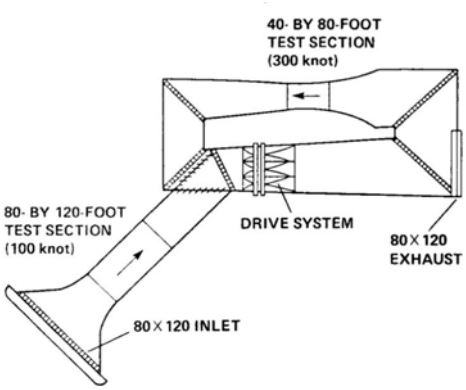

(a) *Plan View of the National Full-Scale wind tunnel* [21].

(b) *Inlet of test section 80 × 120 feet*, https://tinyurl.com/2p9khk9x, credits: Oleg Alexandrov.

Figure 2.27 NASA's wind tunnel at Ames Research Center.

(Mach number ≈ 0 to 0.7), supersonic wind tunnels (Mach number ≈ 1.2 to 5) and hypersonic wind tunnels (Mach number > 5) were developed to meet the demands of high-speed aircraft design. These facilities were necessary to support the advancement of aircraft technology and the increasing speeds at which aircraft were able to fly. The hypersonic domain mainly concerns the field of rockets or space vehicles. In addition to aircraft and space vehicle research, wind tunnels have also been used to study the effects of wind on large structures — stadiums, bridges, towers. This includes determining the forces that act on the surface of these structures and designing them to support those loads. This research helps in designing and constructing safer and more durable structures. Another application of wind tunnel concerns the automotive field. It is not so much to determine aerodynamic forces, but more to determine ways to reduce the power required to move the vehicle on roadways at a given speed, so reducing consumption and also pollutant emissions [19, 20]. In this section, other wind tunnels developed over the years have been briefly reported, as they are not the subject of our work.

3

Wind Tunnel Setup

Contents

3.1 The DII wind tunnel

The experimental tests campaign has been performed in the main subsonic wind tunnel facility of the Department of Industrial Engineering (DII). This is a subsonic, closed circuit and single return tunnel. It has a closed test section with a tempered rectangular section. The main wind-tunnel characteristics are summarized in Table 3.1.

The DII wind tunnel is shown in Figure 3.1. The main components of this wind tunnel are described in the following, where the capital letters refer to the plan view in Figure 3.2.

Test section It is 4 m long, 2 m wide, and 1.4 m high. This is a rectangular with tempered corners and a cross-section of 2.68 m^2. Sections from A to B.

Table 3.1 Wind tunnel of the DII, main characteristics.

	Value
Test section dimensions	2.0 m × 1.4 m
Maximum available wind speed	50 m/s
Turbulence level	0.10%
Maximum power	150 kW

Figure 3.1 Main subsonic wind tunnel facility.

Diffuser There are three diffusers in order to slow down the airflow coming from the test section. The first diffuser — from B to C — has a length of about 5 m and an expansion angle of about 3° and it links the last section of the test section to the first corner. The second diffuser — from D to E — is placed between the first two corners and has a length of about 1.8 m. The last diffuser — from G to I — is the longest one, about 14 m; it increases the tunnel section with an expansion angle of about 3°, and it is placed between the second and the third corner.

Safety screen It is placed immediately before the first corner, section C, with the aim to protect the turning vanes against any possible object or scrap that could be lost by the model in the test section, as shown in Figure 3.3. The screen has squared cells of about 13 mm per edge, shown in Figure 3.4.

Corners The first corner — from C to D — is placed behind the first diffuser and has a constant section. It incorporates turning vanes with a chord of about 450 mm and a maximum thickness of 14.4%, shown in Figure 3.3 and Figure 3.4. The second corner — from E to F — is placed behind the fan and is equipped with tabs

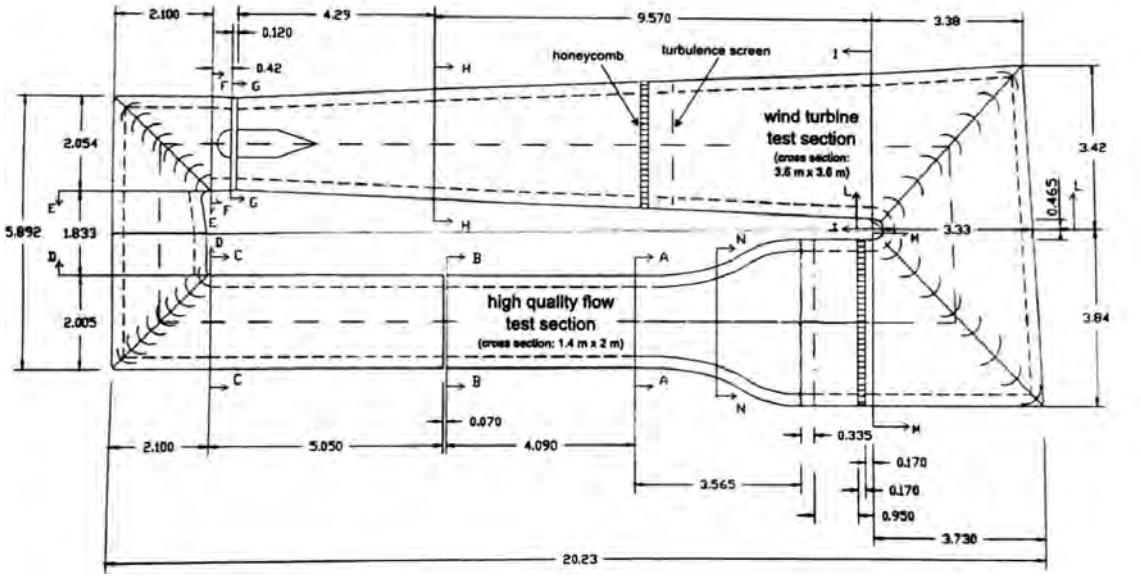

Figure 3.2 Plan View of the DII wind tunnel.

having a chord of about 490 mm and maximum thickness of 13.3%. The second corner section is slightly divergent, such as the third and the fourth corner. The third corner — from I to L — has diverters with a chord of 925 mm and maximum thickness of 17.3%. The fourth corner — from L to M — has tabs with a length of 875 mm and a maximum thickness of 18.3%.

Fan It is placed immediately ahead of the second corner — form E to F. Upstream the six blades propeller, a four blade flow straightener ring is placed. The ogive of the fan has a maximum diameter of 700 mm.

Honeycomb flow straighteners They are elliptical section cells placed at the beginning of the stagnation chamber. Section M.

Turbulence control screen It has the function to reduce the turbulence axial component of the flow in the test section allowing a turbulence level of 0.10%.

Stagnation chamber It has a length of 0.035 m and it is placed ahead of the nozzle. Section M.

Nozzle It has a length of 3.56 m, with an inlet section of about 12.7 m^2 and an outlet section of 2.7 m^2, with a ratio of 4.83. Sections from M to N.

Figure 3.3 Photo of the first corner of the DII wind tunnel just located after the test section. It is easy to observe the turning vanes and the safety screen installed.

Figure 3.4 Further details of the the turning vanes and 13 mm square mesh safety screen of the DII wind tunnel.

3.2 Wind tunnel measurements

The experimental test campaign in the DII wind tunnel is carried out using the instrumentation to obtain forces and moments acting on the model. This instrumentation can be divided in: measurement, control, data acquisition and elaboration.

3.2.1 Measurement instrumentation

The measurement instrumentation consists of two internal strain gage balances for the measurement of aerodynamic forces and moments, a Venturi system to measure the dynamic pressure, an inclinometer to read the longitudinal attitude of the scale model, and finally a temperature probe to measure the static temperature in the test section. Some details are given in the following.

Internal strain gage balance It has three channels and it is used to measure the aerodynamic forces and moments. In detail, it is used for longitudinal measurements of lift, drag, and pitch moment. It is made from an Al-2024-T3 aluminum block, shown in Figure 3.5.

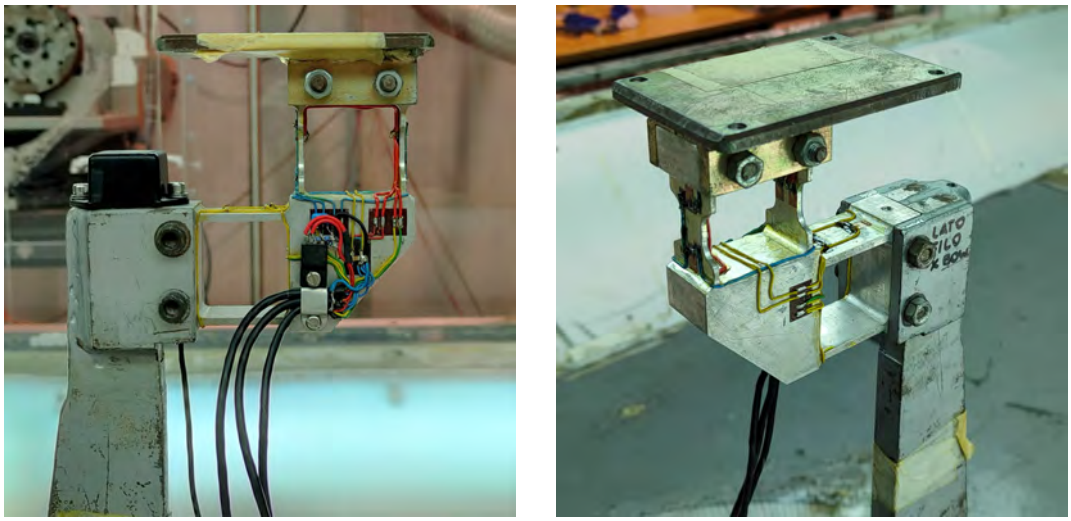

Figure 3.5 Longitudinal strain gage balance.

As Ciliberti declared in his work [22], the calibration process has been previously performed by Corcione [23], who followed the procedure described in the book of Barlow, Rae, and Pope [18]. The matrix form obtained through this process is:

$$F_R = [K_{ij}]F_B \tag{3.1}$$

In this equation, the matrix coefficients K_{ij} relates the load applied to the balance — subscript B — to the balance output reading — subscript R. The previous Equation (3.1), can be inverted to give:

$$F_B = [K_{ij}]^{-1} F_R \tag{3.2}$$

This is the required equation to determine forces and moments applied to the balance by the model, starting from the balance output reading. Finally, the calibration matrix for longitudinal balance has been found, and it is:

$$[K_{ij}]^{-1} = \begin{bmatrix} -12.78263909 & -0.099295936 & 0.036182262 \\ -0.004186418 & -2.06815302 & 0.004097632 \\ 0.052723359 & 0.159755039 & 4.938539268 \end{bmatrix} \tag{3.3}$$

The calibration procedure is also essential to estimate the balance center in order to transfer forces and moments to the desired reference point, e.g. the 25% of wing m.a.c. Table 3.2 summarizes the maximum error found for the balance readings after the calibration procedure. The maximum error in average is about 0.1% of the full scale maximum load of each measured force or moment.

Table 3.2 Strain gage balances margin of error.

Force/Moment	Max. Error	Full scale
Lift	0.05 kgf (0.06%)	80 kgf
Drag	0.03 kgf (0.15%)	20 kgf
Pitching moment	0.02 kgf × m (0.1%)	20 kgf × m

Venturi The wind tunnel of the DII is equipped with 4 static pressure probes placed on both faces of initial and final sections of the nozzle. A pressure transducer (with 2500 Pa full scale and 3 Pa accuracy) measures the static pressure variation between these sections and, through the continuity equation, gives the dynamic pressure at the exit of the nozzle. Several tests without the model in the test section and at different air speeds have shown that the dynamic pressure measured at the end of the nozzle must be increased by a value of 1.09 to obtain the actual dynamic pressure in the test section. Since it is impossible to use a Pitot probe to measure the dynamic pressure in the test section in presence of the scale model — the test section should be long enough to guarantee that the measure is not affected by the pressure field produced by the model in the test section — the only available measure of the dynamic pressure is obtained by the Venturi, thus the above-mentioned 9% increase is assumed to be valid also with the model in the test section.

Inclinometer It is the uni-axial tilt sensor CXTLA01, produced by CrossBow (San Jose, CA, USA). The sensor uses a micro-machined acceleration sensing element with a DC response to measure inclination relative to gravity, in other words, through the component of the gravity acceleration that lies in the plane of the instrument, it goes back to its inclination. The inclinometer has been mounted on the sting of the wind tunnel balance, Figure 3.6.

Figure 3.6 The CrossBow inclinometer mounted on the balance sting.

Temperature probe It consists of a flush wall-mounted probe for the measurement of the static temperature in order to determine the true test section speed through the use of Bernoulli's incompressible equation and to obtain the mass density through the equation of state. Due to the absence of a heat exchanger in our wind tunnel, it is crucial to consider the impact of temperature as detected by the aforementioned probe. This is because an increase in temperature reduces the density which results in a decrease in both dynamic pressure and Reynolds number.

3.2.2 Control instrumentation

In our test campaign, the control instrumentation used is the longitudinal attitude control system.

Longitudinal attitude control system The pitching mechanism is an electromechanical system lead by PC. It is placed outside the model, below the floor of the test section and it is linked to the assembly of balance-model through the sting, as shown in Figure 3.7. It was internally made to the laboratory of the DII. The system consists of an electrical stepper, which allows a sting angular excursion from $-20°$ to $20°$. The control is managed by a PC. Digital signals are generated using LabVIEW software and are sent to the National Instruments multifunction I/O device — NI USB-6341 device. Through an amplifier they reach the stepper motor. The system uses the above mentioned CrossBow Tilt sensor to measure the pitching attitude. The output signal of the inclinometer is acquired by an A/D converter and sent to the PC.

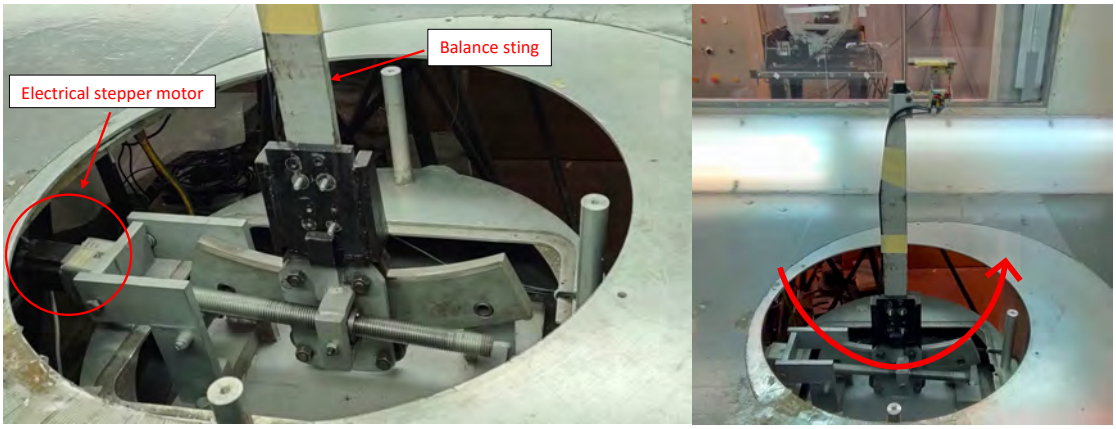

(a) *Electrical stepper motor for pitching attitude control.* **(b)** *Balance sting mounted on the pitching control system.*

Figure 3.7 Longitudinal attitude control system.

3.2.3 Data acquisition system

The instrumentation for data acquisition and processing consist of:

- a 16 channels NI USB-6341 device, produced by National Instruments, for the acquisition and conversion into 16 bit of output data coming from the measurement instrumentation;
- a PC with Windows 10 connected via USB to the aforementioned device;
- a software for the elaboration and visualization of the acquired data. The software has been developed with LabVIEW by the author and his tutor during the internship period.

3.3 Data acquisition software

LabVIEW (Laboratory Virtual Instrumentation Engineering Workbench) is a software developed by National Instruments (NI). LabVIEW programming environment simplifies hardware integration for engineering applications so it is easy to acquire data from NI and others hardware. Advanced control and data analysis algorithms can be developed with math and signal processing functions to convert the acquired data into meaningful information. At this scope, a data acquisition virtual instrument — named `DAQ_Long` — has been developed to measure and process the aerodynamic forces in the wind tunnel. This software is tailored to the measurements of the longitudinal aerodynamic characteristics of the test article, i.e., lift, drag, and pitching moment. The main parts of this virtual instrument and their functions are briefly described below, under the premise that all the acquired data are analog signals.

Initially, a communication channel is established with the NI USB-6341 data acquisition device to measure the voltage of normal force, axial, pitching moment, angle of attack, temperature, and dynamic pressure signals. In addition, a clock defines the numbers of samples to be acquired for each channel and the sampling frequency in samples per channel per second. In this initial phase, the calibration matrix (3.3) and a file of model and tunnel parameters (see Table 3.3) are also loaded. Various useful values for subsequent calculations are stored in the latter. What has been described is performed by the code shown in Figure 3.8.

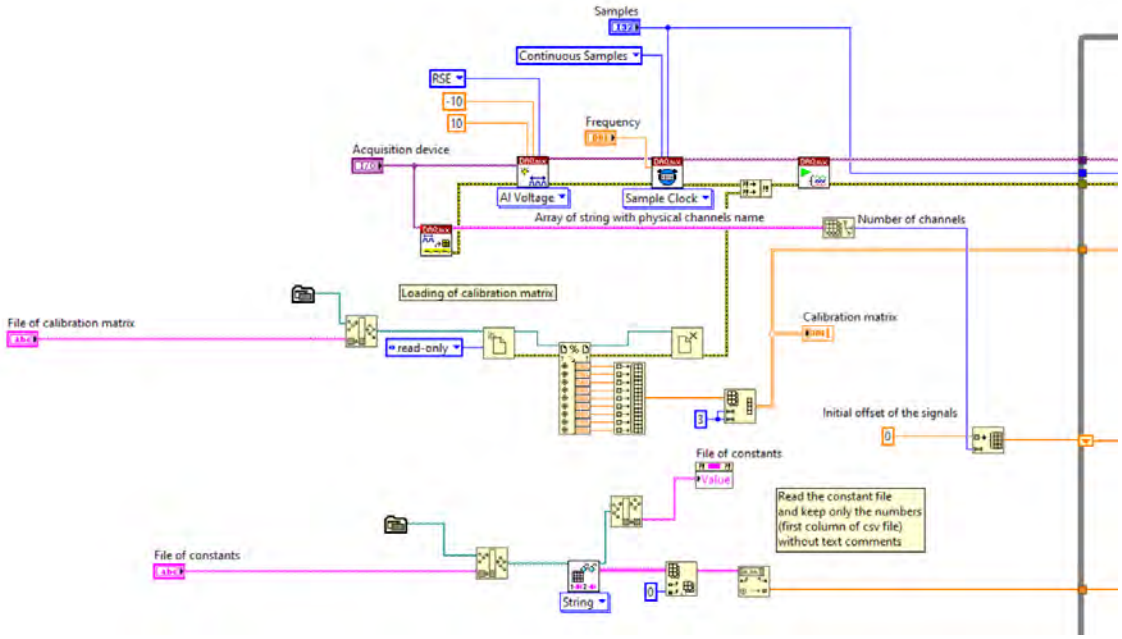

Figure 3.8 Creation channel for acquisition of signals and loading of calibration matrix and file of constants.

Table 3.3 File of constants for the wing-body configuration given in input to the LabVIEW program.

0.25	reference surface (m^2)
0.171	reference chord (m)
0.0	position x of the moment reduction pole with respect to the balance centre
0.028	position z of the moment reduction pole with respect to the balance centre
1.5	wing span (m)
0.0	—
0.0	—
0.049	horizontal tailplane surface
0.466	horizontal tailplane span
0.0	wing sweep angle at $c/2$
10.8	horizontal tailplane sweep angle at $c/2$
0.0	pitch setting alfa
0.0	wind tunnel vein
1.09	Venturi correction
0.003717512	ϵ_{sb} epsilon solid blockage
0.0206	C_{D_0} (if unknown, write zero, i.e.: 0)
0.113	δ wall correction
2.680	wind tunnel area
−0.0005	buoyancy C_D
0.0000321	$\Delta C_{D_{\mathrm{wb}}}$
0.068	$\tau_{2,\mathrm{w}}$
0.0	$\tau_{2,\mathrm{t}}$
0.0	$\mathrm{d}C_{M_{\mathrm{tail}}}/\mathrm{d}\alpha$ pitching moment curve slope of the horizontal tailplane
−9.900	calibration constant of inclinometer 1
2.299	zero inclinometer 1
22.727	calibration constant of inclinometer 2
−5.05	zero inclinometer 2
403.8	calibration constant of pressure transducer
0.0080782	zeroing coefficient F_{X_0}
0.44113	zeroing coefficient F_{X_1}
0.0001914	zeroing coefficient F_{X_2}
−0.00035837	zeroing coefficient F_{Z_0}
0.00054144	zeroing coefficient F_{Z_1}
0.0038652	zeroing coefficient F_{Z_2}
0.00032634	zeroing coefficient M_{Y_0}
0.016555	zeroing coefficient M_{Y_1}
−0.00025397	zeroing coefficient M_{Y_2}
5.0	calibration constant of potentiometer
3.3263	zero potentiometer

Later on, inside the `while loop` represented by a thick gray outline, the voltage signals are read as waveforms from input channels. Furthermore inside the `for loop`, the average of the values related to each channel is computed within the sampling buffer. Finally, the reset of the voltage signal is carried out by subtracting a previously saved voltage value from the voltage values acquired at any instant. This operation is usually made at wind tunnel off, with the model at zero angle of attack, and it is named "taking the zero" or "tare", that is all the signals — except for the temperature and attitude signals, which have absolute reference values — are referenced to that specific set of values. What has been described is performed by the code shown in Figure 3.9.

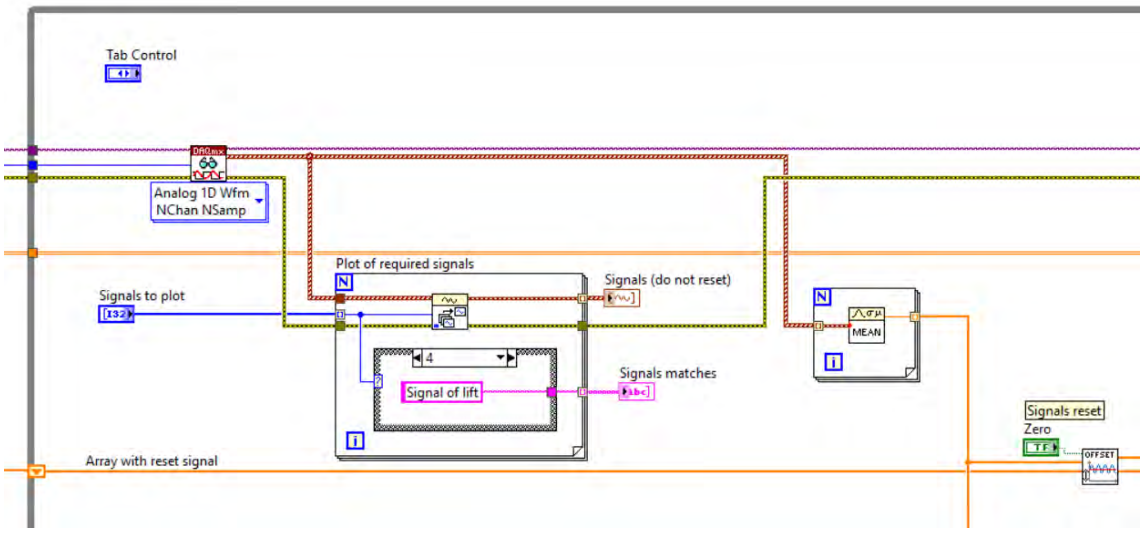

Figure 3.9 Read, mean, and reset of signals.

Then, by multiplying the calibration matrix by the signals relating to the normal force, axial force, and pitching moment, it is possible to obtain the measured vector of forces and moment applied to the balance by the model, as shown in Equation (3.2). Furthermore, the unweighted or net forces/moments, indicated by the subscript `tar`, are evaluated by considering the force containing the weight effect minus the product of the matrix of the weighting coefficients — in this case, specific for the wing-body configuration — by the vector of the angle of incidence, as shown in Equation (3.4).

The matrix of the weighting coefficients is contained inside the file of constants. These coefficients are defined before observing the effect of the wind on the test model, using a LabVIEW code — called `taraPesi.vi`. This code is similar to and simpler that the one described here, and it was developed at the same time. In other words, `taraPesi.vi` returns the aforementioned coefficients of the second order polynomial — specific to a particular model configuration — that best fits the data set (α, F_x), (α, F_z), (α, M_y), where now α, F_x, F_z, M_y are vectors acquired by

varying α in the absence of the wind speed effect and with only the force of gravity acting on the test model.

Lastly, the evaluation of drag and lift is performed by multiplying the previously calculated normal and axial forces by the rotation matrix of the angle of attack:

$$\begin{bmatrix} F_{x_{\text{tar}}} \\ F_{z_{\text{tar}}} \\ m_{y_{\text{tar}}} \end{bmatrix} = \begin{bmatrix} F_x \\ F_z \\ M_y \end{bmatrix} - \begin{bmatrix} 0.0080782 & 0.44113 & 0.0001914 \\ -0.00035837 & 0.00054144 & 0.0038652 \\ 0.00032634 & 0.016555 & -0.00025397 \end{bmatrix} \begin{bmatrix} 1 \\ \alpha \\ \alpha^2 \end{bmatrix} \tag{3.4}$$

What is described above is carried out by the following piece of code, shown in Figure 3.10.

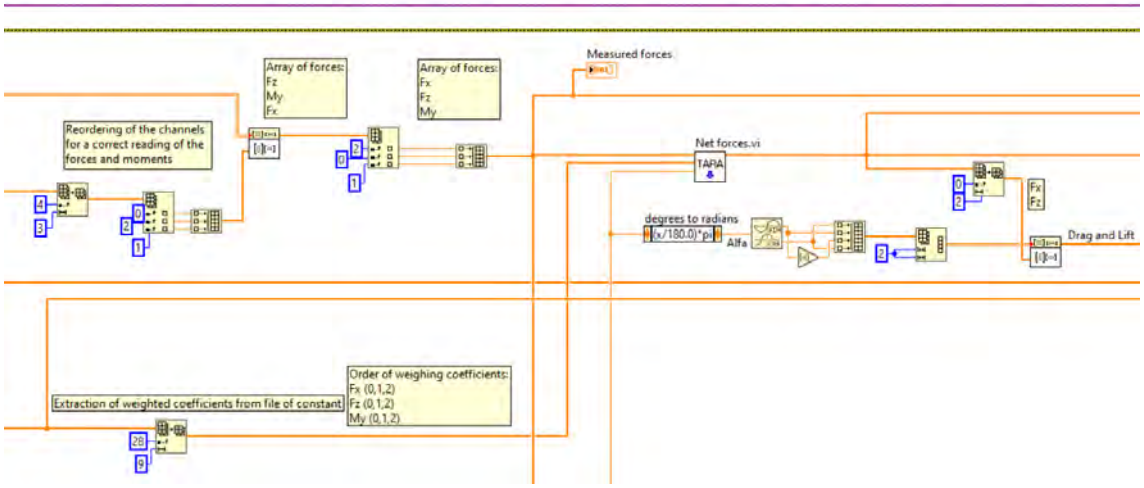

Figure 3.10 Measured forces, net forces, drag and lift evaluation.

The next step is the evaluation, through the following MathScript, of the coefficient of lift, drag, and pitching moment, the speed in the wind tunnel and the Reynolds number, as shown in Figure 3.11. This MathScript takes as input values previously calculated or defined in the file of constants, uses them in the various expressions, and generates some output values.

In details, $C_{M_{\text{cb}}}$ is the moment coefficient referred to the balance center. It is calculated using $m_{y_{\text{tar}}}$, which is the pitching moment referred to the balance center and is defined by Equation (3.4). Meanwhile, $C_{M_{\text{polo}}}$ is the moment coefficient referred to the pole of moments. It is calculated using $M_{y_{\text{trasp}}}$, value defined in Equation (3.5). This is the transport moment evaluated in the reference points of moments, which is for our case is chosen at 25% of the wing mean aerodynamic chord along the longitudinal axis and 20% of the wing mean aerodynamic chord

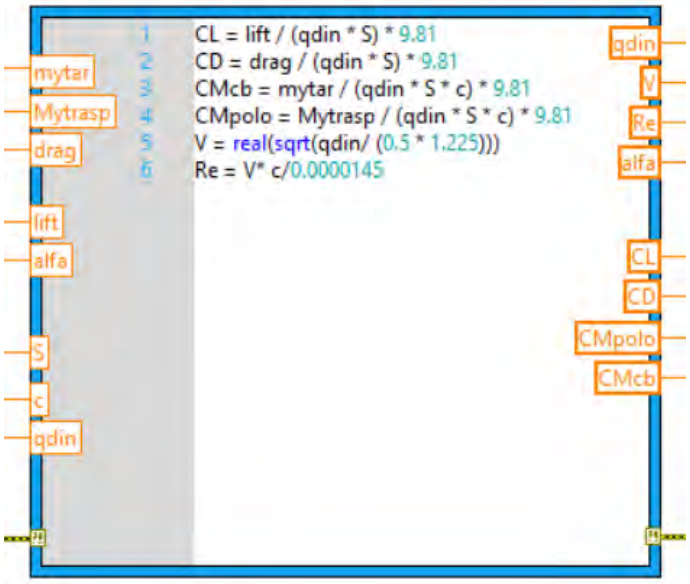

Figure 3.11 MathScript module for evaluating aerodynamic coefficients, wind speed and Reynolds number.

along the vertical axis, below the the wing mean aerodynamic chord plane. This point is defined as the reference point for the calculation of the aerodynamic forces and moments:

$$M_{y_{\text{trasp}}} = m_{y_{\text{tar}}} + F_{z_{\text{tar}}} \cdot x + F_{x_{\text{tar}}} \cdot z \tag{3.5}$$

The distances are referred to a coordinate system with origin at the balance centre, x-axis is directed along the nose of the model and parallel to the balance plate, y-axis is positively oriented in the right wing direction, z-axis is orthogonal to the first two and is positively oriented downward.

The x coordinate is defined as the distance along the longitudinal axis between the balance center and the chosen reference point. The z coordinate is defined as the distance along the vertical axis between the balance center and the chosen reference point. These two positions are estimated with the aid of the CAD model.

Finally, the corrected aerodynamic coefficients are evaluated using a further MathScript, shown in Figure 3.12. Like the previous MathScript, input values can be given and used within the equations to obtain the values of the corrected coefficients as output. These applied corrections are mathematically and physically deepened in the subsection 3.4.1.

Another clarification relates to the part of code used for creating, writing, saving the output files and the coded part to manage the appearance of the switch and buttons on the front panel. These parts are omitted because they are not relevant to the purposes of this work.

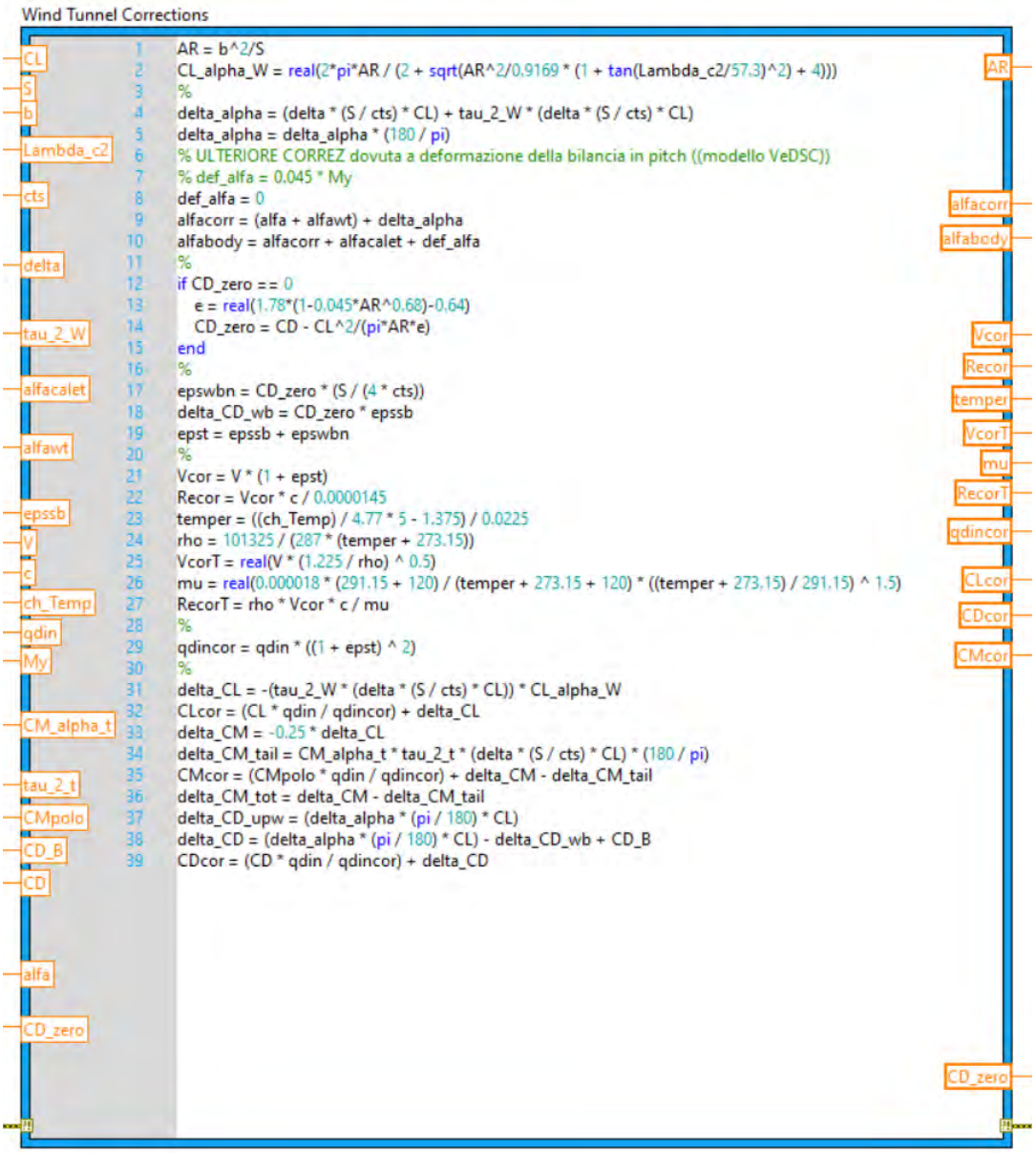

Figure 3.12 MathScript module for wind tunnel corrections, more information in the subsection 3.4.1.

For completeness, the graphic part of the code previously illustrated is shown in Figure 3.13 and in Figure 3.14. By means of the buttons shown in these figures, it is possible to acquire the aerodynamic data by clicking on the `ACQUIRE` button, which is only enabled when the `Save file?` switch is set to `YES`. Each time the `ACQUIRE` button is pressed, a counter is incremented to remind the user of the number of acquisitions made. The name of the file to be saved must be defined in the dedicated text box prior to the run of the virtual instrument. Setting a voltage signal to zero can be done by clicking on the `ZERO` button, as discussed previously

for the code in Figure 3.9. And finally, the `STOP` button can be pressed when the continuous reading of the input signals needs to be interrupted, in other words, when the `while loop` needs to be terminated.

Figure 3.13 Front panel for managing the acquisition settings and displaying the acquired voltage signal.

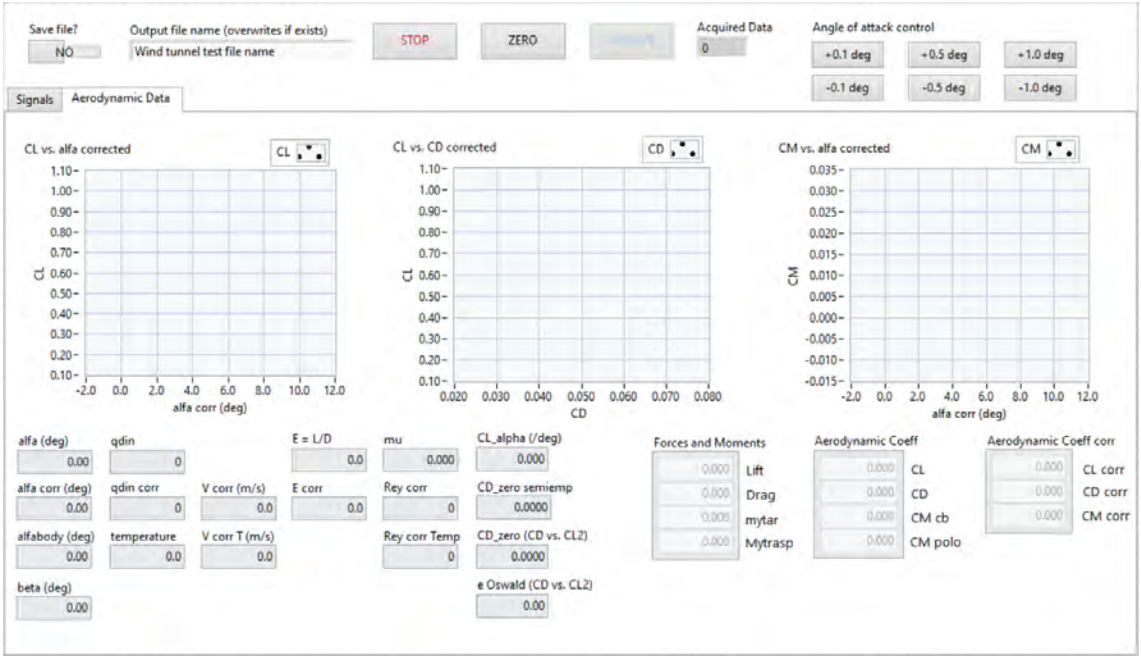

Figure 3.14 Front panel for displaying the calculated aerodynamic quantities and the acquired aerodynamic coefficients.

3.4 Wind tunnel corrections

The flow conditions in a wind tunnel are quite different, due to the presence of solid walls, from an unbounded airstream or in a "free-air" in the case of aircraft or in an environment with only one plane boundary, as may be supposed for ground vehicles. While there is no difference in having the model at rest and the air moving around it, the distances of some or all of the stream boundaries from the article under test are usually less than the corresponding distances for actual operations. In addition, the flow properties in the test section may not be the same in space and time. The presence of solid walls at a finite distance from the body under investigation produces various effects that must be considered in order to be able to apply precise corrections [18]. These effects are defined as follows:

Horizontal buoyancy It refers to a variation of static pressure along the test section induced by the lateral boundaries, when no model is present. In a closed-throat wind tunnel, as a result of a thickening in the boundary layer, there is a variation in static pressure along the axis of the test section. This effect causes an increase in drag and is known as the buoyancy effect. This drag force is analogous to the hydrostatic force on objects in a stationary fluid in a uniform gravitational field.

Solid blockage It is defined as the ratio of the "frontal area" of the article to the stream cross sectional area. In real flight, this is effectively zero due to the absence of solid walls, while in wind tunnel, it is usually chosen in the range of 0.01–0.10. Essentially, the wind tunnel is a tube where the model in the test section "chokes" the flow. This is the most relevant effect; the "blockage" produces a variation in the oncoming speed or dynamic pressure. Furthermore, this effect causes surface stresses larger than the corresponding free-air operations in the case of a closed test section and smaller for an open jet. It is assumed that this "blockage" does not generate any variation on the surface stress distribution.

Wake blockage Every body immersed in a moving fluid generates a wake. The size of the wake is a function of the body shape and the ratio of the wake area to the tunnel area. The wake has a lower mean velocity than the free stream. According to the law of continuity, the velocity outside the wake in a closed tunnel must be higher than the free stream. By Bernoulli's principle, the higher velocity in the main stream has a lowered pressure. This lowered pressure that occurs when the boundary layer — which later becomes the wake — grows on the model, puts the model in a pressure gradient, hence there is a velocity increment on the model. This wake blockage, in a closed test section, increases the measured drag. In other words, it leads to an overestimation of the drag.

Streamline curvature It refers to an alteration in the curvature of the streamlines of the flow around a body in a wind tunnel compared to the corresponding curvature in an infinite stream. In a closed tunnel, lift, pitching moment, hinge

moments, and angle of attack are increased.

Normal downwash change It is referred to the component of the induced flow in the lift direction at the test article. The downwash is changed due to the finite distances to the boundaries. A closed jet makes the lift too large and the drag too small at a given geometric angle of attack corresponding to a smaller downwash at the test article than in an unbounded stream.

Spanwise downwash distortion It refers to an alteration in the local angle of attack along the span of a lifting wing. In a closed test section the angles of attack near the wingtips of a model with large span are increased, making tip stall start at a lower geometric angle of attack. However, this effect becomes negligible by keeping the model span less than 0.8 tunnel width.

Tail downwash change It refers to an alteration in the normal downwash behind the wing. In a closed jet, the wing wake location is higher than in free air and the model increases its static stability.

3.4.1 Mathematical models

The purpose of this section is to describe the corrections that should be applied to the force and pressure measurements obtained from the wind tunnel tests. It is worth noting that the same corrections have already been introduced in the MathScript shown in the Figure 3.12. However, the hardware, software, and wind tunnel corrections evolved from the original data acquisition system of the wind tunnel facility, having been available for 25 years and requiring an upgrade. In the following, the classic wind tunnel corrections suggested in literature are discussed, together with some modifications made for the virtual instrument described in the previous section.

Original corrections

The main idea of this section is that the corrections implemented so far have additional approximations, compared to what is described in the literature. For example, the book of Barlow et al. [18] only uses the wing lift coefficient C_{L_w} in the correction of the angle of attack, while, to keep a straightforward operational procedure and estimate wind tunnel corrections on the fly, the data acquisition software calculate such corrections with the whole value of the C_L, whatever the aircraft components tested. To make the text easier to understand, comparisons with the reference text will be added in the footer. The corrections are applied in the following sequence:

1. effects of solid blockage ϵ_{sb} and wake blockage ϵ_{wb}
2. dynamic pressure q_c/q
3. angle of attack $\Delta\alpha$

4. lift coefficient ΔC_L
5. aerodynamic drag coefficient ΔC_D
6. aerodynamic pitching moment ΔC_M

In the following, the corrections for each effect are quantified.

Solid blockage It is the most important effect. It depends on the size of the model compared to the volume of the test section. This effect increases the effective velocity of the air on the model, and consequently the dynamic pressure. It is the sum of the blockages caused by the individual components:

$$\epsilon_{\text{sb},i} = \frac{K_1 \tau_1 (\text{wing volume})_i}{C^{3/2}} \quad \text{or} \quad \frac{K_3 \tau_1 (\text{body volume})_i}{C^{3/2}} \tag{3.6}$$

$$\epsilon_{\text{sb}} = \sum_i \epsilon_{\text{sb},i} \tag{3.7}$$

where K_1 and K_3 are shape factors, defined using charts in Ref. [18, §10.2], the quantity τ_1 is a factor that depends on the shape of the tunnel test section and the model span-to-tunnel-width ratio. It is evaluated using another chart in [18, §10.2], C is the cross-sectional area of the tunnel test section.

Wake blockage It is usually a negligible effect compared to the previous one. This effect depends on the wake of the test model, which causes an increase in the effective velocity of the air on the model and an increase in the aerodynamic drag in the wind tunnel with closed test section. Each individual component has a wake blockage described by Equation (3.8), while the total wake blockage is expressed by Equation (3.9):

$$\epsilon_{\text{wb},i} = \frac{S}{4C} C_{D0,i} \tag{3.8}$$

$$\epsilon_{\text{wb}} = \sum_i \epsilon_{\text{wb},i} \tag{3.9}$$

where the parameter S is the planform area of the wing. To estimate ϵ_{wb}, it is required the evaluation of the drag coefficient at zero lift C_{D_0}[2].

Drag coefficient at zero lift It is evaluated by the difference between drag coefficient C_D, defined by reducing the drag force in the usual form, and the induced drag $C_{D_i} = f(C_L^2)$. The Oswald factor e must be assumed. The following formula is applied for small angles of attack[3]:

$$C_{D_0} = C_D - \frac{C_L^2}{\pi \text{Æ} e}, \quad \alpha \leq 5^\circ \tag{3.10}$$

[2]The formula is valid for attached flows. Barlow et al. [18] suggested an equation that includes the C_{D_u} — uncorrected drag coefficient — which takes into account separated flow. Instead, Rogers [24] considered blockage to be independent of lift and ignored vortex drag as long as the flow is attacked. Therefore, he suggested $C_{D_0} \approx C_{D_\text{u}}$.

[3]Ref. [18] suggested using a linear regression on the C_{L_u} and C_{D_u} data from a preliminary test to obtain C_{D_0} and e.

Velocity and dynamic pressure correction Considering the effects of solid and wake blockages, the flow speed becomes:

$$V_c = V(1 + \epsilon) \tag{3.11}$$

where

$$\epsilon = \epsilon_{sb} + \epsilon_{wb} \tag{3.12}$$

and the dynamic pressure then becomes:

$$q_c = q(1 + \epsilon)^2 \tag{3.13}$$

Angle of attack correction It is the sum of *upwash* correction and *streamline curvature* correction as a function of the lift coefficient[4]:

$$\Delta\alpha = \Delta\alpha_{up} + \Delta\alpha_{sc} = \delta\frac{S}{C}C_L + \tau_{2,w}\,\delta\frac{S}{C}C_L = \delta\frac{S}{C}C_L(1 + \tau_{2,w}) \tag{3.14}$$

where δ is the *boundary correction factor*, which can be found in a figure in [18, §10.7]. The quantity $\tau_{2,w}$ is a factor used to manage the amount of correction and is referred to the wing. Generally, the value of τ_2 is the effect of streamline curvature on the angle of attack and can be found using charts reported in [18, §10.8] with $\bar{c}/4$ as the tail length needed to determine τ_2.

The corrected angle of attack at which the model operates is therefore given by the sum of the geometric angle of attack and the correction due to the alteration of the streamlines caused by the walls of the closed test section:

$$\alpha_c = \alpha + \Delta\alpha \tag{3.15}$$

Lift coefficient correction The lift coefficient is corrected by multiplying the variation due to the effect of streamline curvature by the wing lift curve slope (which should be estimated beforehand):

$$\Delta C_L = \Delta\alpha_{sc}\, C_{L_{\alpha,w}} = \tau_{2,w}\delta\frac{S}{C}C_L\, C_{L_{\alpha,w}} \tag{3.16}$$

The effect is subtracted from the value measured by the wind tunnel balance. In other words, in a closed test section, due to the combined effect of altering the direction of the current lines and reducing the downwash, the lift produced is greater than that actually expected on the model at the same (corrected) angle of attack. The corrected lift coefficient then becomes:

$$C_{L_c} = C_L\frac{q}{q_c} - \Delta C_L \tag{3.17}$$

[4]In the original formulation proposed by Barlow et al. [18], there is only the wing lift coefficient $C_{L,w}$ and not the total lift coefficient, C_L.

In Equation (3.17), the uncorrected C_L is first corrected for the blockage effect, then the correction of the walls is added.

Drag coefficient correction The drag coefficient is corrected for the effect due to variation of the angle of attack, wake blockage, and horizontal buoyancy effect. Actually, by means of the walls, the model in the test section has too low aerodynamic drag, therefore the first term of the following Equation (3.18) is positive, because it must be added to the measurement of the wind tunnel balance. Conversely, the second and third terms are negative because the effects of the wake of the model and of the walls in a closed test section increase the aerodynamic drag with respect to free air conditions, therefore they must be subtracted from the measurement of the wind tunnel balance:

$$\Delta C_D = \Delta\alpha C_L - \Delta C_{D_{\mathrm{wb}}} - C_{D,B} \tag{3.18}$$

where the effect of wake blockage is estimated as[5]:

$$\Delta C_{D_{\mathrm{wb}}} = \epsilon_{\mathrm{sb}} C_{D_0} \tag{3.19}$$

while the *buoyancy* $C_{D,B}$ is a constant of the wind tunnel[6].

In conclusion, the corrected drag coefficient is therefore the sum of two terms. The first one is extracted from the measurements of the wind tunnel balance and corrected for blockage effects. The second one is referred to the correction previously discussed in Equation (3.18):

$$C_{D_{\mathrm{c}}} = C_D \frac{q}{q_{\mathrm{c}}} + \Delta C_D \tag{3.21}$$

Pitching moment coefficient correction This correction affects the pitching moment curve slope of the horizontal tailplane only. The curve slope is corrected by considering the wall effect and the streamline curvature effect[7]. This effect, discussed earlier as *tail downwash change* in Section 3.4, occurs in the presence of the horizontal tailplane. In this case, due to the effect of the walls, the tunnel model is more stable

[5] It should be underlined that the $\Delta C_{D_{\mathrm{wb}}}$ due to the wake is estimated with the solid blockage ϵ_{sb}.

[6] Ref. [18] gives a different and apparently incorrect indication, at least in the summary at the end of the wind tunnel corrections chapter. The correction of the drag coefficient is given by the sum — always positive — of:

$$\Delta C_D = \Delta\alpha_{\mathrm{up}} C_{L,\mathrm{w}} + \delta \frac{S}{C} C_{L,\mathrm{w}}^2 \tag{3.20}$$

where the second term seems to be the effect of the wake blockage. Furthermore, the effect of the horizontal buoyancy of the test section is neglected.

[7] Ref. [18] neglects the streamline curvature effect, after defining and evaluating it in the angle of attack corrections section. The correction of the pitching moment coefficient is reported as:

$$\Delta C_M = C_{M_{\alpha,\mathrm{t}}} \tau_{2,\mathrm{t}} \delta \frac{S}{C} C_{L,\mathrm{w}} \tag{3.22}$$

where the lift coefficient is that of the wing alone.

than in free air conditions. Therefore, the correction in Equation (3.23), must be subtracted from the value of the pitching moment coefficient measured by the tunnel balance:

$$\Delta C_M = C_{M_{\alpha,\mathrm{t}}} \tau_{2,\mathrm{t}} \delta \frac{S}{C} C_L + 0.25 \Delta C_L \tag{3.23}$$

where $\tau_{2,\mathrm{t}}$ is used to manage the amount of correction and is referred to the tailplane. It is derived as already discussed for the Equation (3.14). The $C_{M_{\alpha,\mathrm{t}}}$ value is the pitching moment curve slope of the horizontal tailplane, which should be estimated from preliminary wind tunnel tests or calculated as:

$$C_{M_{\alpha,\mathrm{t}}} = -C_{L_{\alpha,\mathrm{t}}} \eta_{\mathrm{t}} \overline{V}_{\mathrm{t}} \tag{3.24}$$

where the sign $(-)$ refers to the fact that the horizontal tailplane is behind the pitching moment reference point, therefore contributing to the nose-down behaviour. The volumetric ratio is defined in the usual way:

$$\overline{V}_{\mathrm{t}} = \frac{l_{\mathrm{h}} S_{\mathrm{h}}}{S \bar{c}} \tag{3.25}$$

Finally, the corrected moment coefficient is defined as:

$$C_{M_{\mathrm{c}}} = C_M \frac{q}{q_{\mathrm{c}}} - \Delta C_M \tag{3.26}$$

Additional corrections

Drag coefficient at zero lift – calculation The value ϵ_{wb} is estimated using the Equations (3.8) and (3.9), where the C_{D_0} must be known. If this is unknown, it may be computed using Equation (3.10) when $\alpha \approx 0°$. This requires the attention of the operator to carry out the first measurement at $\alpha \approx 0°$. At this point, for subsequent tests, this estimated C_{D_0} value should be inserted in the file containing the tunnel and model parameters.

The Oswald factor e can be evaluated, with good approximation, using the formula reported in Raymer [25]:

$$e = 1.78(1 - 0.045 \mathit{A}\!\mathit{R}^{0.68}) - 0.64 \tag{3.27}$$

valid for $3 \leq \mathit{A}\!\mathit{R} \leq 10$. However, it is ideal to always carry out a preliminary wing only (or wing-fuselage) test (with flaps retracted, if any) and then perform a linear regression on the uncorrected experimental data of C_L and C_D to find C_{D_0} and e.

Wing lift curve slope – calculation The wing lift curve slope $C_{L_{\alpha,\mathrm{w}}}$ may be found using Roskam's formula [26] for swept a wing — Equation (3.28) — with the

simplification of Mach number equal to zero:

$$C_{L_{\alpha,\mathrm{w}}} = \frac{2\pi \mathit{Æ}}{2 + \sqrt{\frac{\mathit{Æ}^2}{(C_{l_\alpha}/2\pi)^2}\left(1 + \tan \Lambda_{c/2}^2\right) + 4}} \quad (\mathrm{rad}^{-1}) \tag{3.28}$$

All the necessary data for this calculation are already present in the file containing the tunnel and model parameters. The mean airfoil lift curve slope C_{l_α} can be approximated to 0.105 deg^{-1}. Consequently, the constant $(C_{l_\alpha}/2\pi)^2$ can be approximated to 0.9169.

4

Longitudinal Wind Tunnel Tests

Contents

4.1 Aircraft model and test section setup

This chapter covers the experimental investigation of the aerodynamic characteristics of the model tested in the wind tunnel. The main purpose of these experimental tests has been focused on the estimation of the longitudinal static stability characteristics of the test model.

The ratio between the scale model wing span and the test section width is 0.75,

while the ratio between the test section height and width is 0.7. This means that scaled model dimensions are within the range of wind tunnel walls correction effectiveness, as suggested by Barlow et al. [18]. The aircraft model consists of several disjointed components such as wing, fuselage, horizontal and vertical tailplanes and battery cover, to allow testing of different configurations. The model is also equipped with several movable surfaces, including control surfaces (elevator and rudder) and flaps. The wing has been constructed from two aluminum alloy blocks and joining them in the wing-fuselage fillet subpart — the karman. The mass of such group is approximately 15 kg. The flaps have been attached using brackets, and the deflection angles can be changed by using different bracket shapes. The fuselage has been built into two parts: an upper block and a lower block to facilitate the removal of the internal material and reduce its weight, which is approximately 8 kg. Subsequently, the two blocks have been joined together using screws. All the components have been made of aluminum alloy using a CNC machine from a third-part company, while the cover battery has been constructed using 3D printing. The main geometrical characteristics of the aircraft model are summarized in the Table 4.1, and the three-view is shown in Figure 4.1. More details are reported in Appendix A.

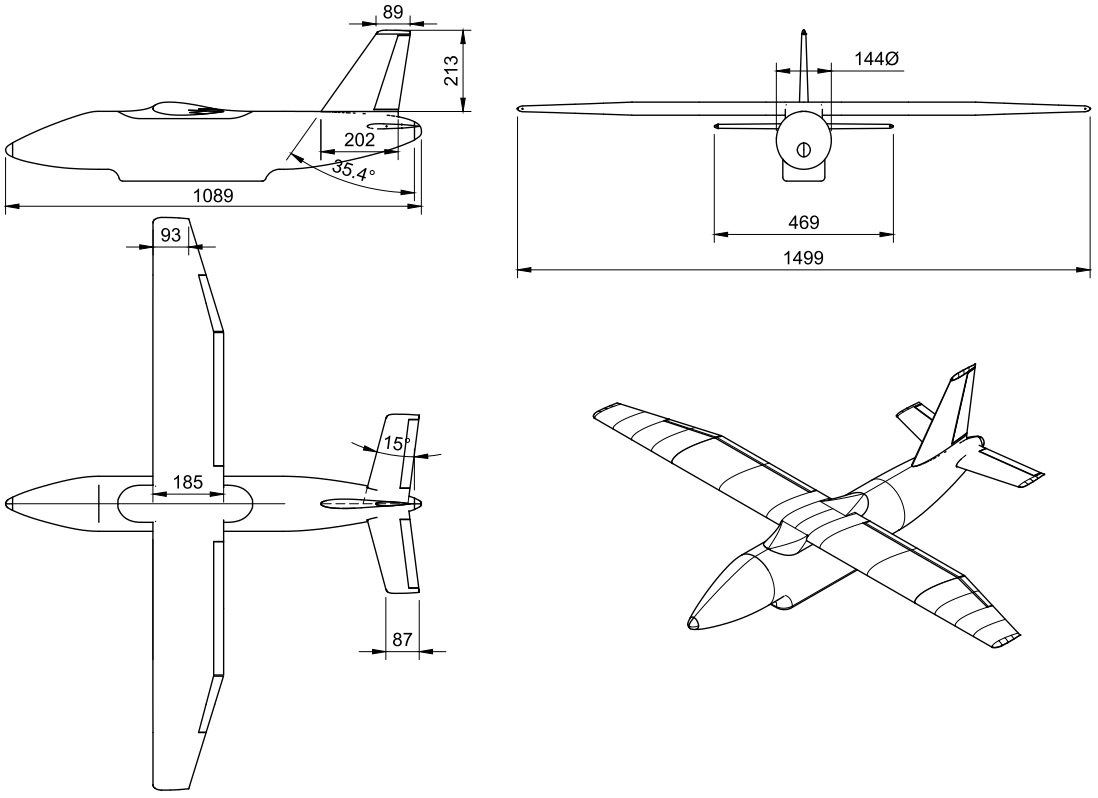

Figure 4.1 Aircraft model three-view.

Table 4.1 Aircraft model, main characteristics.

Wing	
S_{w}	0.25 m^2
b_{w}	1.5 m
c_{root}	0.185 m
c_{kink}	0.185 m
c_{tip}	0.093 m
c_{mac}	0.171 m
x_{ac}	0.429 m
y_{ac}	0.320 m
z_{ac}	0.107 m
Λ_{w}	0 deg
Horizontal tail	
S_{h}	0.0489 m^2
b_{h}	0.466 m
c_{root}	0.123 m
c_{tip}	0.087 m
c_{mac}	0.106 m
l_{h}	0.560 m
Λ_{h}	15 deg
Vertical tail	
S_{v}	0.0310 m^2
b_{v}	0.213 m
c_{root}	0.202 m
c_{tip}	0.089 m
c_{mac}	0.153 m
l_{v}	0.482 m
Λ_{v}	35.4 deg
Fuselage	
l_{f}	1.089 m
d_{f}	0.144 m

Before installing the aircraft model, a check of the forces measured by the balance and acquired by the virtual instrument had been carried out using known masses. This procedure has required attaching a bar above the balance plate. Subsequently, a mass of 5 kg has been first placed on the bar in correspondence of the balance centre — the point where the pitching moment readings are zero — and the correct reading of the normal force F_z has been observed in the data acquisition software. Similarly, the mass of 5 kg has also been placed approximately 20 cm behind the balance centre, as shown in Figure 4.2, and the expected result from the acquisition program has been a pitching-up moment M_y — positive moment — of 1 kgf $\cdot$ m.

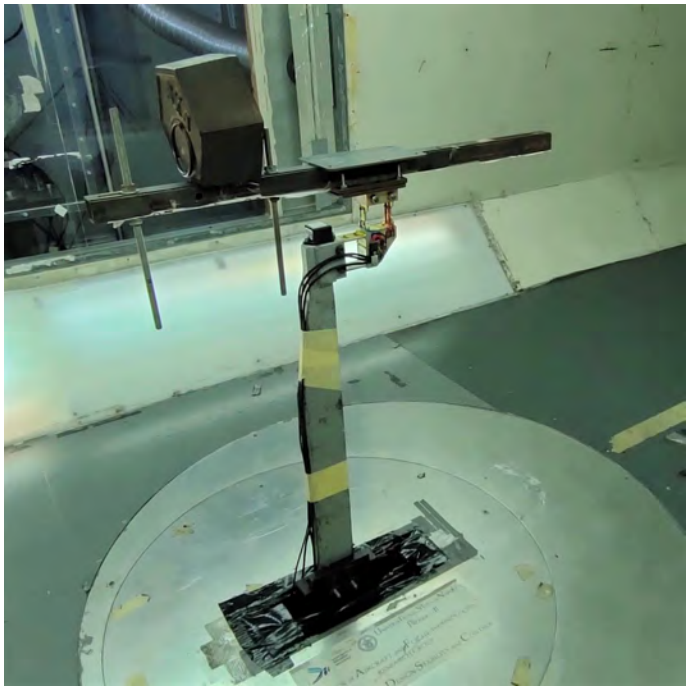

Figure 4.2 Checking the pitching moment with a 5 kg weight placed 20 cm behind the balance centre.

Drag measurements have been verified using a bar and pulley system together, as shown in Figure 4.3. A cable has been fixed at a height approximately equal to that of the balance center above the gallery floor. A first mass of 200 g has been hung on the cable to keep it tight. The input signals to the acquisition software have been reset. A second 200 g mass has been hung on the cable, and it has been verified that the acquisition software read 0.200 kgf as the axial force F_x.

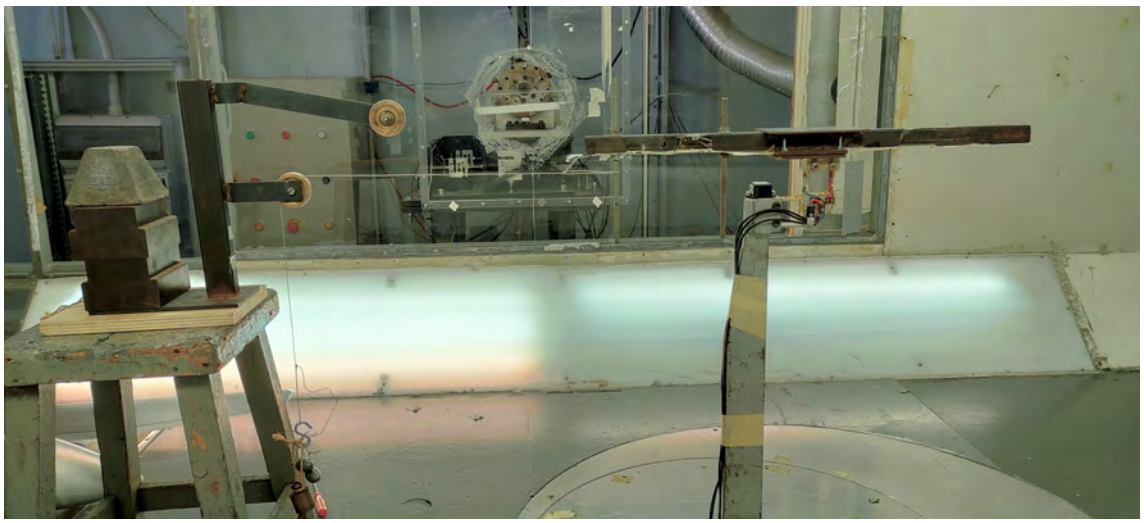

Figure 4.3 Checking drag measurements with a weight hanging from a cable that rotates around the pulley.

4.2 Wing-body installation

The process of setting up the test model begins with placing the fuselage at the base of the sting. The level located on the top of the balance is used to check the inclination angle of the balance plate in both the x and y directions, as shown in Figure 4.4. The fuselage is equipped with a special compartment designed to allow the passage of the internal strain gage balance.

Figure 4.4 Fuselage model at the base of the sting and the level on the balance plate.

The wing is attached to the balance plate via an interface plate, as shown in Figure 4.5. In detail, the interface plate is first mounted on the balance plate using four bolts, as shown in Figure 4.6. The wing is then placed above this interface plate and secured with four screws, as shown in Figure 4.7.

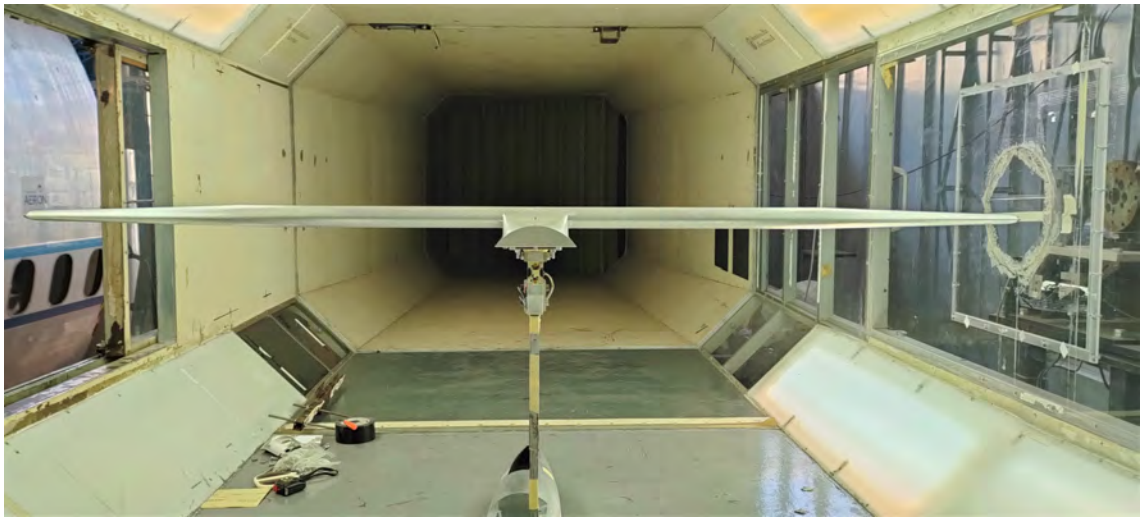

Figure 4.5 Wing installed on the balance plate.

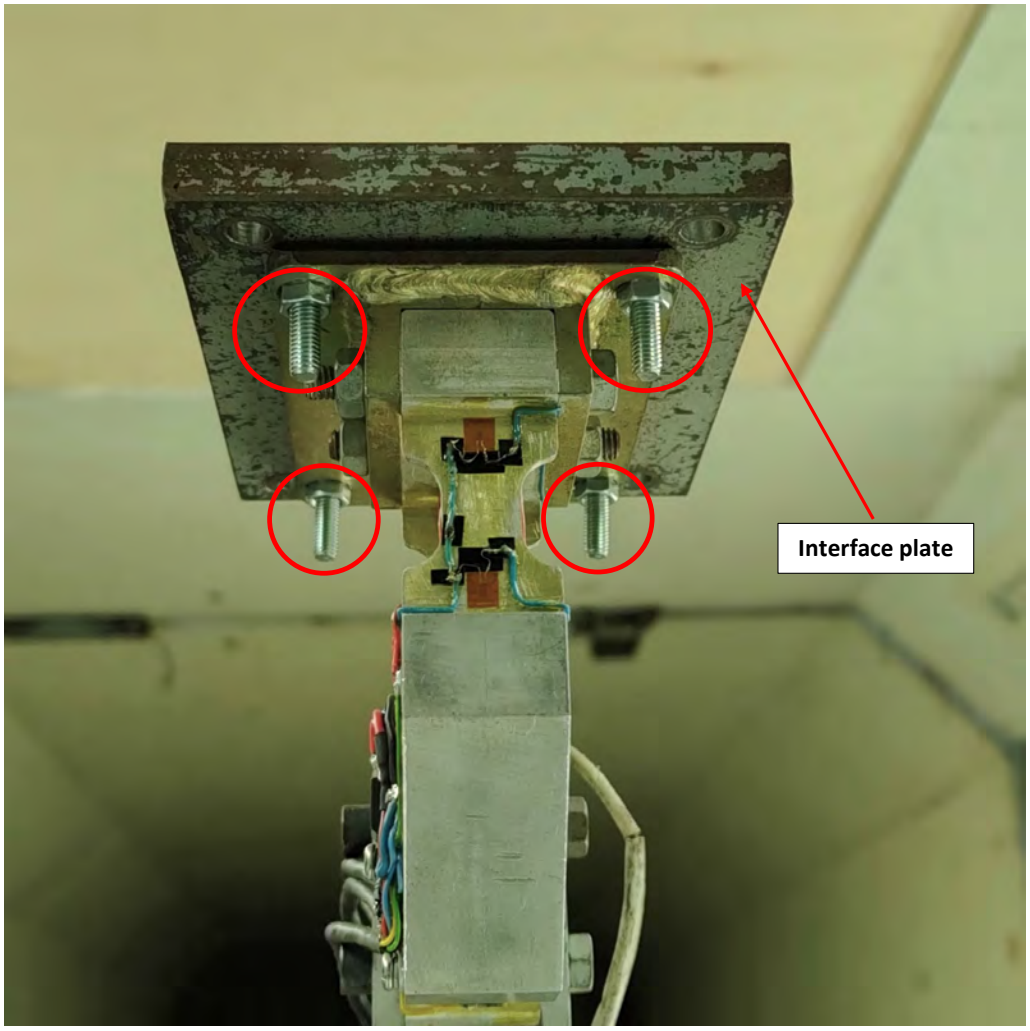

Figure 4.6 Attaching the interface plate to the balance plate using four bolts.

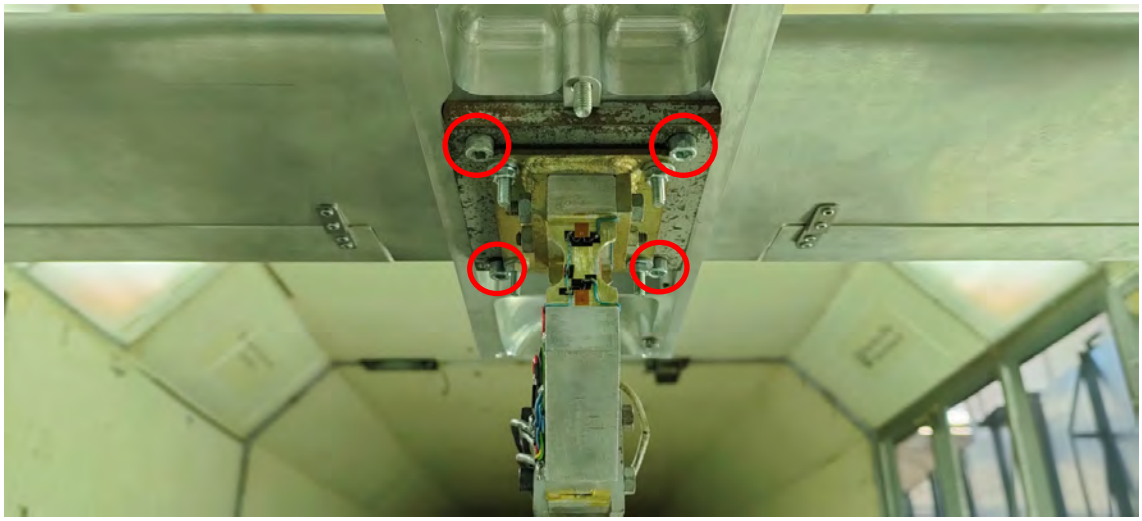

Figure 4.7 Attaching the wing to the interface plate using four screws.

The next step is to lift the fuselage up to match the wing and secure it with screws, as shown in Figure 4.8. In this way the wing-body (WB) configuration is obtained and is fixed to a special sting that positions the model about halfway into the test section. Figure 4.9 and Figure 4.10 show this configuration of the aircraft model in the test section. All the gaps on the fuselage have been sealed using duct tape and paper tape. It is worth noting that the balance's plate is the only contact interface between the balance itself and the model.

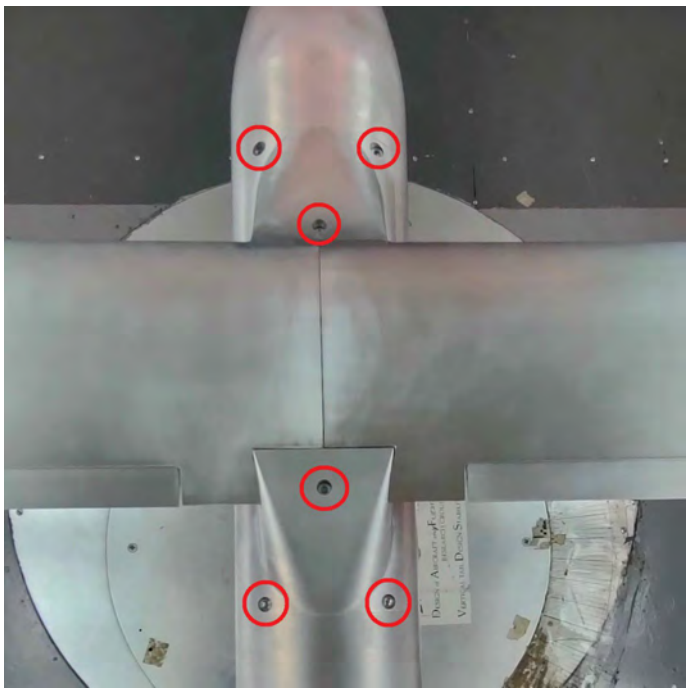

Figure 4.8 Fixing between wing and fuselage with six screws.

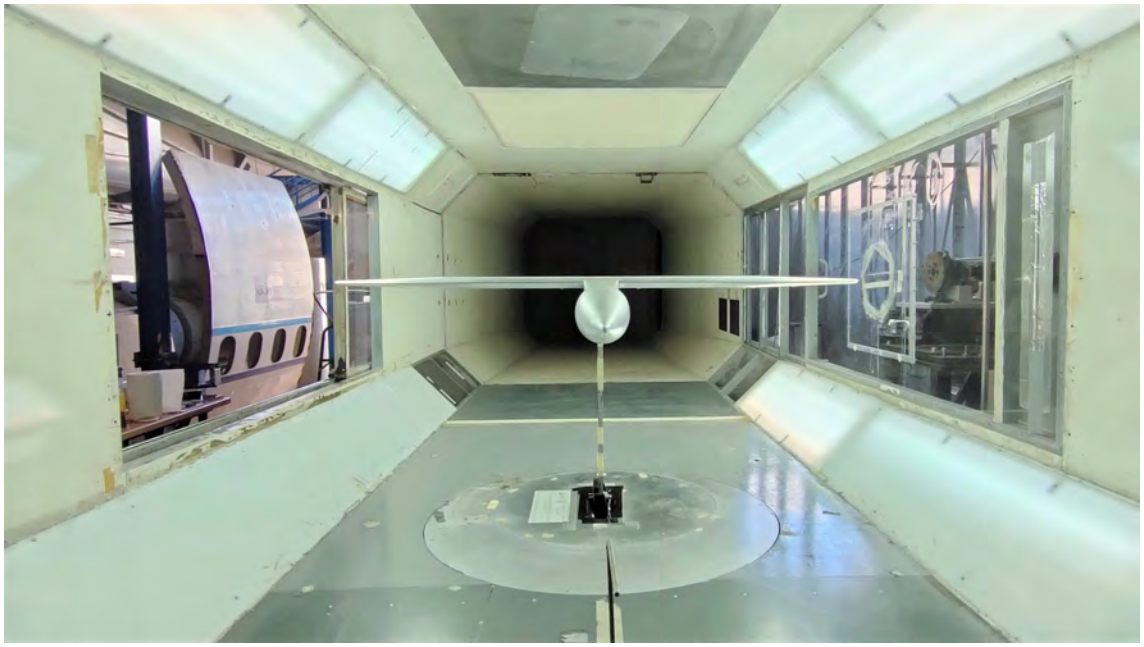

Figure 4.9 Frontal view of the wing-body configuration in the wind tunnel.

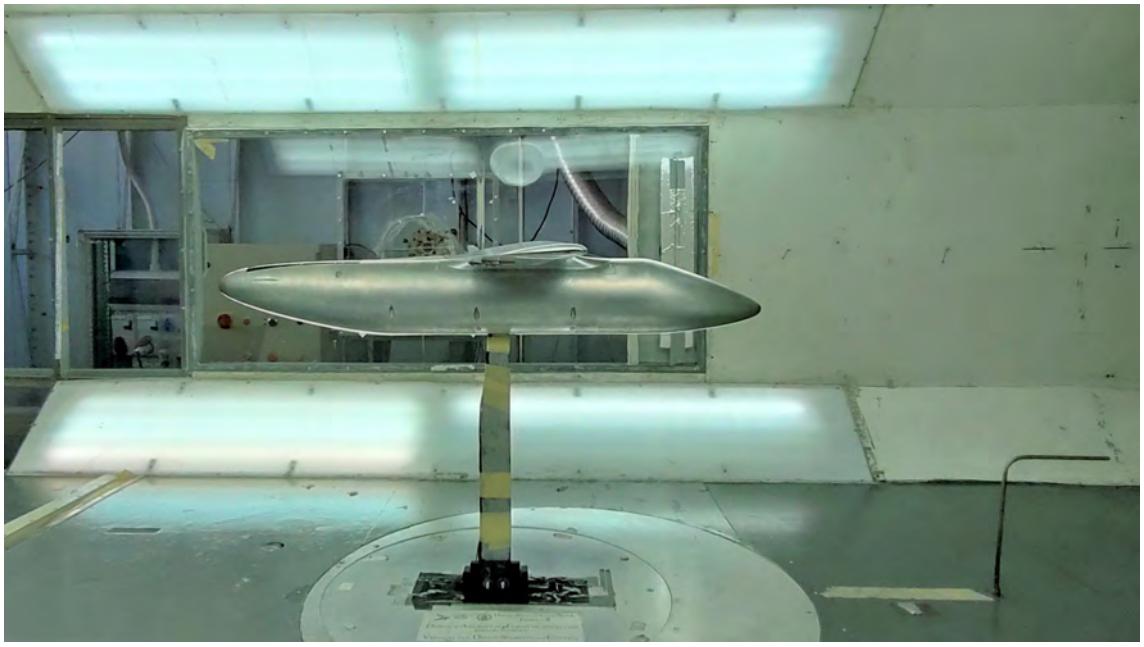

Figure 4.10 Lateral view of the wing-body configuration in the wind tunnel.

4.3 Wing-body configuration tests

The typical experimental test is structured as follow:

1. **Calibration**: since the goal of the experiment is to measure the aerodynamic forces and moments, a calibration procedure is needed in order to have the net aerodynamic forces acting on the model. Because the centre of gravity of a certain configuration does not correspond to the balance center, the mass distribution of a configuration will affect the measurements of lift, drag and pitching moment. Thus in order to estimate the net aerodynamic forces/moments for each tested configuration, the weight contributions to each measured quantity must be determined before the experimental test is performed, in the tunnel off condition. The calibration procedure is stepped as follow:

   - the model is placed at zero incidence angle, with a tolerance of $\pm$ 0.05°;
   - balance measurements are reset;
   - the model is placed at the minimum angle of incidence, which is approximately $-2°$ in this case;
   - balance measurements are acquired at each model attitude — using a 2° step for the calibration procedure in this case — until the maximum available pitch angle, in this case approximately 10°;
   - the acquired data are used to extract interpolation laws. In this way the estimation of the contribution to each measured force/moment introduced by the weight of the tested model can be subtracted to obtain the net force/moment measurements.

2. **Data acquisition**: immediately after the forces and moments have been reset, the tunnel is turned on and brought to the operative conditions. The operator acquires the data at each attitude after a waiting time of about 3 seconds to guarantee a stationary conditions of the flow. The acquisition program samples data at 1000 Hz, displaying the mean value of the last 1000 acquired data on the screen and updating them every second. For the longitudinal tests, data have been acquired starting from the zero incidence angle, then the model has been pitched down till $-2°$, with a step of 1°. Once the minimum pitch attitude has been reached, the model has been driven again at the zero incidence angle, acquiring again the set of data for this condition. Then the model has been driven to the maximum pitch attitude allowed, defined as the attitude at which no vibrations that could damage the balance occur, with a step of 1° or less when close to the stall.

3. **Data elaboration and storage**: the aerodynamic force and moment coefficients are calculated by the acquired measurements of forces and dynamic pressures. Two different corrections, already discussed in the previous chapter, have been applied to these coefficients:

- Moments transfer
- Wind tunnel corrections

A point located at 25% of the wing mean aerodynamic chord along the longitudinal axis and 20% of the wing mean aerodynamic chord below the wing mean aerodynamic chord plane, has been chosen as the reference point — pole — for the calculation of the aerodynamic forces and moments. Figure 4.11 illustrates the location of the pole, balance center, and wing aerodynamic center. The position of the pole can be defined relative to the balance center. Since the center of balance does not coincide with the chosen reference point, the aerodynamic moments must be transferred to the desired reference point. Since the balance is integrated with the model, the transfer of the pitching moment from the balance center to the chosen reference point can be expressed as shown in Equation (3.5), which is re-proposed here:

$$M_{y_{\text{trasp}}} = m_{y_{\text{tar}}} + F_{z_{\text{tar}}} \cdot x + F_{x_{\text{tar}}} \cdot z \tag{3.5}$$

where $M_{y_{\text{trasp}}}$ is the moment along the y axis, passing through the pole and positive if oriented towards the right wing. $m_{y_{\text{tar}}}$, $F_{z_{\text{tar}}}$, $F_{x_{\text{tar}}}$ are the net aerodynamic forces and moment measured at the balance center. The subscripts x, y, and z indicate that the forces or moment are in the direction (or respect to) the longitudinal, lateral and vertical axes, respectively. The quantities x and z are the longitudinal and vertical distances of the chosen reference point from the balance centre, respectively. Table 4.2 shows the coordinates of the chosen reference point.

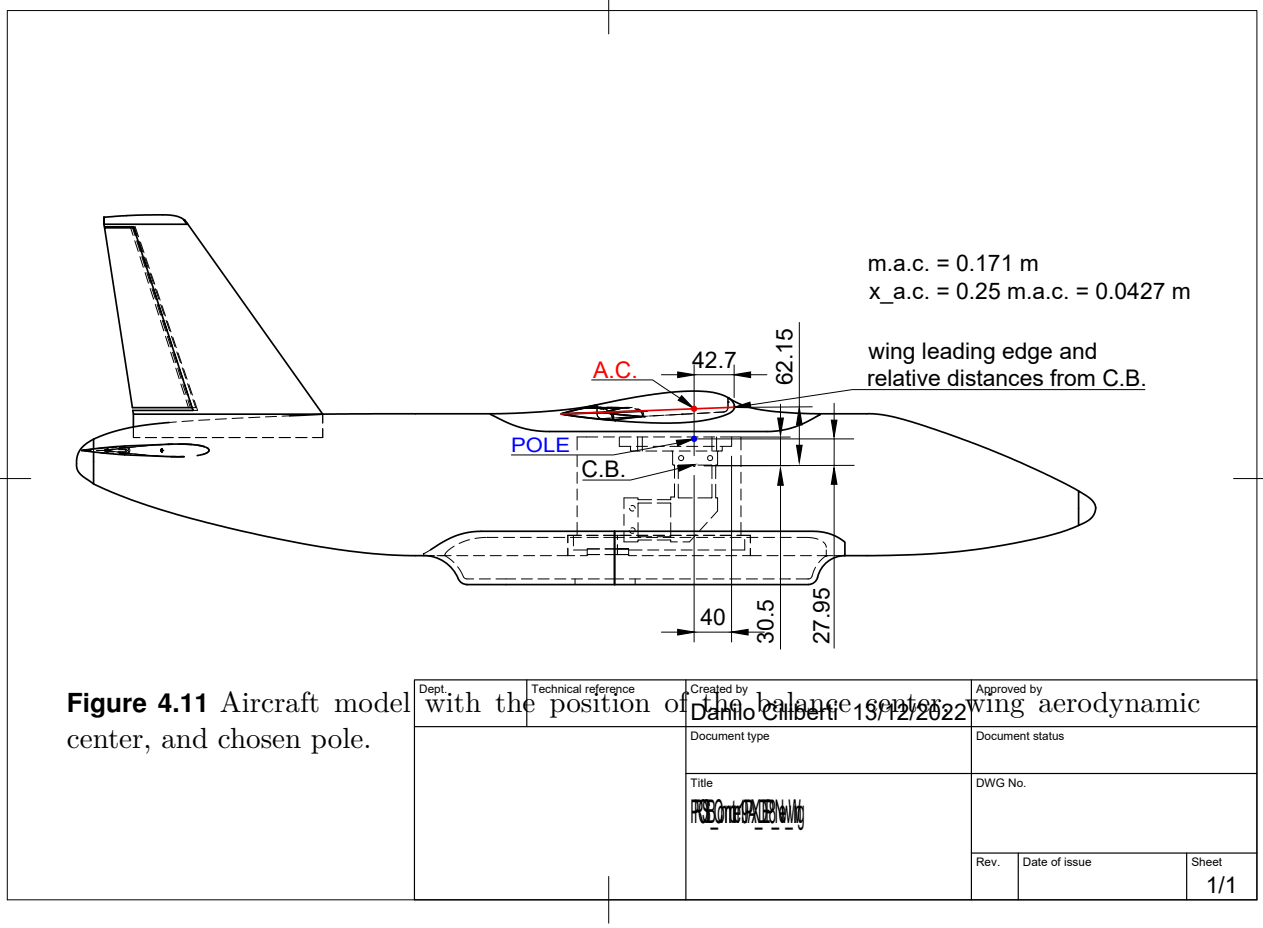

Figure 4.11 Aircraft model with the position of the balance center, wing aerodynamic center, and chosen pole.

Table 4.2 Force and moments reference point location with respect to the balance centre.

Ref. point coordinate	Value
x_{pole}	0.000 m
y_{pole}	0.000 m
z_{pole}	0.028 m

Data for the required wind tunnel corrections, calculated as discussed in Section 3.4, are reported in Table 4.3.

Table 4.3 Aircraft model, volumes and solid blockages for the WB configuration.

Buoyancy Drag Coefficient	-0.0005
Volumes	
Wing	0.0052 m^3
Fuselage	0.014 m^3
Horizontal tail	0.00039 m^3
Vertical tail	0.00046 m^3
Cover battery	0.0029 m^3
Solid blockages	
Wing	0.00107
Fuselage	0.00264
Horizontal tail	0.000078
Vertical tail	0.000092
Cover battery	0.00059
$dC_{M_{\text{tail}}}/d\alpha$	-0.0353 deg^{-1}

4.3.1 Corrected and uncorrected aerodynamic coefficients

The effects of the corrections discussed above are shown in the following figures, which compare the corrected and uncorrected experimental results for the wing-body configuration at $Re = 430000$ are reported. The corrected and uncorrected lift, drag and moment coefficients are shown in Figures 4.12, 4.13, and 4.14, respectively.

As shown in Figure 4.12, the trend of the corrected and uncorrected lift coefficient exhibit a similar trend. This trend, characterized by a bend in the lift curve slope, is a common feature that is experienced with laminar bubble formation when flow transition is left free. However, the corrected values are shifted by a positive amount $\Delta\alpha$, while the C_L values are approximately the same.

Similarly, in the drag polar curve shown in Figure 4.13, the corrected values are shifted by an amount ΔC_D compared to the uncorrected ones, while the C_L values are approximately the same. Thus the corrected drag coefficient values will be higher than the uncorrected values, because the value of drag coefficient measured in the wind tunnel, due to the walls presence, is lower than the drag coefficient experienced in actual flight.

Turning to the pitching moment coefficient curve in Figure 4.14, it can be seen that for $\alpha < 5°$, the slope is positive, which is typical of an unstable wing-body configuration. However, around $\alpha = 7°$ as the lift slope changes, the slope of the curve reverses, then becomes quite flat. This behavior can be attributed to the presence of a laminar bubble forming on the wing. In conclusion, the corrected values are shifted by an amount $\Delta\alpha$ forward compared to the uncorrected ones, while the C_M values are approximately the same.

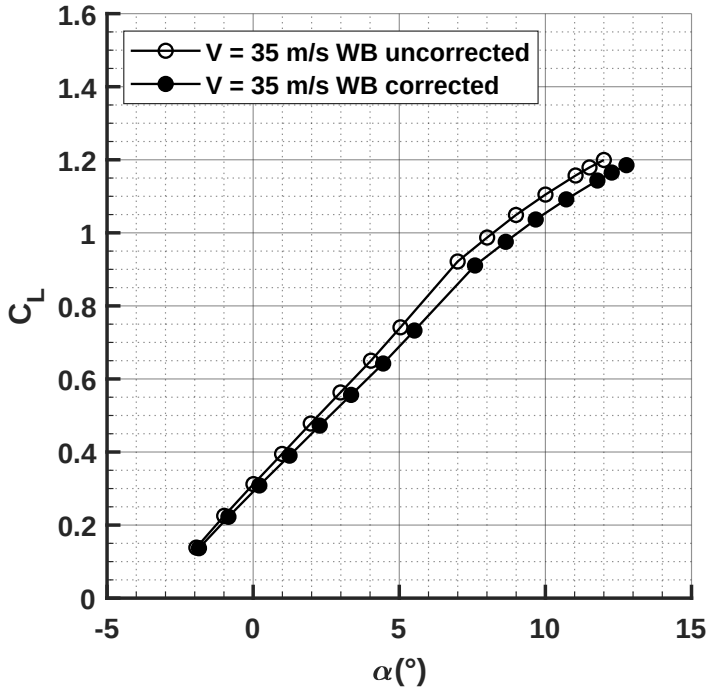

Figure 4.12 Effects of the wind tunnel corrections on the lift coefficient with $Re = 430000$, free transition.

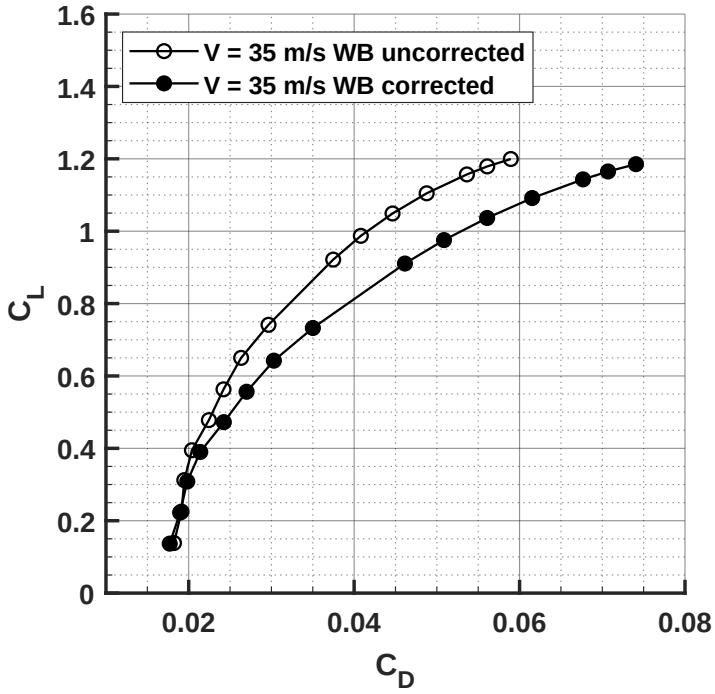

Figure 4.13 Effects of the wind tunnel corrections on the polar curve with $Re = 430000$, free transition.

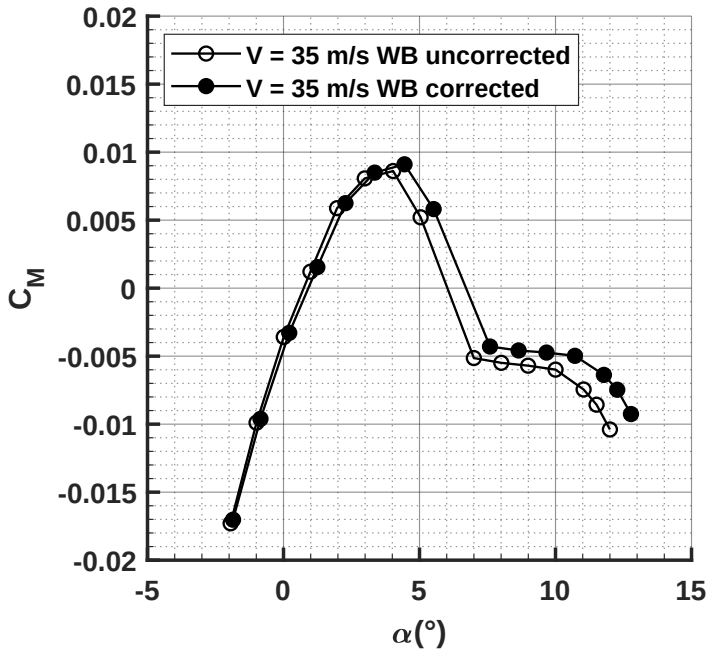

Figure 4.14 Effects of the wind tunnel corrections on the pitching moment coefficient with $Re = 430000$, free transition.

4.3.2 Effect of Reynolds number on the aerodynamic coefficients

The effects of Reynolds number on the corrected aerodynamic coefficients are examined by comparing experimental tests executed at $V_\infty = 25$ m/s and $V_\infty = 35$ m/s, corresponding to $Re = 310000$ and $Re = 430000$, respectively. As shown in Figure 4.15, the effect of the Reynolds number on the lift coefficient is almost imperceptible, with the two curves appearing to be nearly superimposed.

However, the effect of the change in Reynolds number is not negligible on the drag coefficient, as shown in the drag polar curve of Figure 4.16. The values acquired at the lower Reynolds number are larger by an almost constant value ΔC_D for a given C_L. In other words, by increasing the speed of the wind tunnel, an increment of the Reynolds number allowed for a reduction in the drag coefficient while maintaining approximately the same lift coefficient, as expected.

The effect of Reynolds number is also visible on the pitching moment coefficient curves shown in Figure 4.17. The C_M values acquired at lower Reynolds number are shifted upward by an almost constant amount ΔC_M, while the α values are approximately the same. This suggests that, at the same angle of attack, increasing the Reynolds number leads to a reduction of the pitching moment coefficient magnitude.

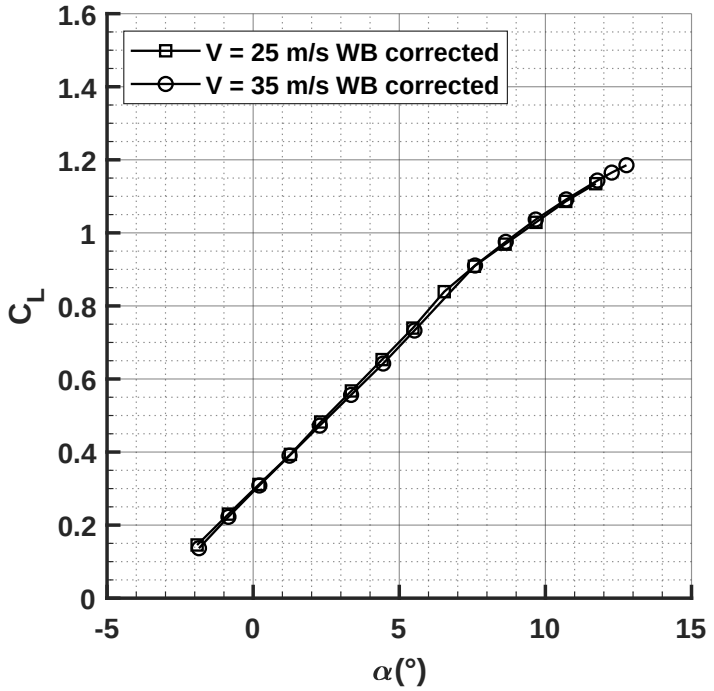

Figure 4.15 Effects of the wind tunnel speed on the lift coefficient with $Re = 310000$ at $V_\infty = 25$ m/s and $Re = 430000$ at $V_\infty = 35$ m/s. The lift slope is $C_{L_\alpha} = 0.08$ deg^{-1}.

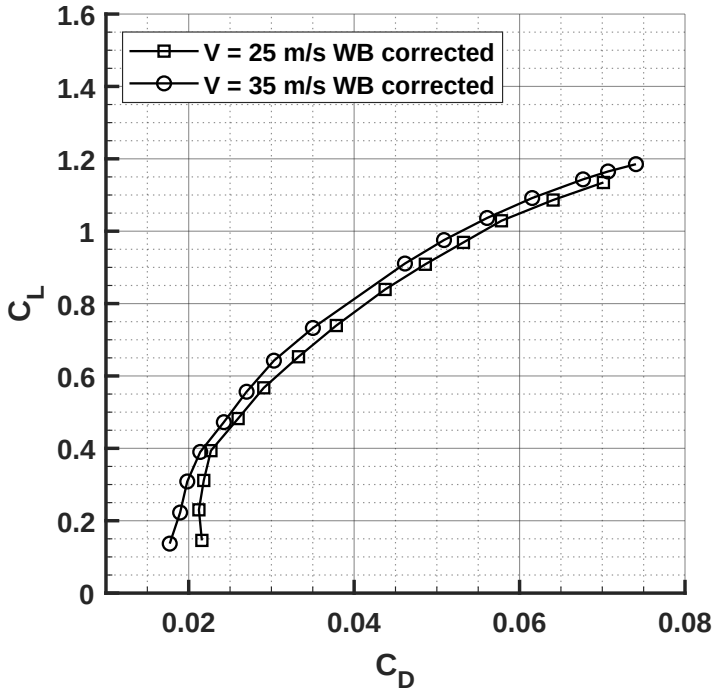

Figure 4.16 Effects of the wind tunnel speed on the polar curve with $Re = 310000$ at $V_\infty = 25$ m/s and $Re = 430000$ at $V_\infty = 35$ m/s.

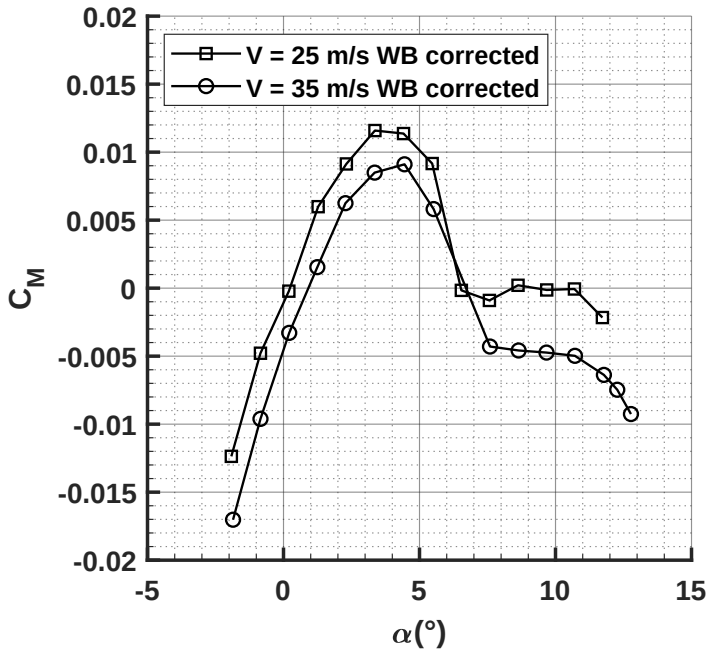

Figure 4.17 Effects of the wind tunnel speed on the pitching moment coefficient with $Re = 310000$ at $V_\infty = 25$ m/s and $Re = 430000$ at $V_\infty = 35$ m/s.

4.3.3 Trip strips

The longitudinal tests of the wing-body configuration have been conducted at a wind speed of approximately 35 m/s — the maximum available wind speed is about 50 m/s — with a Reynolds number of approximately 0.43 million and defined as:

$$Re = \frac{\rho_\infty V_\infty \overline{c}}{\mu_\infty} \tag{4.1}$$

where ρ_∞ is the air density, V_∞ is the air speed, $\overline{c}$ is the wing mean aerodynamic chord, which is the reference length, and μ_∞ is the dynamic viscosity of the air. It is well known that the Reynolds number can have a significant effect on various quantities of interest, such as forces and stability moments, etc. Obviously, it is important for wind tunnel tests to provide conditions that are as similar as possible to actual flight conditions. Therefore the Reynolds number achieved in the tunnel must be as close as possible to that of the full-scale aircraft in flight. It is clear that full Reynolds numbers, which can reach into the tens of millions, are not easily achievable in a typical wind tunnel due to power constraints (see Table 3.1). In order to achieve higher Reynolds numbers, some wind tunnels may decrease the air temperature to reduce its viscosity and increase the total pressure to raise the air density, as described in Section 2.3.2. Since the Reynolds number in low-speed wind tunnels cannot match that of flight conditions, other artifices are needed to replicate the boundary layer of the full-scale aircraft, otherwise laminar separations will affect the measurements. A simple and effective way to address this issue is to use trip strips.

A trip strip is an artificial roughness added to the model in order to fix the location of the transition from laminar to turbulent boundary layer on the wing, which helps to avoid aerodynamic phenomena related to low Reynolds number effects, such as laminar separation bubbles. The thickness and the right position of the trip strips have been determined through flow visualization tests using fluorescent oil. The visualization of the laminar separation bubbles for $\alpha = 5°$ and $\alpha = 8°$ are shown in Figure 4.18 and 4.19, respectively. For major clarity of the pictures, coloured oil has been used without the ultra-violet lamp and the behaviour of the bubble can be seen as the angle of attack increases. As shown in Figure 4.19, as the angle of attack increases, the bubble moves towards the leading edge and reduces in size relative to the wing chord length. After conducting these initial tests using oil, a position has been assumed to place the trip strips. This position has been hypothesized to be advanced with respect to the starting point of the bubbles at $\alpha = 5°$ and $\alpha = 8°$, in order to cover also the cases at higher α angles, for which the bubble moves towards the leading edge. Furthermore this assumed position is highlighted by the black mark on the tape in Figure 4.20. Additional visualization has been carried out using strips made of adhesive tape with triangular edges and with different number of layers. These strips have been glued in the previously assumed position, to observe the effect of the thickness on the laminar bubble and to verify whether

the chosen position of the strips could eliminate the bubble formation. Figure 4.20 shows the behaviour of the oil, and therefore the presence or absence of the laminar bubble, when a single layer strip, no strip and a strip with two superimposed layers are glued on the wing. From this test, as can also be seen from Figure 4.20, a single layer strip is sufficient to cause the boundary layer transition at the desired location and thus avoid the bubble formation. As a result, trip strips have been placed at about 5% of local chord on both the lower and upper surfaces of the wing, and at 20% of the nose length on the fuselage.

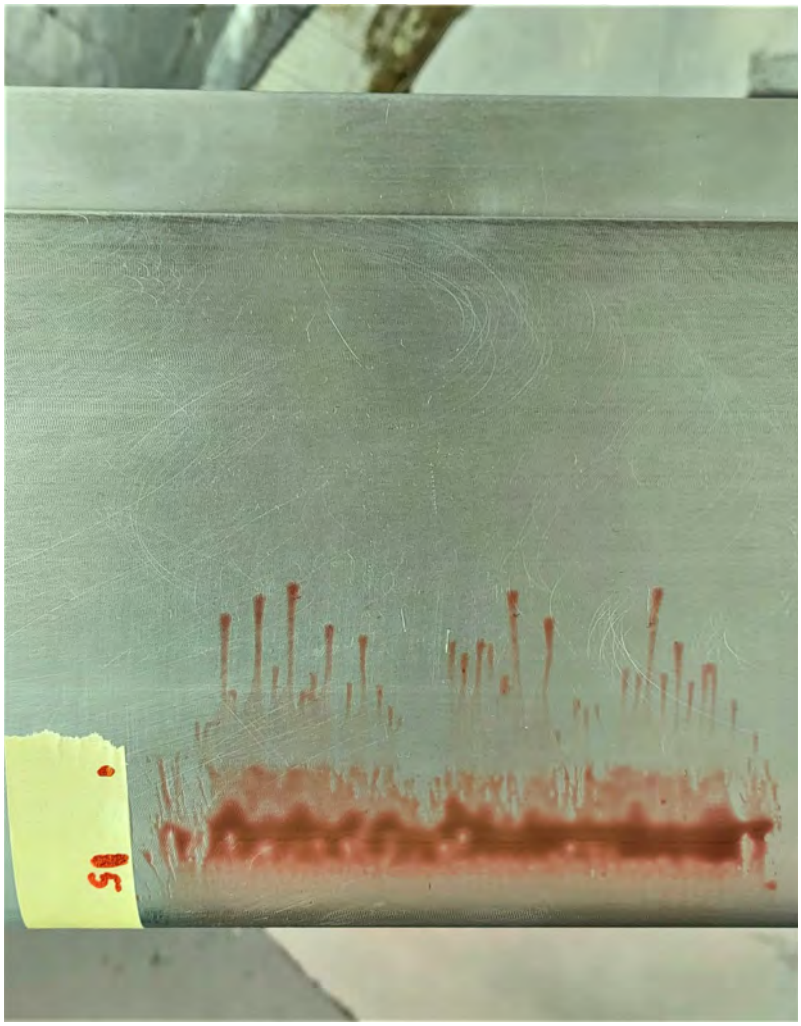

Figure 4.18 Laminar bubble visualization test at $\alpha = 5°$ with the position of laminar separation bubbles indicated on the tape, with $Re = 430000$.

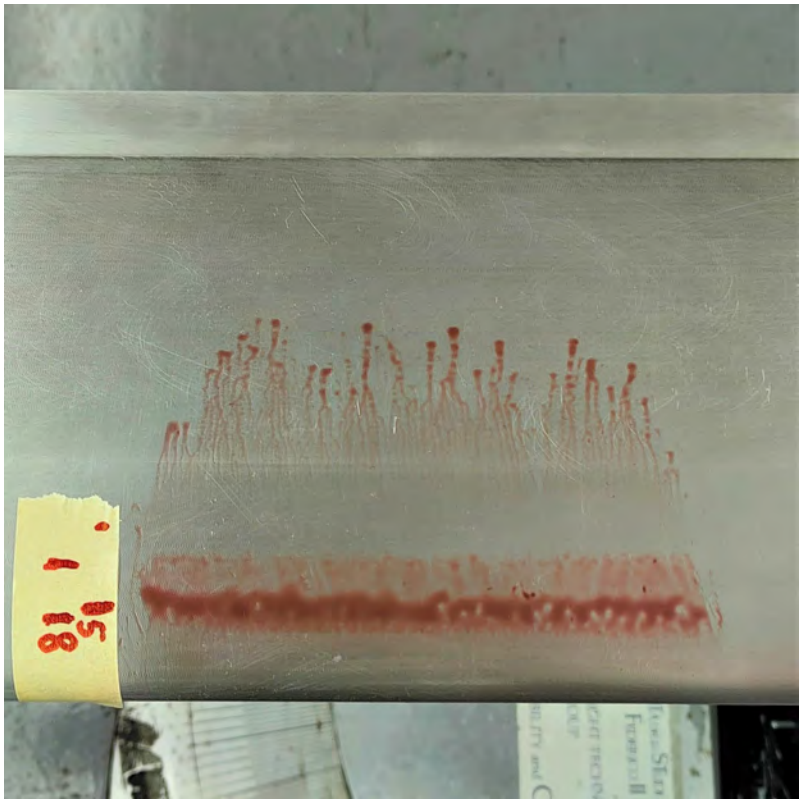

Figure 4.19 Laminar bubble visualization test at $\alpha = 8°$ with the positions of laminar separation bubbles at $\alpha = 5°$ and $\alpha = 8°$ indicated on the tape, with $Re = 430000$.

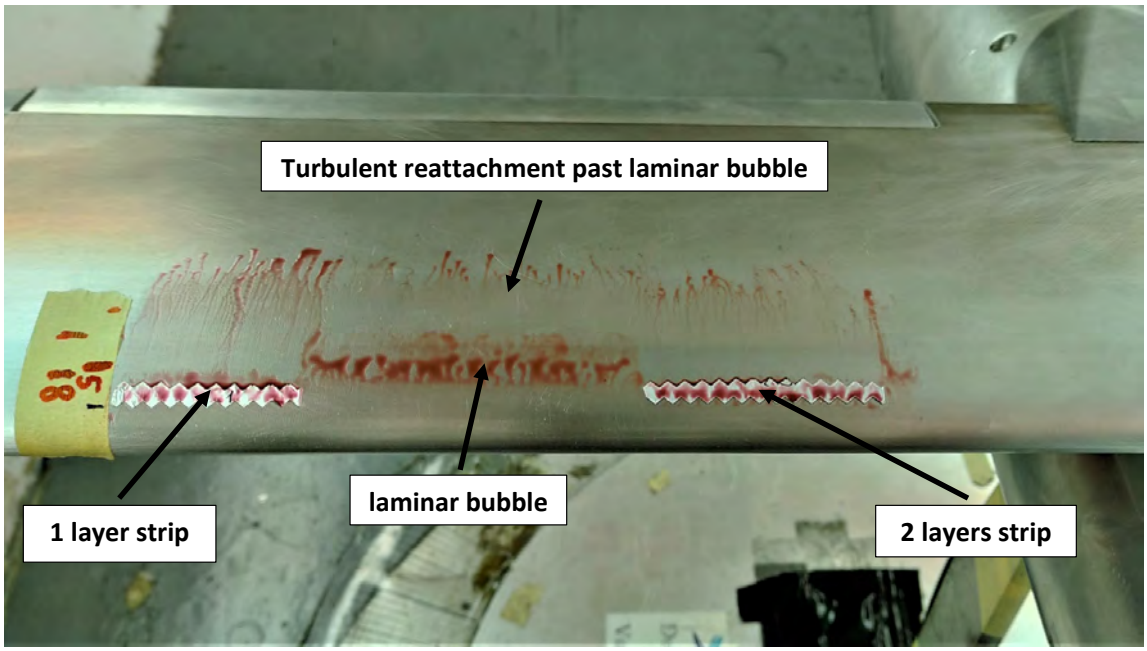

Figure 4.20 Effect of the trip strip thickness on the formation of a laminar separation bubble, with $Re = 430000$.

The following figures shown the comparison of the aerodynamic coefficient of the wing-body configuration at $Re = 430000$, with and without the trip strips. In Figure 4.21, the effect of the trip strips on the lift coefficient is depicted. It can be observed that, without the trip strips, the lift developed at a high angle of attack is larger than that with strip. This increase in lift curve slope can be explained by the formation of laminar bubble, which increases with the angle of attack, creating a region of additional suction due to the laminar separation, flow circulation, and re-attachment near the leading edge of the upper surface of the wing. This effect is eliminated by introducing the trip strips, resulting in a more linear trend of the lift coefficient curve.

The drag polar curve in Figure 4.22 is also affected by the trip strips. The presence of the strips introduces a difference in the drag coefficient ΔC_D for the same C_L. In other words, the trip strips increase the drag coefficient compared to the configuration without trip strips, as the trip strips represent a step on the wing surface. However, this increase in drag is the "price to pay" in order to avoid the formation of laminar bubbles on the aircraft low-Reynolds model.

Additionally, the trip strips also change the shape of the pitching moment curve, as shown in Figure 4.23. The pitching moment coefficient is therefore affected by the formation of the laminar bubble. With trip strips, for the same value of the angle of attack α, the pitching moment coefficient curve shifts upwards and changes shape, especially at high α angles.

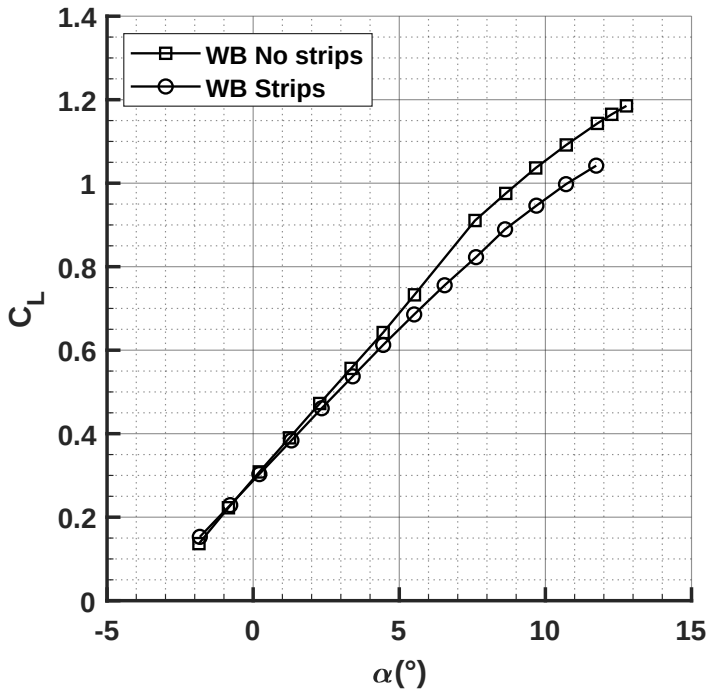

Figure 4.21 Effects of the trip strip on the lift coefficient with $Re = 430000$. The lift slope is approximately $C_{L_\alpha} = 0.08$ deg^{-1} (No strips) and $C_{L_\alpha} = 0.073$ deg^{-1} (Strips).

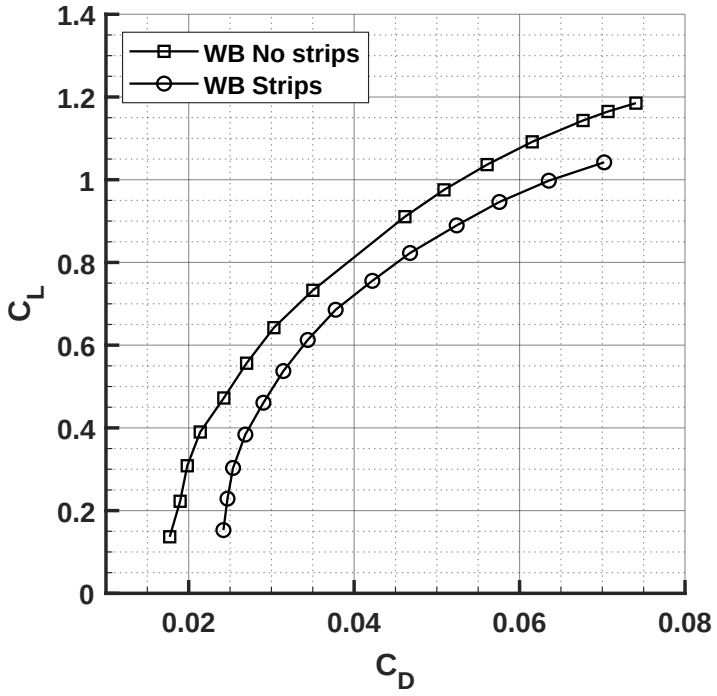

Figure 4.22 Effects of the trip strip on the polar curve with $Re = 430000$.

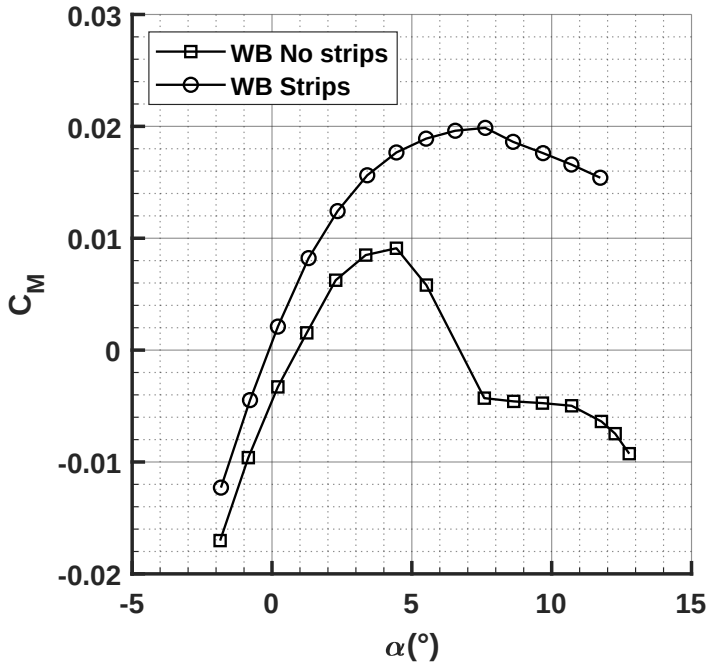

Figure 4.23 Effects of the trip strip on the pitching moment coefficient with $Re = 430000$.

4.3.4 Effect of flap deflected at different angles

These following tests have been conducted to observe the effect of the flap deflection on the wing-body configuration. The fowler flaps mounted have been a type of high-lift device used on the wing of the aircraft model. It has been divided into four parts, two internal and two external sections. Two different deflection angles have been analyzed: 15° for the take-off configuration, in which more lift is required but at same time less drag; 30° for the landing configuration, in which is required lift but also more drag. The wing-body configuration with flap deflection at 15° and 30° are shown in Figure 4.24 and 4.25 respectively.

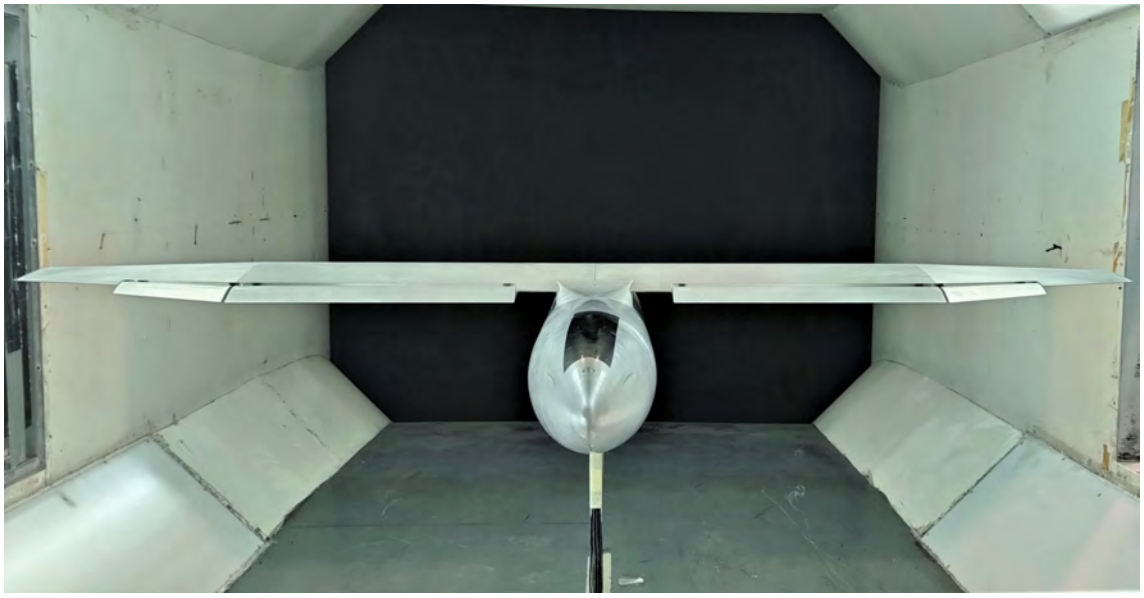

Figure 4.24 Wing-body configuration with flap deflection of 15° for the take-off phase.

Figure 4.25 Wing-body configuration with flap deflection of 30° for the landing phase.

The flaps have been mounted at different angles using supports. These supports have been made with CNC machines from aluminum. They have had different shapes to allow the flaps to be deflected at angles of 15° and 30°. In Figure 4.26 the shapes of these supports are illustrated for the configuration with flap at 0°, at 15°, and at 30°.

(a) *Flap* 0°.

(b) *Flap* 15°.

(c) *Flap* 30°.

Figure 4.26 Different supports used to install the flap on the wing, at different deflection angles.

The effect of the fowler flaps, obtained through wind tunnel tests, has been analyzed. In Figure 4.27, the effect of the fowler flaps on the lift coefficient is visible. As the devices are extended and then rotated, both the wing area and the curvature of the wing increase. Thus, extending the wing surface increases the lift slope with respect to the clean configuration. Meanwhile, rotating the flaps to increase the camber, the lift coefficient is increased. As expected, the fowler flaps at 15° and 30° leads to an approximately lift coefficient increment of $\Delta C_L = 0.4$

and 0.8, respectively, compared to the clean configuration at zero angle of attack. Additionally, these high-lift devices increases the lift slope with a minimal change in stall angle. It should also be noted that the maximum lift coefficient achieved with 30° of flap deflection, typical angle for landing configuration, is $C_{L_{\max}} = 2.2$. Then, after the maximum, an abrupt stall is occurred. Visible oscillations of the model have been observed during the tests in stall conditions with 30° of flap deflection.

As shown in Figure 4.28, the drag polar curve illustrates the impact of the high-lift devices, which increases the drag coefficient. Specifically, as the deflection angle increases from 15° to 30°, there is a corresponding increase in the drag coefficient mainly attributed to the lift-induced drag contribution.

In Figure 4.29 the effect of the flap on the pitching moment coefficient is shown. As expected, the contribution of the flap is to create a negative pitching moment, due to the deflection of the surface located behind the aerodynamic center. Additionally, the higher is the deflection angle, the higher is the negative pitching moment increment. In the case of clean wing (flap deflection equal to 0°), the pitching moment has an initial positive increase with angle of attack. Conversely with flap at 15° and 30° the trend of the curve is towards negative values, more negative if larger deflection angles are considered. This change in pitching moment curve slope is attributed to a backward shift of the aerodynamic center.

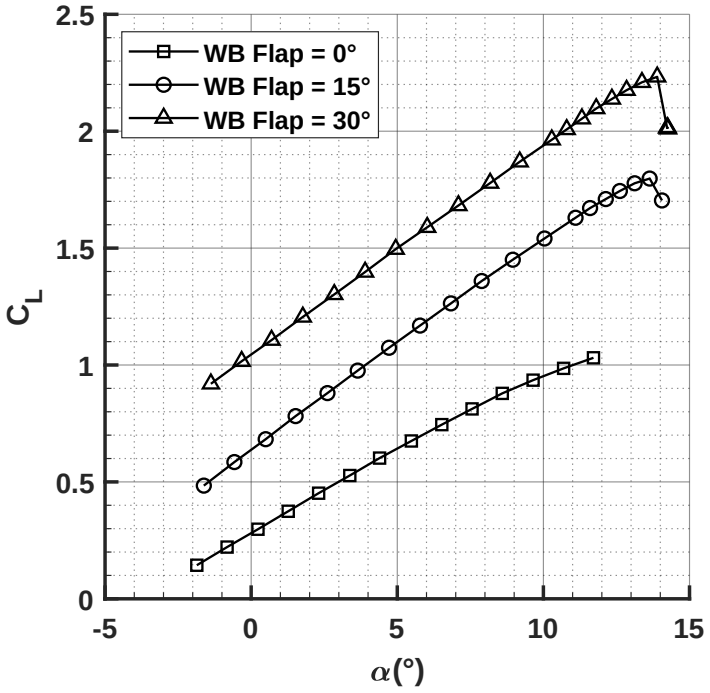

Figure 4.27 Effects of the fowler flap on the lift coefficient with $Re = 430000$. The lift slope is approximately $C_{L_\alpha} = 0.073$ deg^{-1} and 0.092 deg^{-1} for the clean and flapped configurations, respectively.

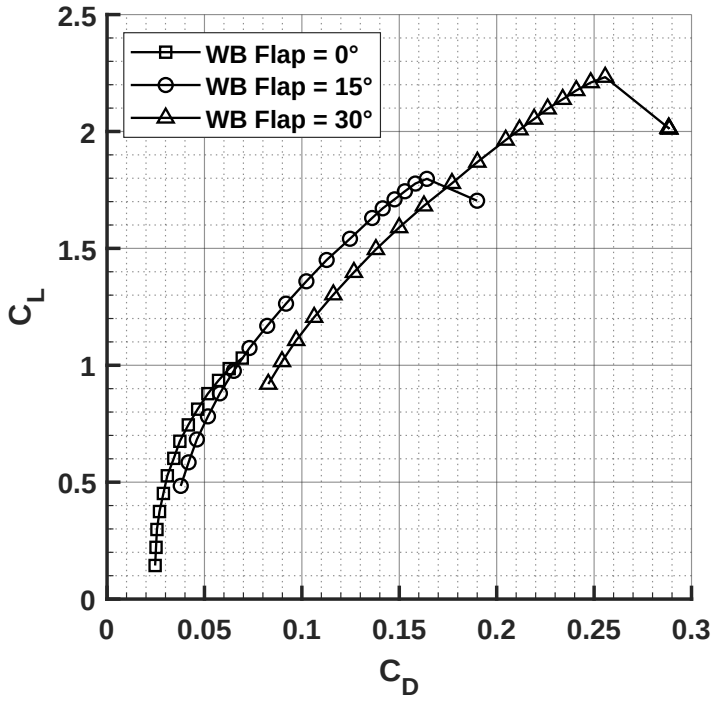

Figure 4.28 Effects of the fowler flap on the polar curve with $Re = 430000$.

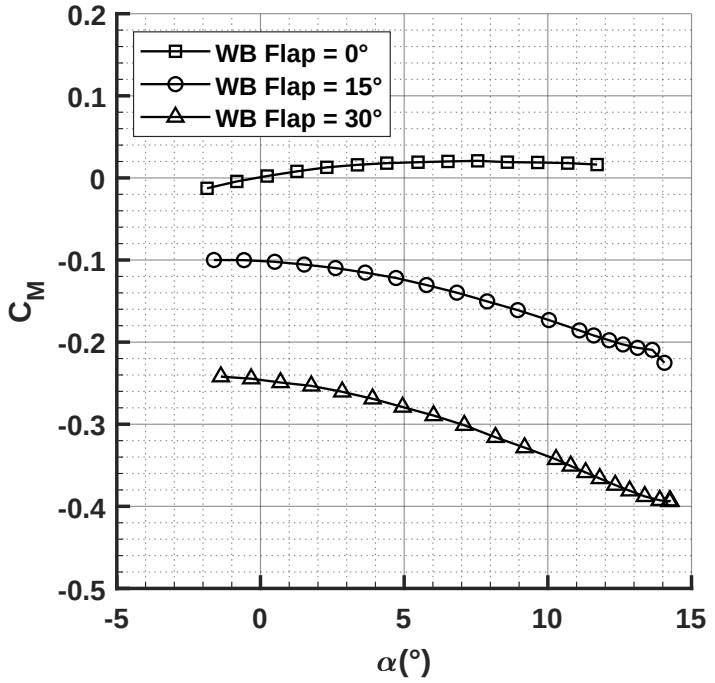

Figure 4.29 Effects of the fowler flap on the pitching moment coefficient with $Re = 430000$.

4.3.5 Repeatability of values

The repeatability of wind tunnel tests is a measure of the consistency of results obtained from multiple tests or measurements conducted under the same conditions. In the wind tunnel, repeatability is a crucial factor in determining the reliability of the results. The repeatability can be affected by variations in measuring instruments, test model location in the test chamber, and measurement techniques. To determine the repeatability of wind tunnel tests, multiple runs of the same test are typically conducted and the results are compared to define the mean value and standard deviation. In this case, for the wing-body configuration with flap at 0°, three wind tunnel tests have been conducted at the same flow speed ($V_\infty = 35$ m/s). These tests were executed on different days and after several configuration changes. They are not three consecutive tests and thus they include the effect of model installation.

The wind tunnel tests have provided vectors of angle of attack, lift, drag, and pitching moment coefficients for each test. Thus, by taking the three values of angle of attack from the three different tests, it has been possible to evaluate the mean value and the standard deviation. The same has also been done for the lift, drag, and pitching moment coefficients. The mean values and standard deviation related to angle of attack and aerodynamic coefficient are shown in Table 4.4.

Table 4.4 Mean values and standard deviations, WB configuration.

α (deg)		C_L		C_D		C_M	
avg.	st.dev.	avg.	st.dev.	avg.	st.dev.	avg.	st.dev.
0.205	0.0311	0.300	0.0029	0.026	0.0006	0.002	0.0004
−0.820	0.0319	0.224	0.0042	0.025	0.0003	−0.005	0.0008
−1.853	0.0250	0.147	0.0050	0.024	0.0002	−0.013	0.0010
1.270	0.0380	0.378	0.0050	0.027	0.0004	0.008	0.0007
2.311	0.0330	0.456	0.0047	0.029	0.0006	0.012	0.0007
3.367	0.0428	0.532	0.0051	0.032	0.0007	0.016	0.0003
4.407	0.0372	0.607	0.0054	0.035	0.0006	0.018	0.0002
5.475	0.0387	0.680	0.0053	0.038	0.0008	0.019	0.0003
6.518	0.0382	0.750	0.0053	0.042	0.0008	0.020	0.0003
7.574	0.0471	0.818	0.0054	0.047	0.0010	0.020	0.0005
8.593	0.0269	0.885	0.0057	0.053	0.0010	0.019	0.0003
9.647	0.0455	0.941	0.0055	0.058	0.0009	0.018	0.0006
10.691	0.0149	0.993	0.0062	0.064	0.0010	0.017	0.0007
11.716	0.0219	1.037	0.0058	0.070	0.0010	0.016	0.0005

4.4 Complete configuration tests

In order to continue the evaluation of the aircraft components effect on the longitudinal stability, tests have been performed on another configuration. Specifically, the entire aircraft, including the vertical and horizontal tailplane, has been tested to assess its aerodynamic characteristics. The tail, made up of horizontal and vertical planes joined together, has been installed in the rear part of the fuselage and it has been fixed with three screws. Figure 4.30 shows the complete aircraft model configuration mounted on the balance plate in the wind tunnel. This configuration is indicated as WBHV.

Figure 4.30 Complete test model configuration (WBHV) in the wind tunnel.

The effect of the fowler flap on the complete aircraft model configuration has been measured. Figure 4.31 and 4.32 show photos of the model in the test chamber with flap deflected at 15° and 30°, respectively.

As with the wing-body configuration, the lift coefficient of the complete aircraft model is affected by the fowler flap deflection at 15° and 30°, as shown in Figure 4.33. As the wing surface is extended, the lift slope is increased compared to the clean configuration. As the flap is rotated to increase the camber, the lift coefficient is increased. The fowler flaps at 15° and 30° leads to an approximately lift coefficient increment of $\Delta C_L = 0.4$ and 0.8, respectively, compared to the clean configuration at zero angle of attack. It should also be noted that the maximum lift coefficient achieved with 30° of flap deflection, a typical angle for landing configuration, is $C_{L_{\max}} = 2.3$.

The drag polar curve is also affected by the flap rotation, as shown in Figure 4.34. The curve shifts towards higher values of drag coefficient with increasing the flap

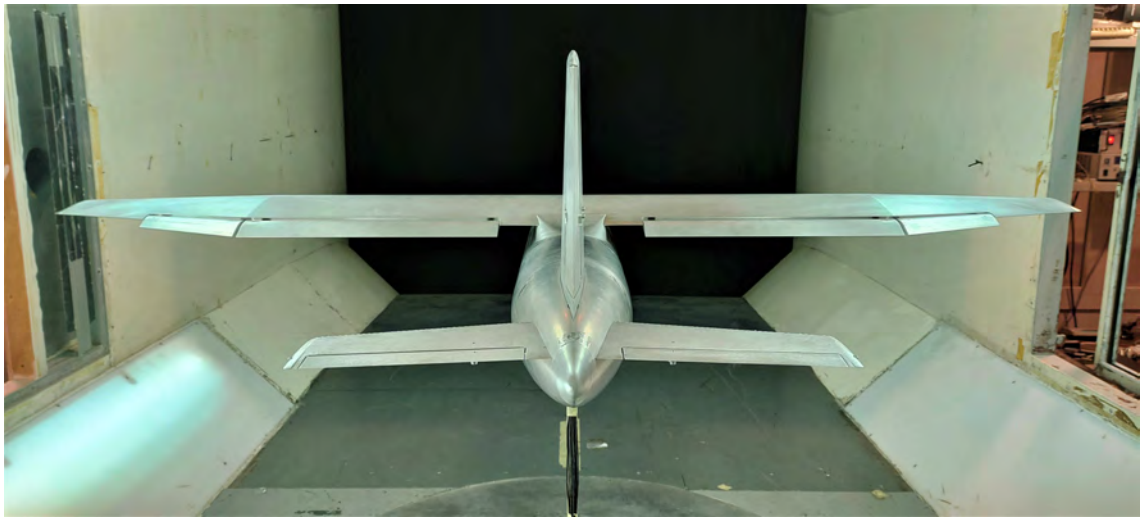

Figure 4.31 Complete aircraft model configuration with flap deflection of 15° for the take-off phase.

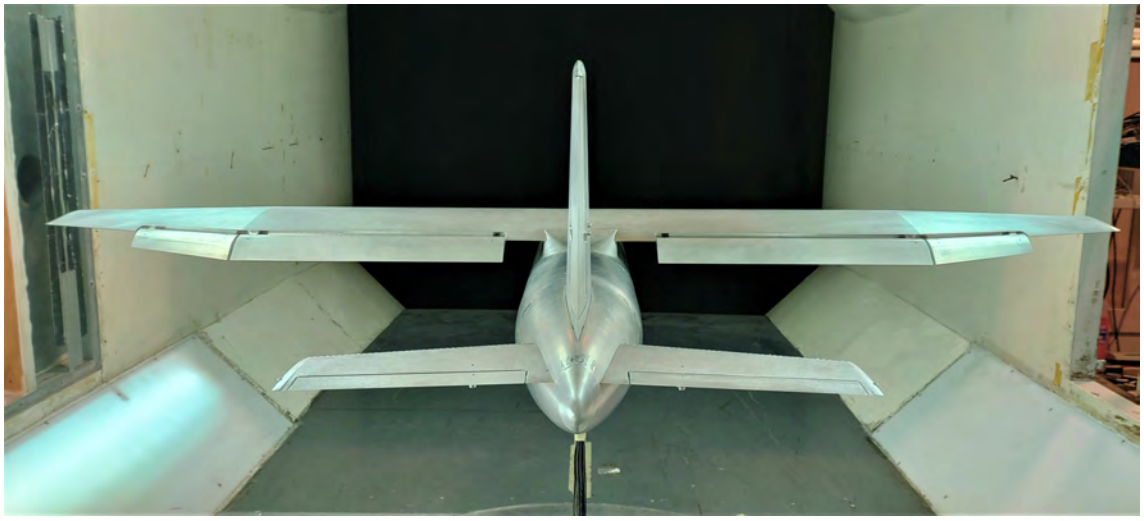

Figure 4.32 Complete aircraft model configuration with flap deflection of 30° for the landing phase.

deflection angle. Additionally, as the flap rotates from 15° to 30°, the drag polar curve shows an increment of the lift coefficient but also a significant increase of the drag coefficient, largely due to lift-induced drag.

The contribution of the flap on the pitching moment coefficient is highly relevant, as shown in Figure 4.33. The pitching moment becomes more negative as the flap deflection angle increases. In Figure 4.33, two changes in the pitching moment slope can also be observed. The first variation, at low angle of attack, is caused by the initial reduction of the downwash angle ϵ with respect to the angle of attack α increment, i.e., a change in downwash gradient $\mathrm{d}\epsilon/\mathrm{d}\alpha$. The second variation is attributed to the same phenomenon, but is related to high values of the angle of attack where the flow separation on the wing is reducing its downwash. This leads to a larger nose-down contribution of the horizontal tail. Specifically, for a high wing configuration, as the angle of attack increases, the wake moves away from the tailplane, increasing the vertical distance of the former from the latter. This results in a cleaner flow on the horizontal tail and thus a larger longitudinal stability (a steeper slope of the pitching moment curve) of the aircraft configuration.

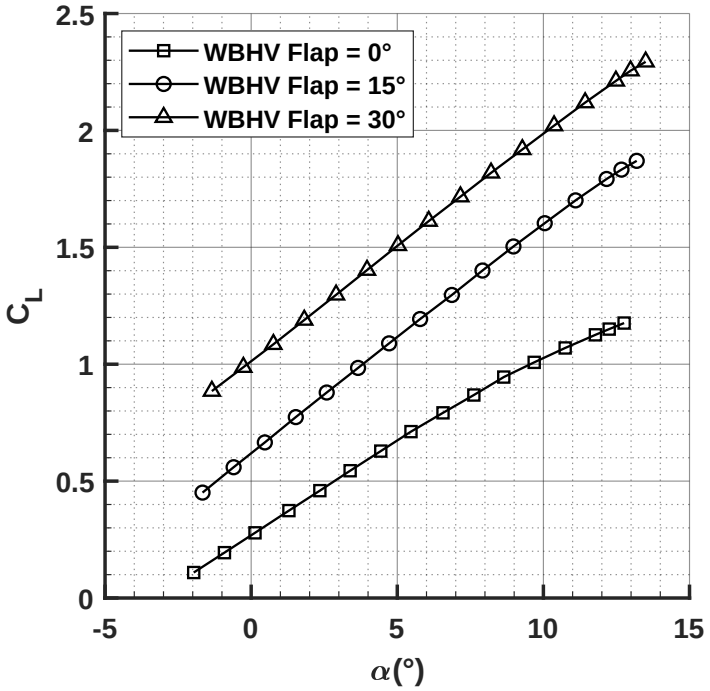

Figure 4.33 Effect of the fowler flap on the lift coefficient with $Re = 430000$. The lift slope is approximately $C_{L_\alpha} = 0.081$ deg^{-1} and 0.099 deg^{-1} for the clean and flapped configurations, respectively.

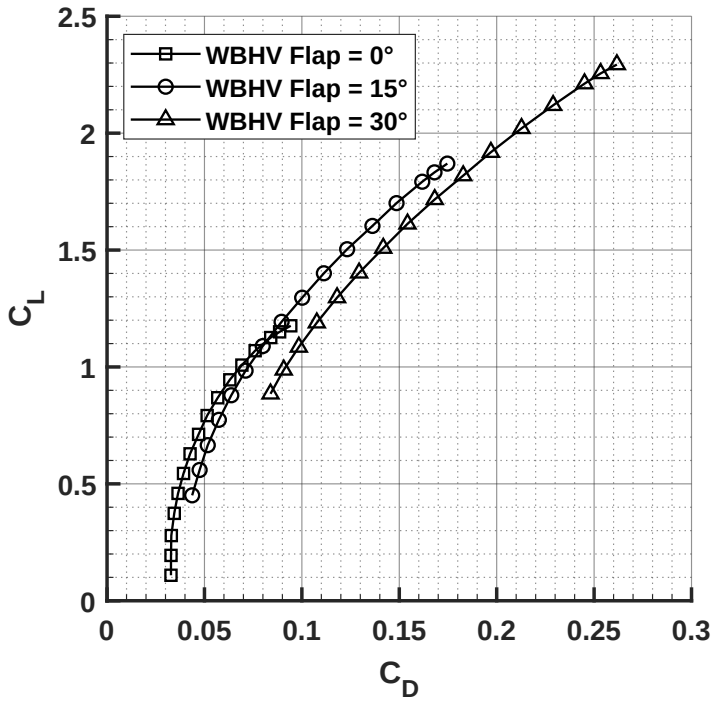

Figure 4.34 Effect of the fowler flap on the polar curve with $Re = 430000$.

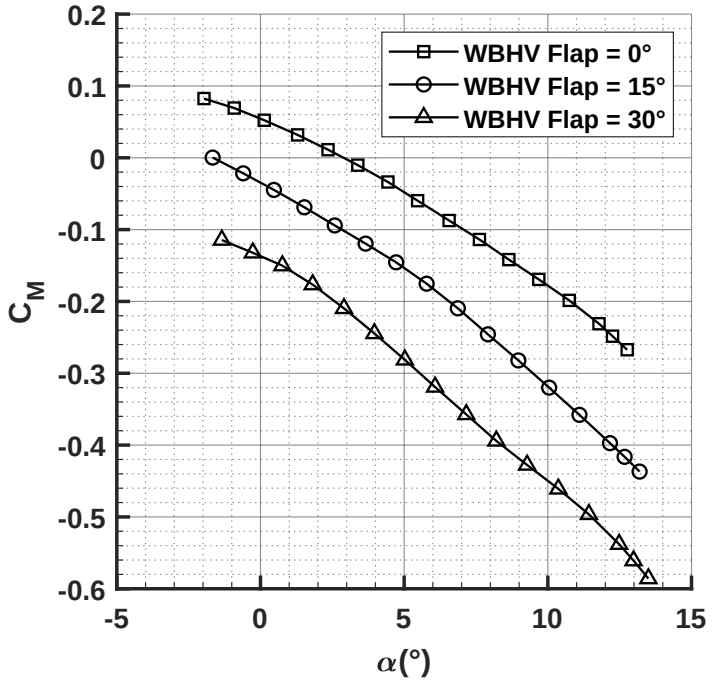

Figure 4.35 Effect of the fowler flap on the pitching moment coefficient with $Re = 430000$.

4.4.1 Horizontal tailplane effect

The idea to observe the advantages of mounting the horizontal tail in the fuselage, as shown in Figure 4.36, can be discussed by comparing the aerodynamic curves of the wing-body and complete configurations. Additionally, the comparison of flap deflection at angles of 0°, 15°, and 30° for the two configurations has also been reported.

Figure 4.36 Detail of the horizontal tailpane mounted in the fuselage.

The analysis of the lift coefficient in Figure 4.37 reveals the influence of the horizontal plane on the lift. Specifically, the curves related to the complete configuration (WBHV) have a steeper slope compared to the wing-body (WB) configuration, as reported also in Table 4.5, resulting in a higher lift produced by the former. Thus, the increase in lift coefficient can be attributed to the presence of the horizontal tailplane.

In the drag polar curve of Figure 4.38 the effect of the horizontal tail is also present. In detail, at low values of C_L, the drag coefficient C_D of the WBHV configuration appears to increase much more than the drag coefficient at higher C_L. This suggests that the horizontal tail added to the fuselage affects the parasite drag more than the induced drag.

The pitching moment coefficient in Figure 4.39 compares the two configurations. The advantages of the horizontal tail are clearly visible. While the pitching moment coefficient of the WB configuration appears to decrease slightly in some cases (flap at 15° and 30°), the curves of the WBHV configuration have a steeper negative slope, indicating the longitudinal stability of this configuration. According to the theory [27], the stability of a conventional configuration is achieved when the derivative of

the pitching moment coefficient C_{M_α} is negative. This means that as a perturbation tends to increase the angle of attack, the pitching moment coefficient becomes more negative, indicating that the aircraft will tend to reduce the angle of attack.

Table 4.5 Lift curve slope of WB and WBHV configurations evaluated on the acquired data in the range of $\alpha \in [0° - 5°]$.

Configuration	C_{L_α} (deg^{-1})
WB Flap 0°	0.073
WBHV Flap 0°	0.081
WB Flap 15°	0.093
WBHV Flap 15°	0.100
WB Flap 30°	0.091
WBVH Flap 30°	0.098

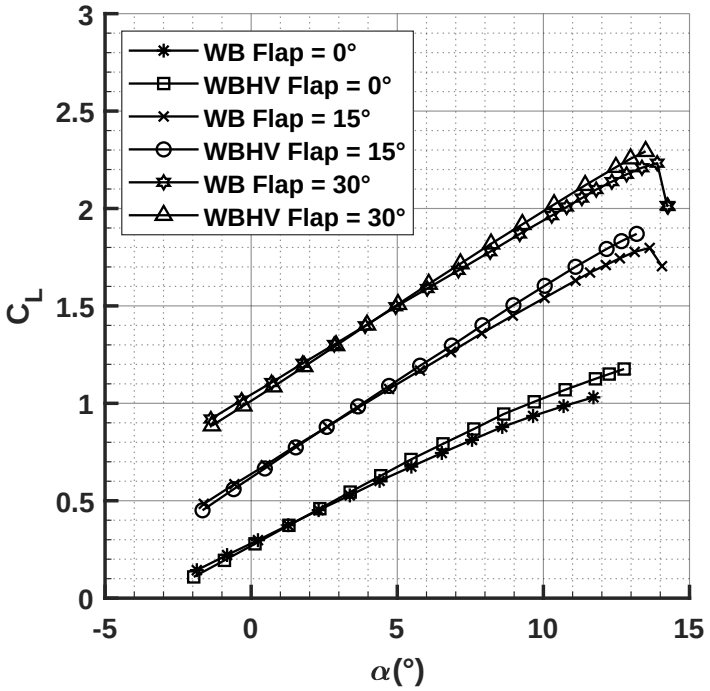

Figure 4.37 Effects of the horizontal tailplane and fowler flap on the lift coefficient with $Re = 430000$. The lift curve slope are reported in Table 4.5.

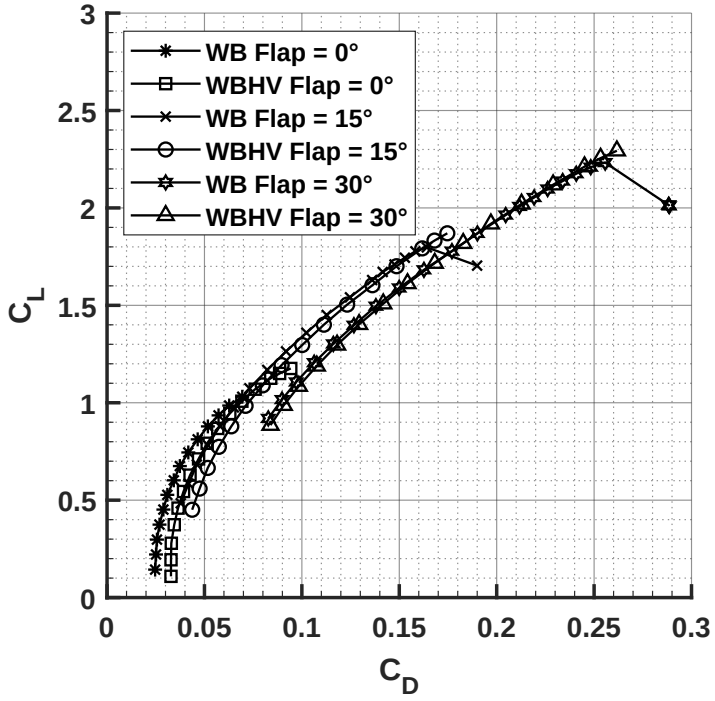

Figure 4.38 Effects of the horizontal tailplane and fowler flap on the polar curve with $Re = 430000$.

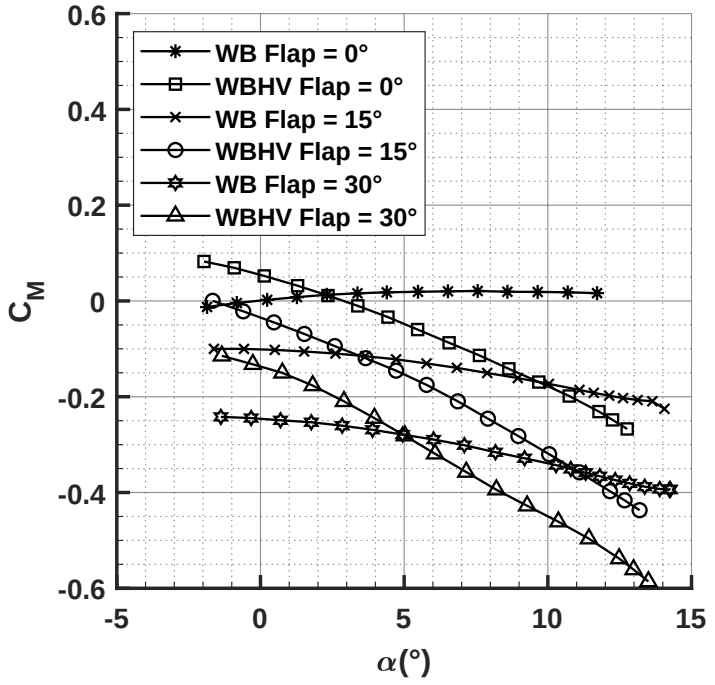

Figure 4.39 Effects of the horizontal tailplane and fowler flap on the pitching moment coefficient with $Re = 430000$.

4.4.2 Neutral point evaluation

An aircraft is considered to be longitudinally statically stable when a disturbance in the angle of attack results in a pitching moment that tends to restore the aircraft to its original state of equilibrium [27]. The stability is strictly related to the center of gravity (in this case, it is the pole assumed to be at 25% of MAC) and neutral point N_0. The neutral point is defined as the longitudinal position about which the pitching moment coefficient is invariant with the angle of attack. According to the literature [27], the distance between the center of gravity (CG) and the neutral point (N_0) of an aircraft can be determined by using the slope of the pitching moment coefficient (C_M) evaluated at the CG versus the slope of the lift coefficient (C_L). This distance is also known as static margin. Considering the following equation:

$$\left.\frac{C_{M_\alpha}}{C_{L_\alpha}}\right|_{\text{CG}} = C_{M_{C_L}} = \overline{x}_{\text{CG}} - \overline{x}_{N_0} \tag{4.2}$$

the center of gravity $\overline{x}_{\text{CG}}$ and the neutral point $\overline{x}_{N_0}$ coordinates are both expressed as a fraction of MAC. By inverting Equation 4.2, it has been possible to evaluate the neutral points of the complete configuration with flap deflection angles at 0°, 15°, and 30°, as reported in Table 4.6.

Table 4.6 Neutral point for various configurations as fraction of MAC. Lift and pitching moment curve slope evaluated in the range of $\alpha \in [0° - 5°]$.

Configuration	$\overline{x}_{N_0}$	C_{L_α} (deg^{-1})	C_{M_α} (deg^{-1})
WBHV Flap 0°	0.475	0.081	−0.018
WBHV Flap 15°	0.479	0.100	−0.023
WBVH Flap 30°	0.520	0.098	−0.026

The effect of the flap on neutral point positions can also be observed. In the WBHV configuration, as the flap deflection angle increases, the neutral point shifts backwards with respect to the pole (chosen at 25% of MAC). This effect can be explained observing the Equation (4.2), which includes the slope of C_M and C_L. Increasing the fowler flap deflection increases the magnitude of the ratio $C_{M_\alpha}/C_{L_\alpha}$. At flap deflected by 15°, the neutral point N_0 shifts backwards by a small amount with respect to the clean configuration. When the flap deflection angle is set to 30°, the backward shift of N_0 is much larger. Generally, the longitudinal stability is achieved when the CG is located ahead the N_0. Thus, in this case the configuration appears to be statically stable because the CG (pole chosen at 25% of MAC) is forward with respect to the neutral points estimated in Table 4.6.

4.4.3 Elevator deflection effect

The elevator is a control surface, a mobile part of the horizontal tailplane, which controls the aircraft pitch and therefore the angle of attack of the wing. The elevator rotates around an hinge with respect to a fixed part known as the stabilizer [27]. The deflection of the elevators has been taken into account during the wind tunnel tests. Several aluminum supports, made using a CNC machine, have allowed for the elevator to be deflected at angles of $\delta_e = -5°, -10°, -20°, -25°$ which means that the trailing edge of the surface has been moved upwards. The tests have been conducted at $V_\infty = 35$ m/s on the complete configuration with flaps set to 0°, as shown in Figure 4.40.

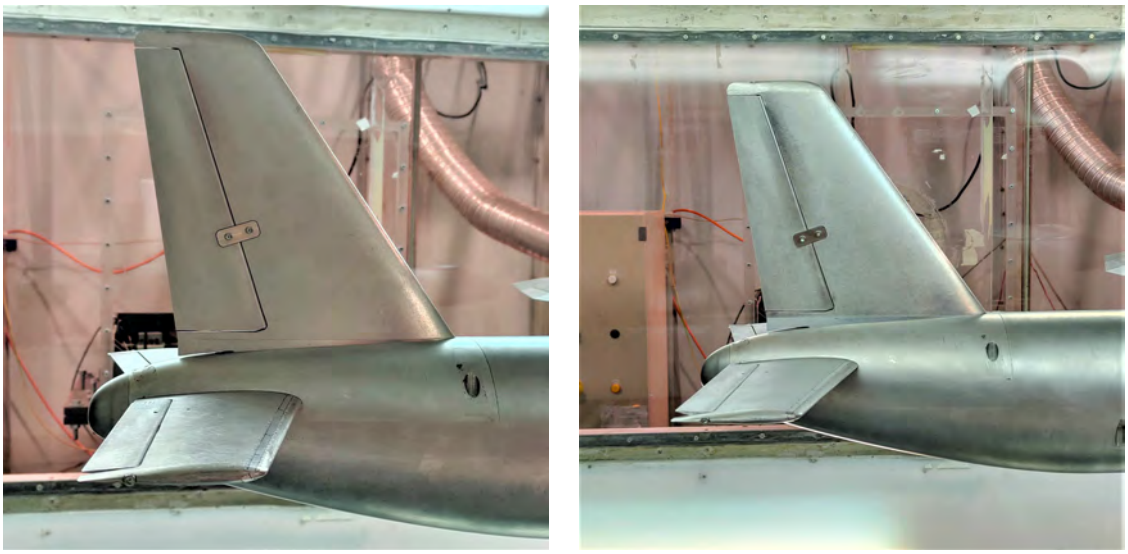

(a) $\delta_e = -5°$ **(b)** $\delta_e = -10°$

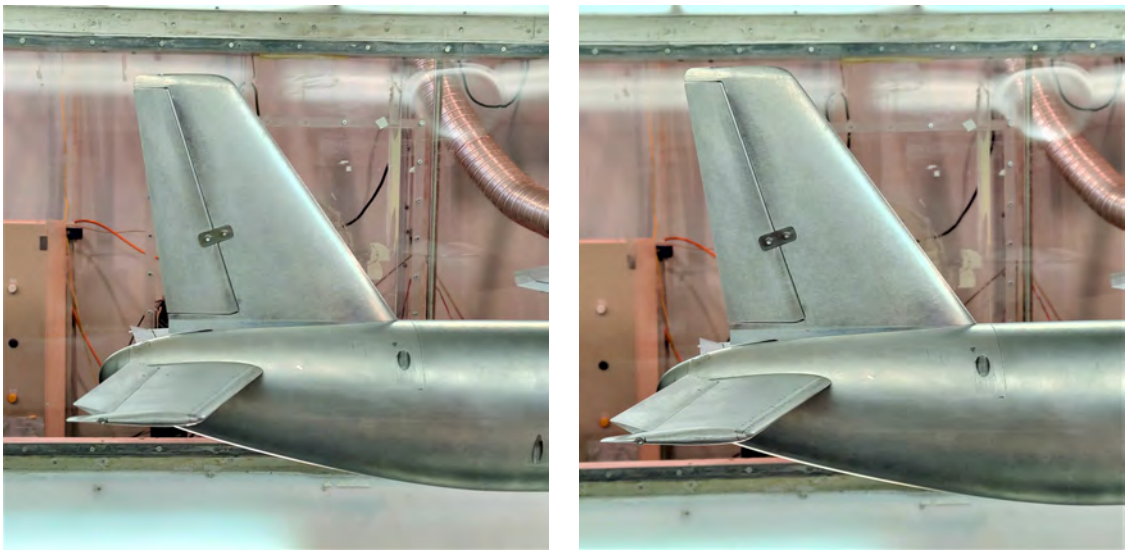

(c) $\delta_e = -20°$ **(d)** $\delta_e = -25°$

Figure 4.40 The investigated elevator's deflections.

The data acquired during the tests have been processed to determine the aerodynamic coefficients. As shown in Figure 4.41, the comparison between the lift coefficient of the complete configuration with an elevator deflection angle of 0° and −5° reveals that the variation in lift coefficient is negligible between the two curves. However, when the deflection angle is changed towards more negative values −10°, −20°, −25°, the lift coefficient decreases slightly. This can be explained by considering that the total lift of the aircraft model is composed of the sum of the wing and tail contributions. By moving the elevator upwards, the positive lift contribution of the tail decreases. The lift coefficient of the tail is reduced as the δ_e is increased to more negative values. This results in a reduction in the total lift coefficient as shown in Figure 4.41.

The impact of varying the δ_e is also insignificant on the drag polar curve at low values of elevator deflection, as shown in Figure 4.42. As a result, the curves at lower elevator deflections appear to be superimposed. However, as the elevator deflection is increased, the drag curves shift towards higher drag coefficients. In detail, the increase in the parasite drag becomes relevant, as shown in Figure 4.42.

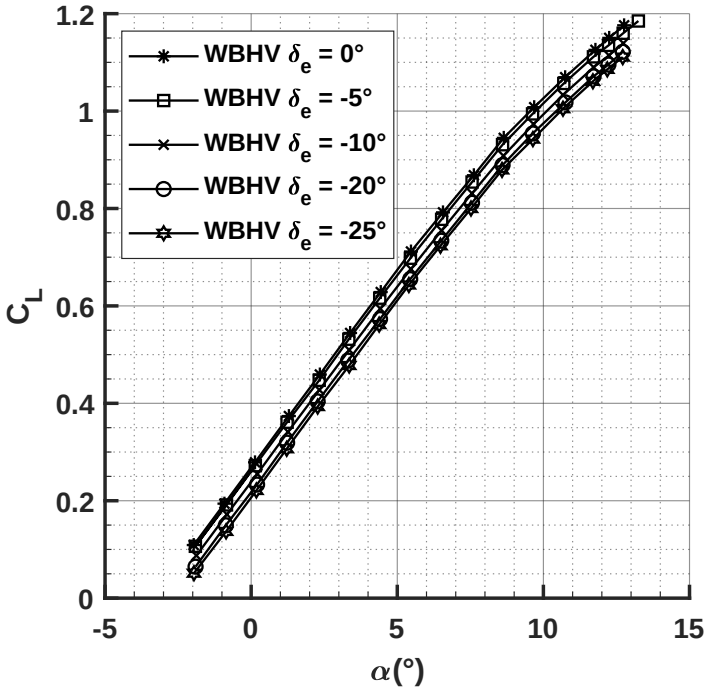

Figure 4.41 Effect of the elevator deflection on the lift coefficient with $Re = 430000$. The lift slope $C_{L_\alpha} = 0.081$ deg^{-1} for all elevator deflections δ_e.

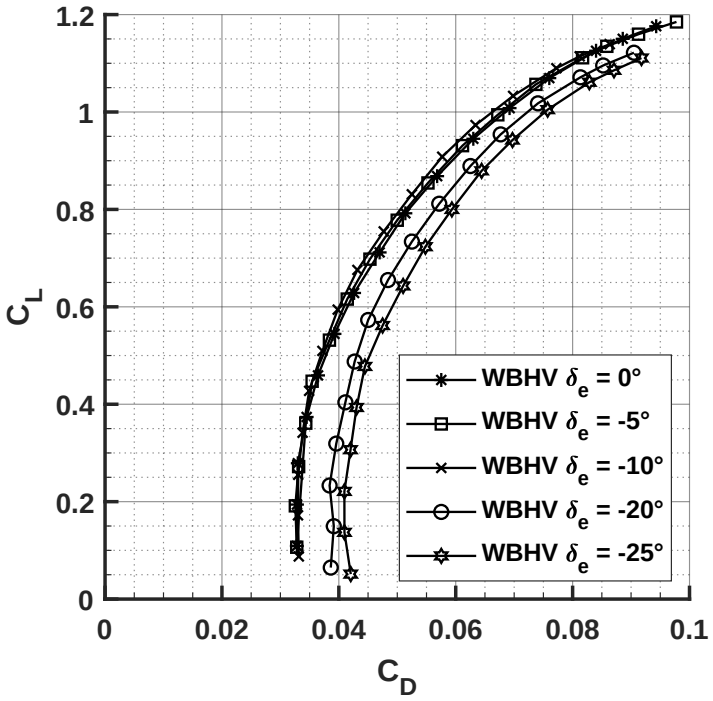

Figure 4.42 Effects of the elevator deflection on the drag polar curve with $Re = 430000$.

Figure 4.43, on the other hand, illustrates the expected effect of elevator deflection on the pitching moment. As the rotation of the elevator changes the resultant of the forces acting on the horizontal tailplane, which has a finite distance with respect to the reference, the effect on the pitching moment is visible. This effect results in a variation of the pitching moment, as shown in Figure 4.43, where the moment curve shifts upward when the elevator deflection is upward. In detail, increasing δ_e towards negative values, the equilibrium condition ($C_M = 0$) is achieved at an increased α, as reported in Table 4.7. The visible effect on the aircraft when the elevator is deflected upward is a positive pitching moment increment.

Table 4.7 Equilibrium conditions at several elevator deflection angles.

Configuration	α_e	C_{L_e}
WBHV $\delta_e = -0°$	2.51	0.47
WBHV $\delta_e = -5°$	3.90	0.56
WBHV $\delta_e = -10°$	6.19	0.70
WBHV $\delta_e = -20°$	8.87	0.88
WBHV $\delta_e = -25°$	10.06	0.96

Considering the known value acquired for the two lift coefficient curves with $\delta_e = 0°$ and $-5°$, it was also possible to evaluate the derivative of C_L with respect to the derivative δ_e at $\alpha = 0°$, using the incremental ratio $\Delta C_L/\Delta\delta_e$. This value, also

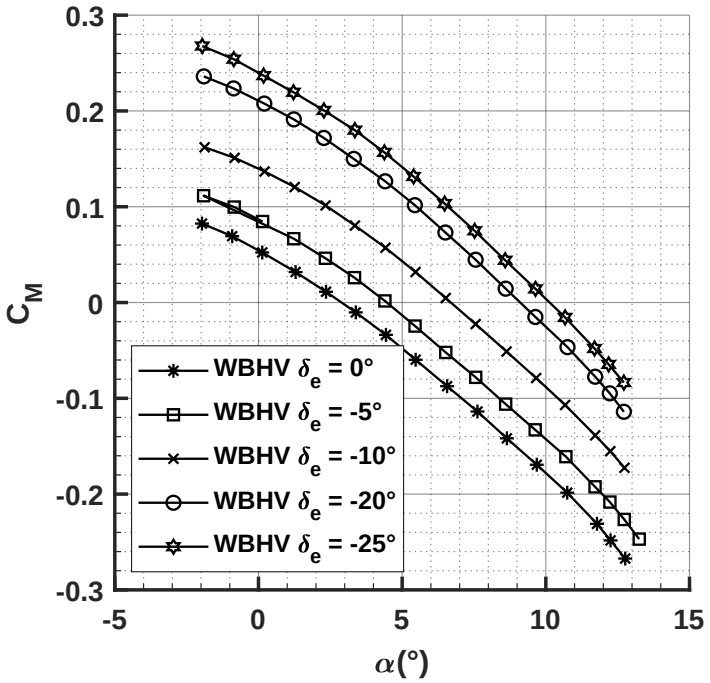

Figure 4.43 Effects of the elevator deflection on the pitching moment coefficient with $Re = 430000$.

known as $C_{L_{\delta_e}}$ describes how the lift coefficient changes as the elevator is deflected. Similarly, the value $C_{M_{\delta_e}}$, known as the control power of the elevator, was evaluated with values of C_M at $\alpha = 0°$ acquired with $\delta_e = 0°$ and $-5°$, using the incremental ratio $\Delta C_M/\Delta\delta_e$. Furthermore, the elevator efficiency $\tau_e = d\alpha/d\delta_e$, which refers to the ability of the elevator control surface to effectively change the pitch attitude of an aircraft, was estimated as the ratio $C_{M_{\delta_e}}/C_{M_\alpha}$ and its variation with δ_e is shown in Figure 4.44. These calculations are also repeated for different levels of elevator deflection, the results are reported in Table 4.8. The Figure 4.45 shows the trimmed lift curve that intersects the various C_L curves obtained for different deflections of the elevator. The values of equilibrium related to the lift coefficient and angle of attack are reported in Table 4.7.

Table 4.8 Aerodynamic coefficients derivatives with respect elevator deflection and elevator effectiveness.

Configuration	$C_{L_{\delta_e}}$	$C_{M_{\delta_e}}$	τ_e
WBHV $\delta_e = -5°$	-0.0010	0.0067	-
WBHV $\delta_e = -10°$	-0.0030	0.0086	0.47
WBHV $\delta_e = -20°$	-0.0050	0.0079	0.43
WBHV $\delta_e = -25°$	-0.0061	0.0075	0.41

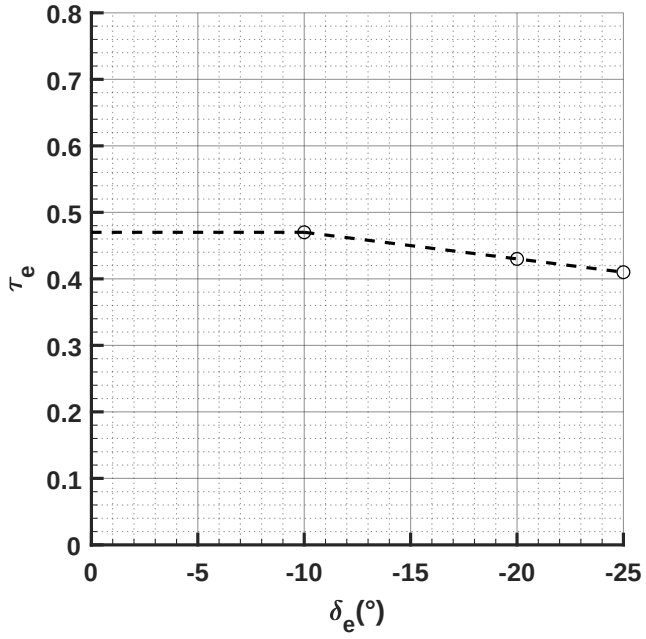

Figure 4.44 Relationship between elevator effectiveness and deflection.

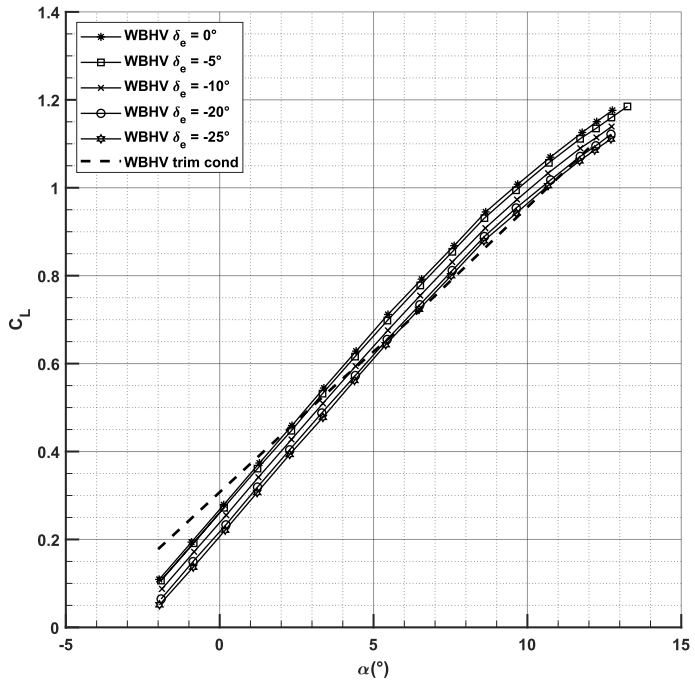

Figure 4.45 Effect of the elevator deflection on the lift coefficient with $Re = 430000$. The lift slope $C_{L_\alpha} = 0.081$ deg^{-1} for all elevator deflections, while the slope of the trimmed lift curve $C_{L_{\alpha_{\text{trim}}}} = 0.065$ deg^{-1}.

5

Conclusions and future works

5.1 Conclusions

Main objectives of this research work have been:

- identifying the possibility of introducing new solutions for the commuter aircraft that can reduce emissions in the atmosphere;
- discussing different types of wind tunnel tests that have been developed over the years;
- describing the wind tunnel test adopted to conduct the tests on the aircraft model and the software developed to acquire the results during the test campaign;
- conducting several longitudinal tests on different aircraft configurations.

The complete procedure followed for these test campaigns has been:

- installation of the pitching attitude control;
- installation of the balance on the previous pitching attitude control;
- development of the data acquisition software `DAQ_Long`;
- verification of measurements acquired by the software `DAQ_Long` using known masses;
- installation of aircraft model in the test section;

- acquisition with the developed virtual instrument `taraPesi.vi`, with wind tunnel off, of the balance measurements for several angles of attack, to define the coefficients of the second order polynomial and thus evaluate the net forces/moments during the test with tunnel on;
- conducting longitudinal wind tunnel tests on the aircraft model and acquiring data with developed software `DAQ_Long`.

The scale model of the aircraft has been widely tested in the main subsonic wind tunnel of the DII. This test campaign of the aircraft model belonging to the commuter category has required the installation of the aircraft in the test section using several measurement instruments. The installation procedure has begun placing the fuselage at the base of the sting first, then attaching the wing to the balance plate, and finally fixing the fuselage to the wing with screws. Afterwards, the horizontal and vertical tailplanes have been mounted to conduct the longitudinal tests on the total configuration. Before installing the aircraft model, a check of the forces measured by the balance and acquired by the program had been carried out using known masses. The data acquisition has required the development of a code using LabVIEW. This acquisition software had the capability to acquire signals voltage of axial and longitudinal forces, pitching moment, dynamic pressure, angle of attack, temperature and obtain values of forces, moment and others. These value have been manipulated to derive the uncorrected and corrected aerodynamic coefficients. The correction has been necessary, due to the presence of the walls of the test section that change the working conditions of the flow around the aircraft compared to the actual flight conditions.

The results of the experimental investigation of the wing-body configuration have been acquired. A first test has been conducted at a $V_\infty = 35$ m/s to observe the correction effects on the aerodynamic coefficients: lift, drag and pitching moment. Then, data have been also acquired at two different speed, $V_\infty = 35$ m/s and $V_\infty = 25$ m/s, to make the comparison of the aerodynamic curves. It is visible how, as the speed increases, the Reynolds number increases, and this effect results in changes to the polar and pitching moment; while it is less visible in the lift coefficient. The tests with trip strips have been conducted at $V_\infty = 35$ m/s, and the aerodynamic coefficient derived have been compared with those obtained without trip strips. The results show the great advantage of using trip strips, especially in terms of lift and pitching moment, which change their behaviour. However, on the other hand, the trip strips appear to be a disadvantage on the polar curve because there is an increase in drag. The analysis of wing-body configuration with flap at angles 15° and 30° has highlighted the advantages to use the fowler flaps. In particular, lift and lift slope are increased, while the drag and pitching moment become higher as the deflection angle of the flap increases. The complete configuration, with horizontal and vertical tail installed in the fuselage have been tested at a $V_\infty = 35$ m/s. The aerodynamic results show the effect of the fowler flap on the complete aircraft model. Similar

to the WB configuration, the flap causes an increase in lift coefficient, a change in lift slope, an increase in drag and in pitching moment coefficient. A comparison is made between WBHV and WB configurations with different flap deflections. These results highlight the need of installing a horizontal tail in addition to the wing-body configuration. The tail provides lift and also increases the drag, but it is crucial for the pitching moment to achieve a stable configuration. The deflection of the elevator has also been applied during the tests campaign. This effect is primarily observed in the pitching moment coefficient rather than in the lift and drag coefficients, when the elevator deflection angle δ_e is low.

The major limitation of these tests is related to the low Reynolds number achievable at which the experimental test have been performed. This is attribute to the *scale effects* which is referred to differences that arise when the fluid dynamic dimensionless parameters, primarily the Reynolds number, are not the same in low-speed wind tunnel tests and flight operations. Therefore, the main impact of this limitation is on the drag polar curve obtained from wind tunnel tests, which may not be fully representative of the actual flight conditions.

5.2 Future works

Future work will primarily focus on these key areas: i) conducting experimental investigations on the effect of cover battery on aerodynamic characteristics, with a particular emphasis on drag; ii) developing new data acquisition software for lateral-directional testing phase; iii) investigating the lateral-directional stability and control for various aircraft configurations; iv) determining the power effects on aerodynamic characteristics through the use of ten electric engines installed on a fixed support within the test section.

A

CAD Model

The following drawings of the CAD model are reported:

1. Model 3-view
2. Frontal and rear view
3. Top and bottom view
4. Lateral view
5. Exploded view
6. Frontal and lateral view in the wind tunnel
7. Generic view in the wind tunnel

The components visible in the exploded view, Figure A.5, are the following:

1. fuselage
2. wing
3. vertical tail
4. forward battery cover
5. forward fuselage cover
6. horizontal tailplane
7. longitudinal balance
8. balance sting
9. aft fuselage cover
10. aft battery cover

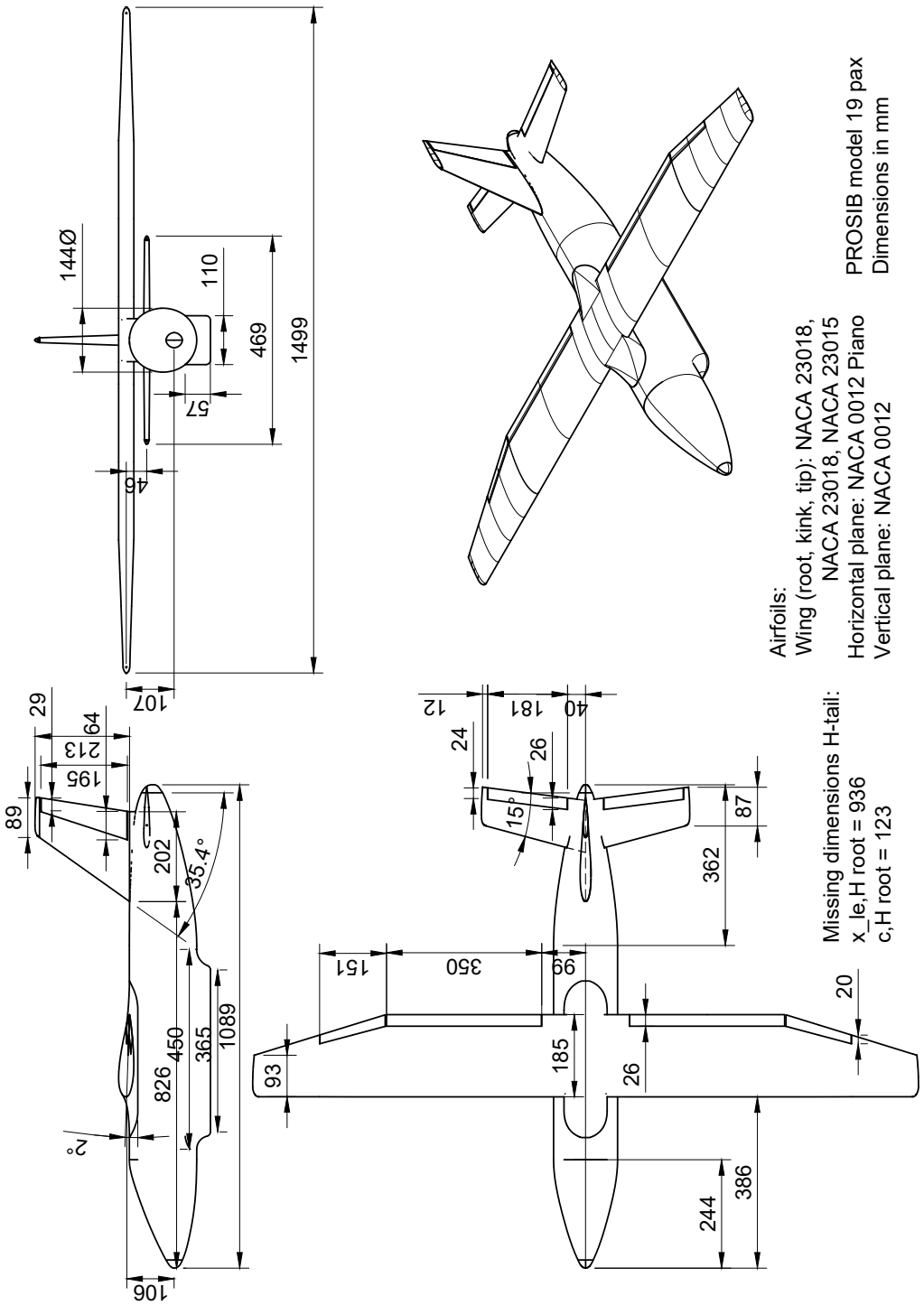

Figure A.1 Three view of the PROSIB model 19 pax.

(a)

(b)

Figure A.2 Frontal and rear view of the PROSIB CAD model 19 pax.

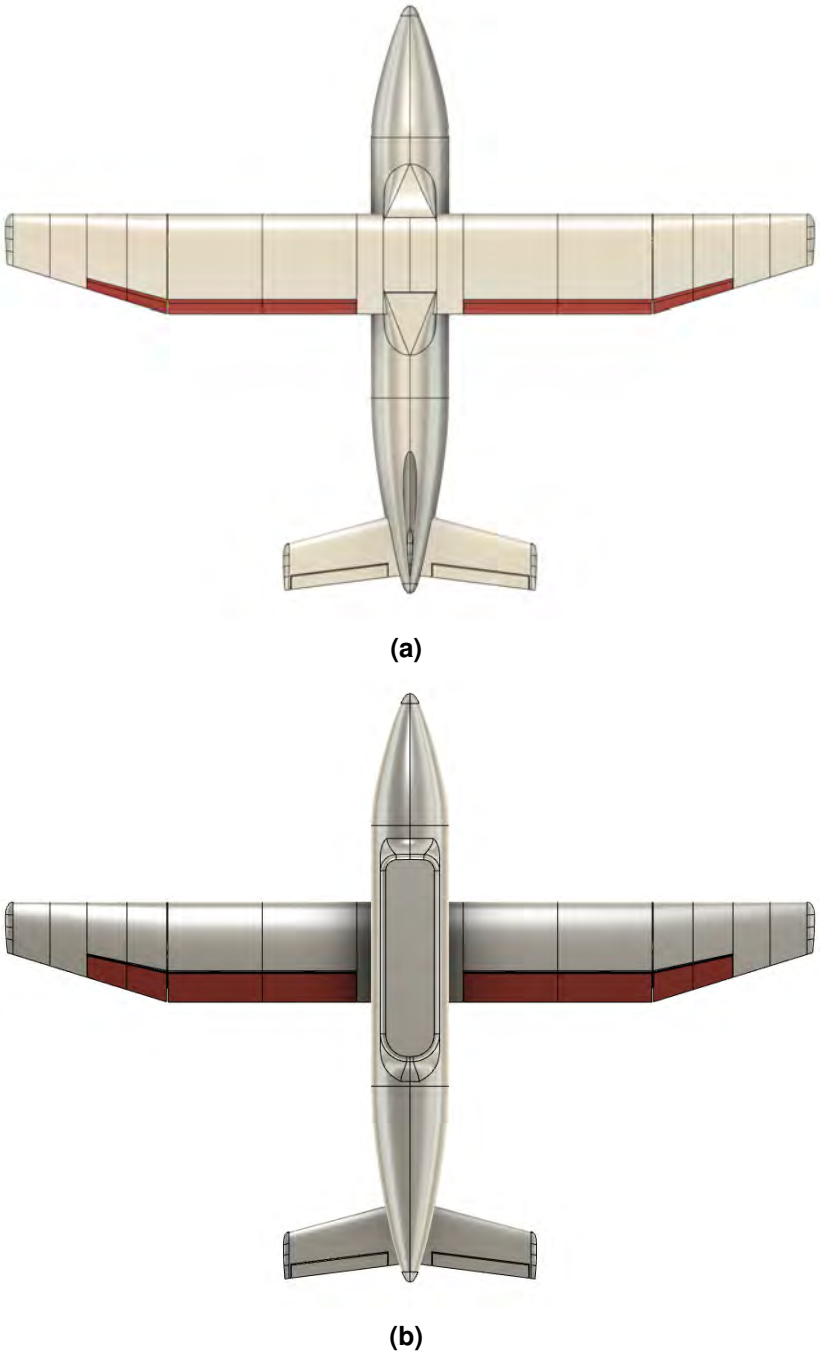

(a)

(b)

Figure A.3 Top and bottom view of the PROSIB CAD model 19 pax.

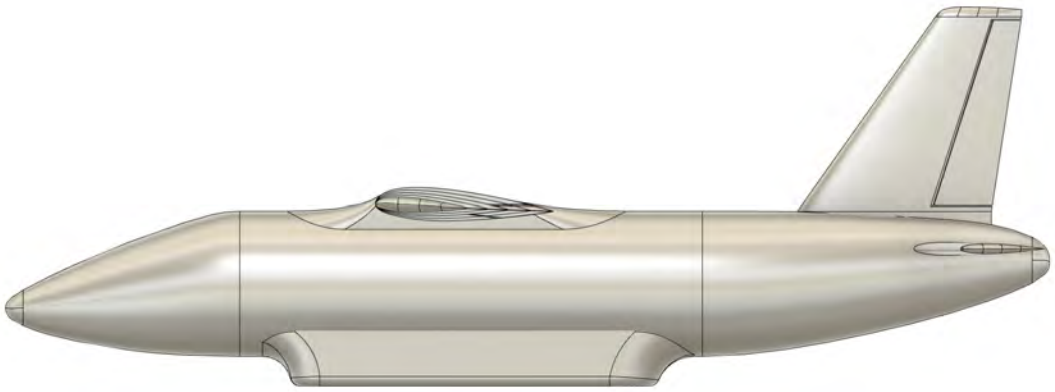

(a)

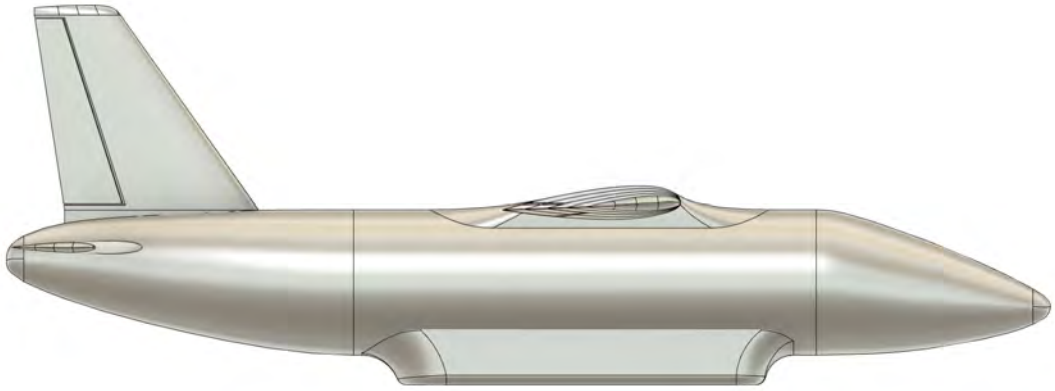

(b)

Figure A.4 Lateral view of the PROSIB CAD model 19 pax.

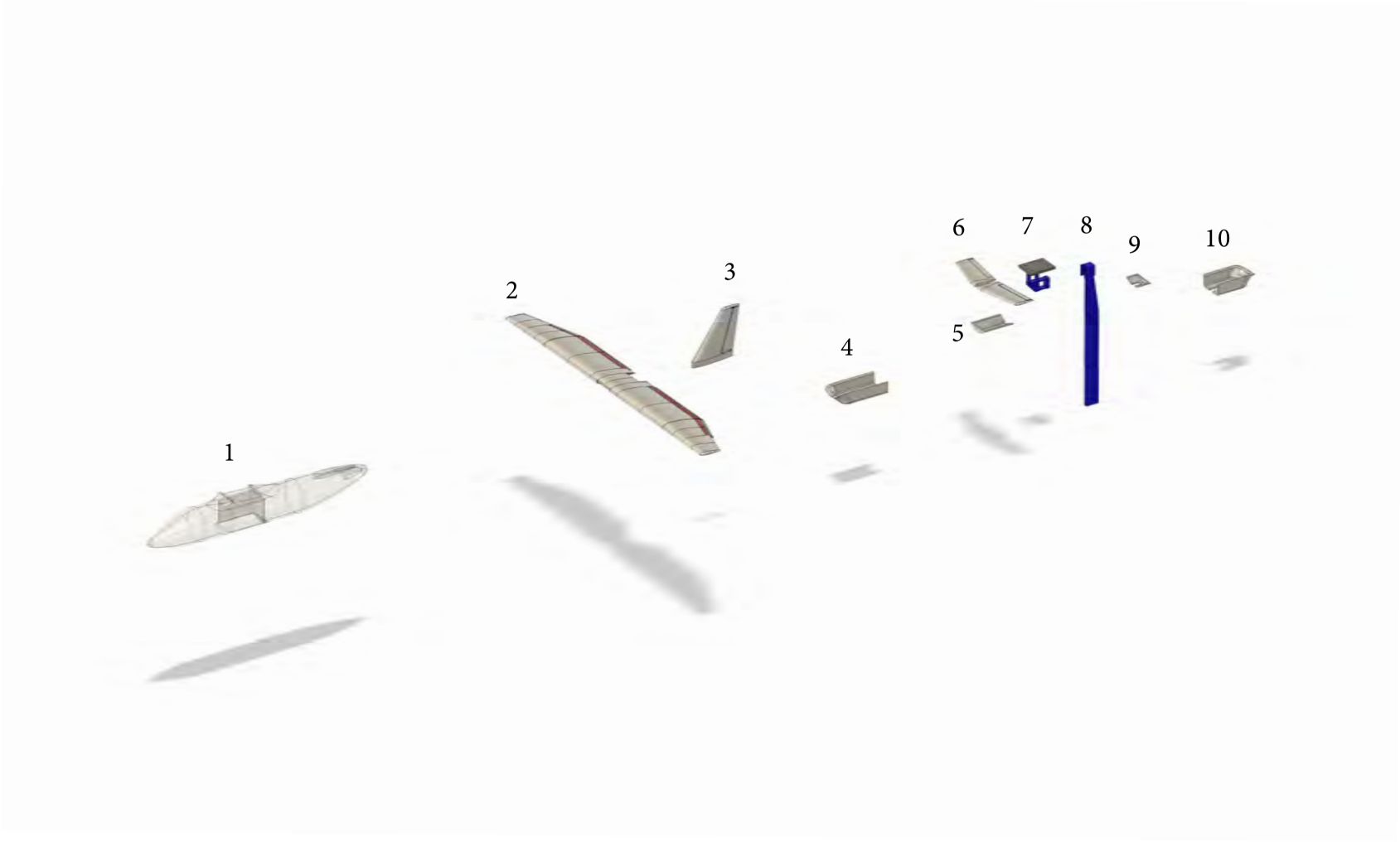

Figure A.5 Exploded view of the PROSIB CAD model 19 pax.

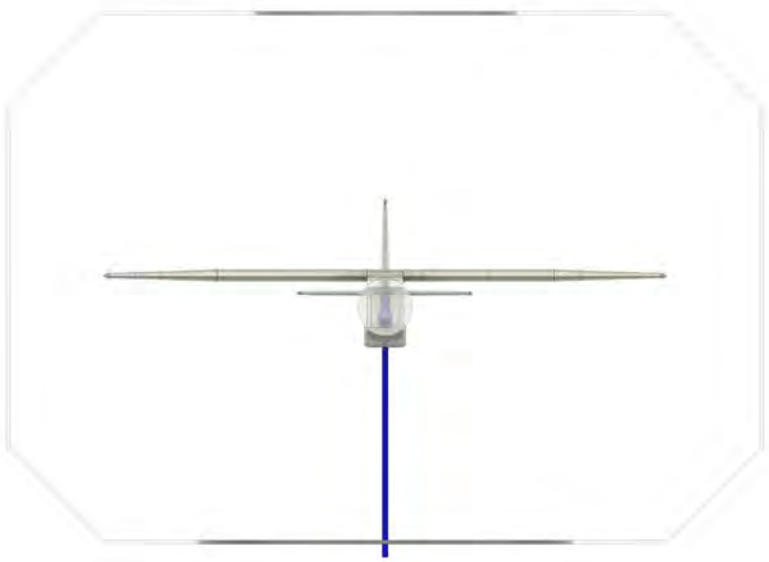

(a)

(b)

Figure A.6 Frontal and lateral view of the PROSIB CAD model 19 pax installed in the wind tunnel.

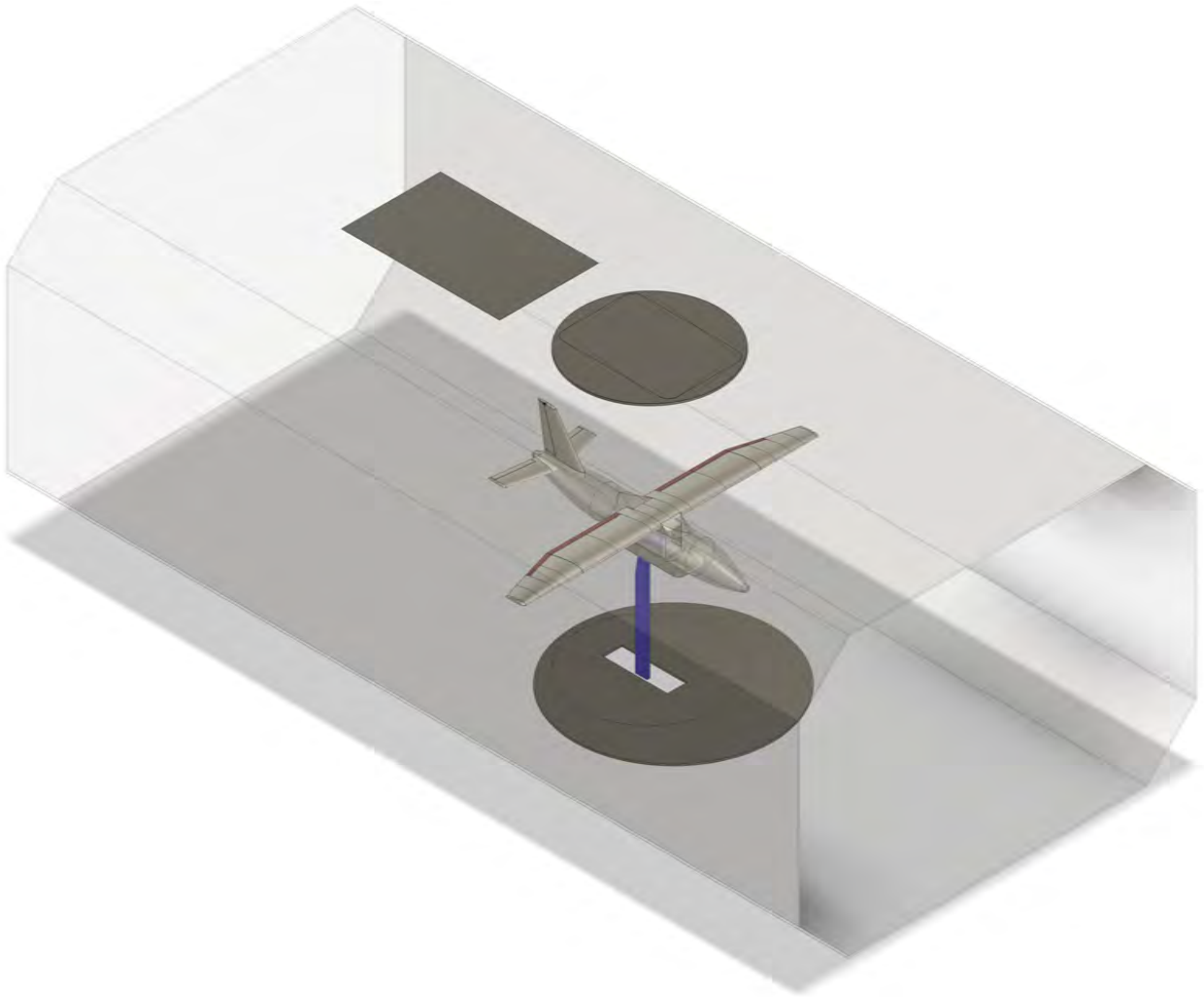

Figure A.7 View of the PROSIB CAD model 19 pax installed in the wind tunnel.

(a)

(b)

Figure A.8 Rendering of the aircraft model with Autodesk Fusion 360.

References

[1] United Nations Department of Economic and Social Affairs. *World Population Prospects 2022: Summary of Results*. Population Division, 2022.

[2] United Nations. *The Sustainable Development Goals Report*. 2022.

[3] Bolt, J., Timmer, M., and van Zanden, J. "GDP per capita since 1820". In: van Zanden, J. et al. *How was life?: Global well-being since 1820*. OECD Publishing, 2014. URL: http://dx.doi.org/10.1787/9789264214262-7-en.

[4] Schafer, A. and Victor, D. G. "The future mobility of the world population". In: *Transportation Research Part A: Policy and Practice* 34.3 (2000), pp. 171–205. ISSN: 0965-8564. DOI: https://doi.org/10.1016/S0965-8564(98)00071-8.

[5] Michelmann, J. et al. "Influence of COVID-19 on air travel - A scenario study toward future trusted aviation". In: *Journal of Air Transport Management* (2022), p. 102325. ISSN: 0969-6997. DOI: https://doi.org/10.1016/j.jairtraman.2022.102325.

[6] Lee, D. S. et al. "Aviation and global climate change in the 21st century". In: *Atmospheric Environment* 43.22 (2009), pp. 3520–3537. ISSN: 1352-2310. DOI: https://doi.org/10.1016/j.atmosenv.2009.04.024.

[7] Ryley, T., Baumeister, S., and Coulter, L. "Climate change influences on aviation: A literature review". In: *Transport Policy* 92 (2020), pp. 55–64. ISSN: 0967-070X. DOI: https://doi.org/10.1016/j.tranpol.2020.04.010.

[8] Ciliberti, D. et al. "The Enabling Technologies for a Quasi-Zero Emissions Commuter Aircraft". In: *Aerospace* 9.6 (2022). ISSN: 2226-4310. DOI: 10.3390/aerospace9060319.

[9] Le Quéré, C. et al. "Temporary reduction in daily global CO2 emissions during the COVID-19 forced confinement". In: *Nature Climate Change* 10 (2020), pp. 647–653. ISSN: 1758-6798. DOI: 10.1038/s41558-020-0797-x.

[10] Forster, P. M. et al. "Current and future global climate impacts resulting from COVID-19". In: *Nature Climate Change* 10 (2020), pp. 913–919. ISSN: 1758-6798. DOI: 10.1038/s41558-020-0883-0.

[11] European Commission, Directorate-General for Mobility and Transport, and Directorate-General for Research and Innovation. *Flightpath 2050 : Europe's vision for aviation : maintaining global leadership and serving society's needs*. Publications Office, 2012. DOI: 10.2777/15458.

[12] Clean Sky 2 and Fuel Cells Hydrogen 2 Joint Undertaking. *Hydrogen-powered aviation : a fact-based study of hydrogen technology, economics, and climate impact by 2050*. Publications Office, 2020. DOI: 10.2843/471510.

[13] EASA. *Certification Specifications for Normal, Utility, Aerobatic and Commuter Category Aeroplanes CS-23*. July 2012. URL: https://www.easa.europa.eu/en/downloads/1742/en.

[14] EASA. *Certification Specifications and Acceptable Means of Compliance for Large Aeroplanes*. Aug. 2017. URL: https://www.easa.europa.eu/en/downloads/32288/en.

[15] XIE, Y. et al. "Review of hybrid electric powered aircraft, its conceptual design and energy management methodologies". In: *Chinese Journal of Aeronautics* 34.4 (2021), pp. 432–450. ISSN: 1000-9361. DOI: https://doi.org/10.1016/j.cja.2020.07.017.

[16] Kim, H. D., Perry, A. T., and Ansell, P. J. "A Review of Distributed Electric Propulsion Concepts for Air Vehicle Technology". In: *2018 AIAA/IEEE Electric Aircraft Technologies Symposium (EATS)*. 2018, pp. 1–21. DOI: https://doi.org/10.2514/6.2018-4998.

[17] SNYDER, M. H. and ZUMWALT, G. W. "Effects of wingtip-mounted propellers on wing lift and induced drag." In: *Journal of Aircraft* 6.5 (1969), pp. 392–397. URL: https://doi.org/10.2514/3.44076.

[18] Barlow, J.B., Rae, W.H., and Pope, A. *Low-Speed Wind Tunnel Testing. 3rd ed.* New York: Wiley, 1999.

[19] Baals, D.D. and Corliss, W.R. *Wind Tunnels of NASA*. NASA, Jan. 1981. URL: https://ntrs.nasa.gov/citations/19810023610.

[20] Chanetz, B. "A century of wind tunnels since Eiffel". In: *Comptes Rendus Mécanique* 345.8 (2017). A century of fluid mechanics: 1870–1970, pp. 581–594. ISSN: 1631-0721. DOI: https://doi.org/10.1016/j.crme.2017.05.012.

[21] Dromiack, H.T. and Wagner, L .N. "Inlet Performance of the NFAC 1/50th-scale 80- by 120- Foot Wind Tunnel". In: *AIAA Scitech 2021 Forum* (2021). DOI: https://doi.org/10.2514/6.2021-0510.

[22] Ciliberti, D. "An improved preliminary design methodology for aircraft directional stability prediction and vertical tailplane sizing". PhD thesis. Università degli Studi di Napoli "Federico II", 2016.

[23] Corcione, S. “Design Guidelines, Experimental Investigation and Numerical Analysis of a New Twin Engine Commuter Aircraft”. PhD thesis. Università degli Studi di Napoli “Federico II”, 2015.

[24] Garner, H.C. et al. *Subsonic Wind Tunnel Wall Corrections.* NATO AGARD, 1966.

[25] Raymer, D.P. *Aircraft Design: A Conceptual Approach.* AIAA education series. 5th edition. Reston,VA: American Institute of Aeronautics and Astronautics, 2012.

[26] Roskam, J. *Methods for Estimating Stability and Control Derivatives of Conventional Subsonic Airplanes.* 1971.

[27] Perkins, C.D. and Hage, R.E. *Airplane Performance Stability and Control.* New York: Wiley, 1949, p. 502. ISBN: 047168046X.

Acknowledgements

In conclusione, ci tengo a dedicare questo spazio del mio lavoro a tutte le persone che hanno fatto parte di questo percorso per esprimere la mia gratitudine nei loro confronti.

Un ringraziamento speciale va alla mia famiglia: i miei genitori, mia sorella e mia nonna, ai quali dedico questo intero lavoro. Senza il loro incoraggiamento, la loro presenza, la loro pazienza e i loro insegnamenti, probabilmente questo percorso non sarebbe stato possibile. Sono infinitamente grato di averli al mio fianco.

Vorrei esprimere la mia immensa gratitudine al Prof. Fabrizio Nicolosi per avermi guidato e supportato con estrema professionalità nella preparazione del lavoro finale di tesi, per avermi dato la possibilità di prendere parte a questo entusiasmante progetto sperimentale e per avermi dato l'opportunità di conoscere persone che ogni giorno svolgono il loro lavoro in dipartimento con grande dedizione.

Un immenso grazie va al Prof. Danilo Ciliberti che è diventato per me un solido punto di riferimento e che ha contribuito in modo significativo alla mia crescita professionale. La passione e l'intraprendenza con cui si dedica al suo lavoro sono per me di grande ispirazione.

Non possono mancare i ringraziamenti a tutti gli amici del gruppo M.A.G.A con i quali ho trascorso ore e ore tra i banchi universitari. Abbiamo condiviso tanti momenti di studio, di divertimento e di aiuto reciproco. Porterò sempre nel cuore tutti i momenti trascorsi insieme.

Grazie ai miei amici di sempre Roberto, Antonio e Luisa per essere al mio fianco in ogni momento, per avermi sempre supportato e capito e per aver portato spensieratezza e leggerezza anche nei momenti difficili.

Un posto speciale tra questi ringraziamenti lo merita anche mia zia Assuta: durante questi anni è sempre stata presente ed è per me un grande esempio di tenacia e determinazione.

Grazie infinite a tutti voi.